UNIVERSITY OF TROMSØ UIT

FACULTY OF SCIENCE AND TECHNOLOGY
DEPARTMENT OF PHYSICS AND TECHNOLOGY

Air temperature at 90 km altitude in the Artic obtained using meteor radar

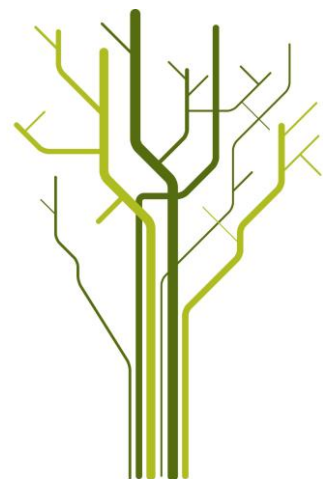## - Validation, characterisation and climate change

Original: Ed Sweeney

Lars Grytbakk Kluken

FYS-3931

Master's thesis in space physics

September 2011

Air temperature at 90 km altitude in the Artic obtained using meteor radar

Validation, characterisation and climate change

Abstract

Temperatures at 90 km altitude above Ramfjordmoen (69°N, 19°E) have been obtained with the Nippon/Norwegian Tromsø Meteor Radar. The temperatures have been derived from meteor radar decay rates using two techniques: the pressure based and the temperature gradient based methods. The results have been compared to the Microwave Limb Sounder (MLS) instrument on board the Aura spacecraft. It was found that the pressure method was simpler to implement than the temperature gradient method and gave better results in relation to the MLS temperatures. With the use of a technique for statistical comparison of geophysical data, the intrinsic uncertainty of the radar temperatures was estimated to be less than 4 K.

Two attempts to combine the two techniques in order to measure both temperatures and pressure with the meteor radar have been carried out. One of the approaches proved to be feasible and gave promising results. This indicates that the meteor radar may have the potential of producing continuous temperature and pressure measurements virtually independent of external data.

A new collocated sodium lidar is introduced and some initial comparisons are carried out between the two instruments. At times there were large discrepancies, but more data is necessary in order to obtain reliable results.

Finally, some possible uses of the radar temperatures are proposed. A method for investigating long term trends is discussed in detail. The data available resulted in a trend of - 2.2 K per decade, but more data is required to establish the trend at the 95 % confidence level. It was estimated that there is a 90 % probability of detecting a significant non-zero trend after approximately 13 years.

Acknowledgements

First and foremost, I would like to thank my main supervisor Chris Hall. His guidance, encouragement, and support were of major importance in the process of writing the thesis. Our numerous scientific discussions and his many constructive comments have been of great value. My second supervisor, Ulf-Peter Hoppe, has also been of invaluable help, especially because of his profound expertise on atmospherical physics.

I would also like to thank Wayne Hocking for extensive technical advising on the temperature gradient method and Werner Singer for supplying the temperature gradient model needed by the technique.

I also want to express my gratitude to Masaki Tsutsumi for clarifying important questions about the works of the radar, and Elizabeth Weatherhead for an enlightening discussion on trend analysis.

Last but not least, I would like to thank Satonori Nozawa for supplying lidar data and Margit Dyrland for supplying the Aura MLS level 2 data, which were crucial for the evaluation and validation of the results obtained in this thesis.

Table of Contents

Chapter 1: Introduction

Lately there has been an increasing interest in the atmospheric region around the mesopause. The mesopause is the boundary region between the mesosphere and the thermosphere. The height of the mesopause varies from 80 to 100 km, depending on the latitude and season. One of the main reasons for the increased focus on the upper atmosphere is that society is becoming more and more dependent on space based technology such as satellite communication and navigation systems. Radio waves are distorted when they pass through the ionosphere, the ionized part of the upper atmosphere. Accurate information on the structure of the upper atmosphere is therefore important in order to ensure good performance in systems like the Global Positioning System (GPS). Another reason for the increased attention is the growing realisation of the importance of the coupling between the mesopause and the neighbouring layers.

The mesopause houses several interesting phenomena. At high latitudes in the summer there is large scale upwelling of air, which causes extremely cold temperatures in the mesopause due to adiabatic cooling. The mesopause is actually the coldest place on earth, with temperatures that could reach down to around -140 °C in the summer (Garcia and Solomon, 1985). Another interesting phenomenon in the mesopause region is the occurrence of polar mesospheric clouds. These are the highest clouds in the atmosphere, and are called noctilucent clouds when visible from the ground. The name noctilucent clouds means 'clouds that shines at night'. The clouds can be seen when light is reflected from ice particles in the clouds, and the sun has set on the lower atmosphere. A related phenomenon is polar mesospheric summer echoes (PMSE), which are anomalous radar echoes found in the artic mesopause region during the summer. Our knowledge about the PMSEs is poor, but they are thought to be caused by water vapour that nucleates into ice crystals because of the extremely cold temperatures in the mesopause. More knowledge about the physical conditions in the mesopause region will be important in order to fully understand these phenomena.

At the height of the mesopause, carbon dioxide is too thin to contain the earth's outgoing infrared radiation, but it will still absorb energy from collisions with the ambient gas. Some of the absorbed energy will be lost to space through radiation. Due to this, the temperature in the mesopause is expected to decrease as carbon dioxide levels rise (Laštovička, et al., 2008).

The mesosphere and lower thermosphere, together called MLT, are regions of the atmosphere which are very hard to explore. The region is too high for balloons to reach, and too low even for the lowest satellite orbits. This leaves rockets as the only method to do in situ measurements. Unfortunately, the use of rockets is very expensive and time consuming. Rockets are therefore highly unsuitable for long continuous temperature measurements of the mesopause. Because of its inaccessibility, the knowledge about the mesopause is sparse. This applies especially to high latitudes, where harsh climate and limited infrastructure limit the research activity.

The mesopause may be less complicated than the underlying atmosphere. There are less local effects that can affect measurements, and the solar influence is particularly low in the mesopause. This might make it easier to determine the cause of potential trends in the measurements, and therefore make the region ideal for investigation of climate change.

In this paper temperature measurements at 90 km altitude will be obtained using data from the Nippon/Norway Tromsø Meteor Radar (NTMR) located at Ramfjordmoen, Norway (69°N, 19°E). The temperature retrieval method will be based upon the method used by Dyrland, Hall, Mulligan, Tsutsumi, and Sigernes (2010) for a similar radar at Adventdalen, Spitsbergen (78°N, 16°E). An alternative approach developed by Hocking (1999) is also investigated, and the possibilities of combining the methods are evaluated.

At the beginning of this paper, the most commonly used techniques for temperature measurement at this height are reviewed and compared to the properties of the radar. Then the details on the radar and the theory of radar echoes from meteor trails are presented. Thereafter the main focus will be on the techniques for temperature acquisition with the radar and comparing the results with other independent instruments. Lastly, the value of the meteor radar temperatures is evaluated and possible ways to utilize the results are considered.

Chapter 2: Various measurement techniques for the mesopause

In the last decades a number of different remote sensing techniques have been developed to measure the temperature in the mesopause region, each with their own individual advantages and disadvantages. Technological advances in lasers and sensors have led to many ground based optical systems. Some of the most used techniques will be discussed below, including space missions and the meteor radar.

2.1 Hydroxyl rotational temperature

One of the oldest and most applied optical techniques measures the hydroxyl (OH) rotational temperature. The temperature is obtained by looking at the relative intensities of the spectral lines of the OH airglow emission. This emission emanates from layers of hydroxyl at an average height of 87 km and an average thickness of 8km (Sigernes, et al., 2003).

There are however some uncertainties regarding the accuracy of the technique. Some older measurements used interference filters to look at the spectral lines. These filters are known to have poor long term stability, and thus make the data less suitable for trend studies (Beig, et al., 2003). However, this is not the case with modern OH airglow measurements. The main uncertainty with this technique lies in the determination of the height of the hydroxyl layer, which in extreme cases has been measured to be up to 10 km lower than the mean height of 87 km (Winick, et al., 2009). These variations will introduce great errors if not taken into account. Since these measurements are passive measurements of the airglow, the height has to be determined by an independent system. In addition, the OH airglow is emitted from a layer of which thickness and vertical distribution varies, making the height determination more complicated. The OH rotational temperature measurement itself usually has very good accuracy, and it has commonly been accepted to be equal to the neutral temperature. However, new research by Cosby and Slanger (2007) suggests that this might not be the case after all.

2.2 Lidar systems

A potassium lidar (K-lidar) is an optical system that can measure the temperature by looking at the Doppler broadening of emission lines from potassium. This technique typically has a resolution of 1 km in height and a temperature uncertainty around 3K (Höffner and Lübken, 2007). The relatively small uncertainties are the main advantage of the K-lidar. Some lidars can measure during day time with the use of daylight filters, but as most other optical systems, they depend on clear sky. Another disadvantage of many lidars is that they often require operation by personnel, which is expensive and impractical in areas with rough weather conditions.

Another high precision optical system is the Sodium lidar (Na-lidar). This lidar measures the temperature from the Doppler broadening of the backscattered signal from sodium atoms. Its properties are generally very similar to the K-lidar. In 2010 such a sodium lidar was installed right next to the meteor radar. Temperature measurements have not been the main focus of the lidar, but measurements for some days were acquired for comparison. The details of this comparison will be discussed in Chapter 9.

2.3 Falling sphere

The falling sphere method is a technique where a rocket carries a folded sphere to around 110 km altitude. The sphere is then dropped and unfolded. By accurately monitoring the fall of the sphere, one can deduce a profile of the atmospheric density. Temperatures can then be obtained by integrating the density profiles. Clearly, one of the biggest weaknesses of the technique is that the measurements are very sporadic in time. Another weakness is that the integration requires knowledge of the initial conditions at the beginning of the drop. The effect of the initial conditions decreases downward with height, so that the temperatures are accurate one to two scale heights below the drop height. The initial conditions are generally not known, but the effect of the initial conditions tends to vanish when the iteration is repeated (Lübken, et al., 1994). Falling sphere measurements will be used several times later in the thesis.

2.4 Space missions

The large focus on the MLT region has led to several space missions. One of the first missions launched was the Thermosphere, Ionosphere, Mesosphere Energetics and Dynamics (TIMED) satellite, which is a NASA mission launched in 2001. Its objective is to investigate the energy transfer in and out of the Mesosphere and Lower Thermosphere/Ionosphere (MLTI) region. It also contributes to research on the basic structure of the mesopause, including temperature measurements.

Another NASA satellite with long temperature records is the Aura satellite. This satellite was launched in 2004. Aura's tasks are to answer questions about changes in the atmosphere and monitor air quality. One of its main objectives is to keep track of changes in the ozone layer. On board the Aura space craft is the Microwave Limb Sounder (MLS) instrument which measures the temperature in the MLT region. Dyrland et al. (2010) chose to use the temperatures from the Aura satellite as a source of calibration for the meteor radar on Svalbard, mainly because it has better temporal cover of the radars location.

A more recent mission is the Aeronomy of Ice in the Mesosphere (AIM) satellite. This satellite's main objective is to explore the phenomena of Polar Mesospheric Clouds (PMCs). To better understand the nature of these clouds and how they form, the satellite will measure the thermal and chemical properties of the mesopause region in which the clouds form. The AIM mission was launched in 2007 and therefore the temperature record was too short to be used in previous calibrations of the meteor radar temperatures. At the time of writing, the satellite has collected data for almost four years and it might be considered used for future calibrations.

The main advantage of satellites is the global coverage, unlike ground stations which measure the region just above their location. Unfortunately, satellites have limited lifetimes due to orbit instabilities, system failures and fuel limitations. This makes it difficult to provide continuous measurements needed for long term studies. In fact, many satellite missions have lifetimes shorter than a solar cycle, which lasts about 11 years.

2.5 Advantages of the meteor radar

The limitations of the optical instruments are the very strength of the radar. The meteor radar does not need clear sky, and can run year round with very little maintenance and supervision. It can make 30 minute average measurements, making it suitable for investigation of both intraday variations and long term variations. An advantage of the meteor radar compared to airglow observations is that the radar measures the height and the temperature simultaneously. The radar itself is relatively inexpensive compared to other systems, and also measures other valuable scientific parameters such as wind speed and meteor flux. A network of meteor radars could run uninterrupted for a very long time and produce relatively good spatial cover.

2.6 Disadvantages of the meteor radar

The main disadvantage of the meteor radar is that it depends on other parameters in order to produce temperatures. For instance the pressure method discussed in Chapter 6 depends on the pressure in order to estimate the temperature. Large uncertainties in these input parameters might cause unacceptably large errors in the temperatures. The techniques for temperature acquisition with meteor radars are fairly new, thus comparisons against other instruments are required to validate the results. Following the example of Dyrland et al. (2010), the temperatures from the Microwave Limb Sounder on board the Aura space craft will be used for comparison.

Chapter 3: Description of the meteor radar

The data used in this paper are obtained by the Nippon/Norway Tromsø Meteor Radar (NTMR), located close to Tromsø at Ramfjordmoen, Norway (69.4°N, 19°E). The radar was installed in November 2003 and is jointly operated by Tromsø Geophysical Observatory (TGO) and National Institute for Polar Research (NIPR, Japan).

The radar consists of five receiving antennas and one transmitting antenna which operate in the very high frequency regime (VHF) at 30.25 MHz. The field of view of the radar is approximately 70° off zenith. Receiving antennas are arranged in a cross, as illustrated in Figure 1, enabling the radar to measure winds speeds and position in the sky through interferometric techniques. All antennas are 3-element crossed Yagi antennas.
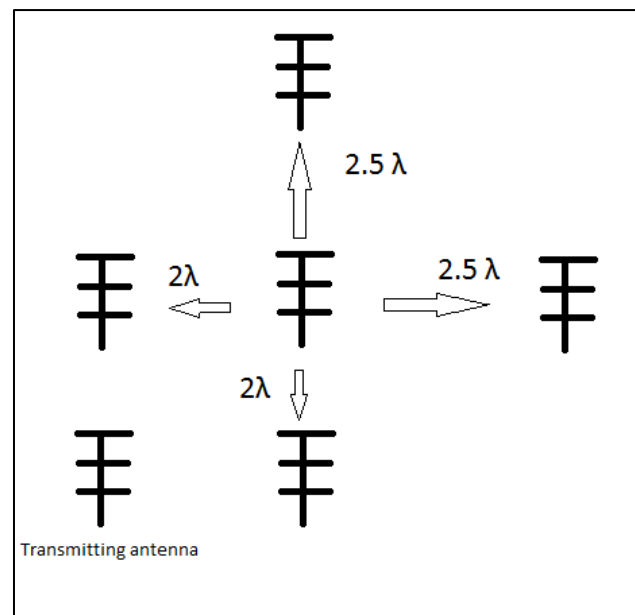

Figure 1: Sketch of the radars antennas arrangement.

The peak power is 7.5 kW, but the average power is only around 500 W and the power is spread out over a large part of the sky in order to detect as many meteors as possible. This results in a very low radiation hazard, which minimizes the need for supervision and facilitates automatic operation.

Figure 2: One of the six identical crossed Yagi-antennas of the Nippon/Norway Tromsø Meteor Radar.

The earth's great orbital velocity causes more meteors to be swept up in the direction of travel than there are meteors catching up with the earth. This will cause a diurnal variation in echo occurrences, especially at low latitudes. The high latitude of this radar causes it to observe less diurnal variation because the observations will almost always be done at high angles to the earth's direction of travel.

The fundamental measurement of the radar is the decay time of the meteor echo. The radar also measures the time it takes for the transmitted pulse to return to the radar, which gives the distance between the meteor and the radar. The configuration of the receiving antennas makes it possible to calculate the position in the sky, which can be used together with the distance to obtain the altitude of the meteor trails. The radar has a height resolution of 1 km.

The output data from the radar relevant to temperature measurements includes time of acquirement, altitude, zenith angle, azimuth angle, error code and decay time for each meteor detected. The error code is an indication that the detected signal is not suited for temperature analysis purposes, and should therefore be excluded from further analysis. Some of the detections with error codes will be unsuitable meteor echoes, but many will also be non-meteoric detections or detections with various analysis errors. A full list of the 16 error criteria used by the radar is found in Holdsworth and Reid (2002) and is reprinted here in Table 1. The same paper also said that when events have zenith angles larger than 70°, the height of the meteors are considered ambiguous. The events are however not assigned an error code as they may be useful in some analyses. In this case the height is important, thus all events with error codes or zenith angles larger than 70° are therefore removed before further analysis. The error codes reduce the total number of events by approximately 40%. Despite this, an average of over 12,000 meteors is left for further analysis.

Table 1: Rejection criteria for the Nippon/Norway Tromsø Meteor Radar

Criterion	Explanation
1	SNR < 12 dB
2	Angle of arrival (AOA) may be unambiguously determined (unused)
3	AOA estimate is not feasible
4	Large difference in AOAs obtained from different antenna baselines
5	Event at start or end of time series
6	Length of event time too short for analysis
7	Event rise time too long to be a meteor
8	Decay time less than twice rise time
9	Power level before meteor event large
10	Power level after meteor event large
11	Poor fit to amplitude for estimation of decay time
12	Poor fit to cross correlation function (CCF) phase variation
13	Range and AOA estimate does not yield a height within the expected height range
14	Range and AOA estimate yield more than one height within expected height range
15	Radial velocity exceeds 200 m/s
16	Oscillatory, indicating event is most likely not underdense

Chapter 4: Radio wave scattering from meteor trails

There are mainly two ways in which portions of a transmitted radar beam can return back to the receiving antennas. One instance is when the radar beam is reflected from a surface layer, similar to how light is reflected by a mirror. The other situation occurs when small fractions of the radar beam are absorbed and backscattered from charged particles in the atmosphere.

A certain change in the refractive index is required in order to reflect the radar waves. The refractive index n is a measure of the speed of electromagnetic radiation through a substance defined by

$$n = \frac{c}{v},$$
(1)

where c is the speed of light in vacuum and v is the phase speed through the medium. The ratio R of reflected radiation is for two materials denoted with indices one and two in the case of normal incidence angle given by

$$R = \left(\frac{n_1 - n_2}{n_1 + n_2}\right)^2$$
(2)

This means that a bigger difference between the refractive indexes will increase the amount of radiation that is reflected. The atmosphere has very weak variations in the refractive index, and it will normally be transparent to radars, but the meteors that frequently enter the earth's atmosphere set up the conditions needed by the radar.

Meteors travel through the vacuum of space at very high velocities. When they enter the earth's atmosphere, the air in front of the meteors compresses very quickly. The compression instantly heats the air to temperatures high enough for it to ionize. The heat and friction will completely ablate most meteors before they reach the ground. The plasma in the trail is what

makes it possible to receive the returned signal at ground, because there is a change in the refractive index between the ionized plasma in the trail and the ambient neural atmosphere.

The refractive index of the meteor trail depends on the free electron density. Together with Equation (2), this means that a stronger gradient in the free electron density will increase the reflectivity. The gradient needed for reflection is dependent on the frequency of the radar. Higher frequencies require stronger gradients to be reflected.

4.1   Diffusion of the meteor trail

The reflected power from a meteor trail will fade away and eventually disappear. This is because the plasma in the meteor trail diffuses much like the condensation trail from an aeroplane. Diffusion is the movement of atoms or molecules from an area of higher concentration to an area of lower concentration. The process continues until the differences in the concentrations are equalized, thus also removing the gradient needed to reflect the radio wave. Diffusion is driven by the thermal motion of the particles and its speed also depends on the viscosity of the involved matter. The fact that the diffusion is independent of the magnitude of the concentration makes it easier to link the speed of the diffusion to the temperature.

The ions in the meteor trail are much heavier than the electrons. The ions will therefore have much lower thermal velocities than electrons at the same temperature. Because of this, one might think that the electrons would diffuse faster than the ions, but both ions and electrons will diffuse at the same rate. The reason for this is that the equations of diffusion assume that there are no other forces acting on the system. In a meteor trail there are electric forces between the ions and electrons that have to be taken into account. What actually happens is that the initial fast diffusion of the electrons, cause a separation from the slow ions. This sets up an electric field, which will speed up the ions and slow down the electrons. Such diffusion of charged particles is called ambipolar diffusion. The result is that both electrons and ions diffuse at a rate which is somewhere between the rate that one diffuses without the other.

4.2   Overdense echoes

An overdense meteor trail is a trail where the plasma frequency is higher than the radar frequency (McKinley, 1961). An overdense echo occurs when the radar beam is reflected from a surface layer of an overdense meteor trail. The plasma frequency is proportional to the electron density. Since bigger meteors usually create trails with high electron densities, the overdense meteors are likely to be large. Figure 3 illustrates the cross section of a trail where the electron density in the central part is high enough for the radio wave to get reflected. Surrounding the dense part of the trail is a layer of underdense plasma. As the trail diffuses the overdense part expands, creating a larger surface available to reflect the radar beam. Eventually, the expansion will cause the electron density to decrease to a level insufficient for surface reflection. If temperatures were to be obtained using overdense meteors, one would have to look at how the diffusion increases the diameter of the overdense part of the trail. Unfortunately, the overdense trails can last for several seconds, making the trails prone to distortions by wind. The relatively small flux of incoming overdense meteors along with the risk of distortions makes them unsuitable for temperature measurements.
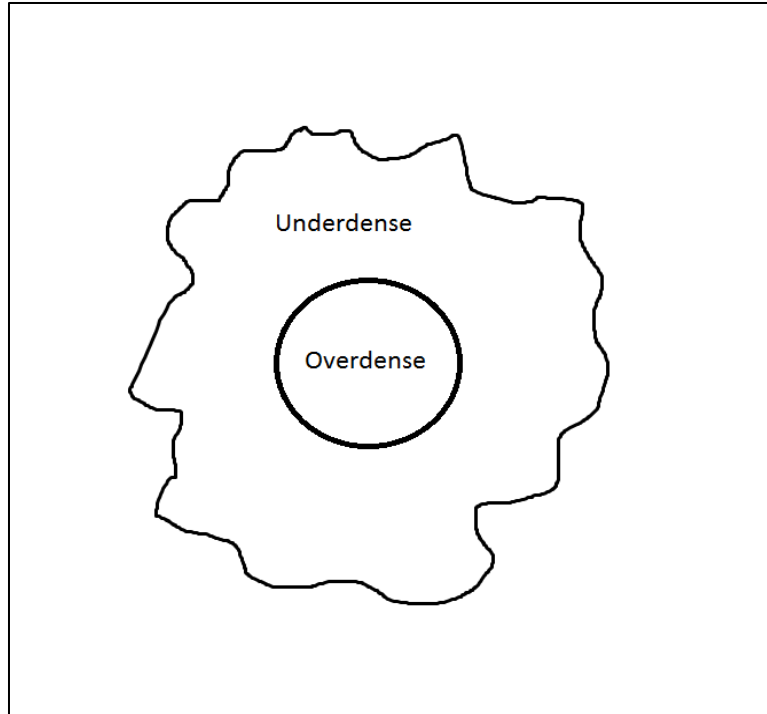
Figure 3: Illustration of the cross section of a meteor trail. The highly ionized central part is overdense and the less dense surrounding part is underdense.

4.3 Underdense echoes

An underdense meteor is a meteor where the radio wave is not reflected at the surface, but rather penetrates into the trail and scatters from individual electrons. These meteors are smaller and much more numerous than the overdense meteors. The underdense meteors normally weigh less than 10^{-6} kg and have a radius less than 10^{-3} m (Havnes and Sigernes, 2005). Some of the radiation scattered from the electrons will be backscattered to the meteor radar. In such cases the received signal will rise in a few hundredths of a second and then decline with an exponential decay as illustrated in Figure 4. The total evolution of signals from underdense meteors lasts no more than a few tenths of a second, thus making them less exposed to distortions by winds. The fading time of these echoes depends mainly on the ambipolar diffusion, which itself is dependent on the temperature.
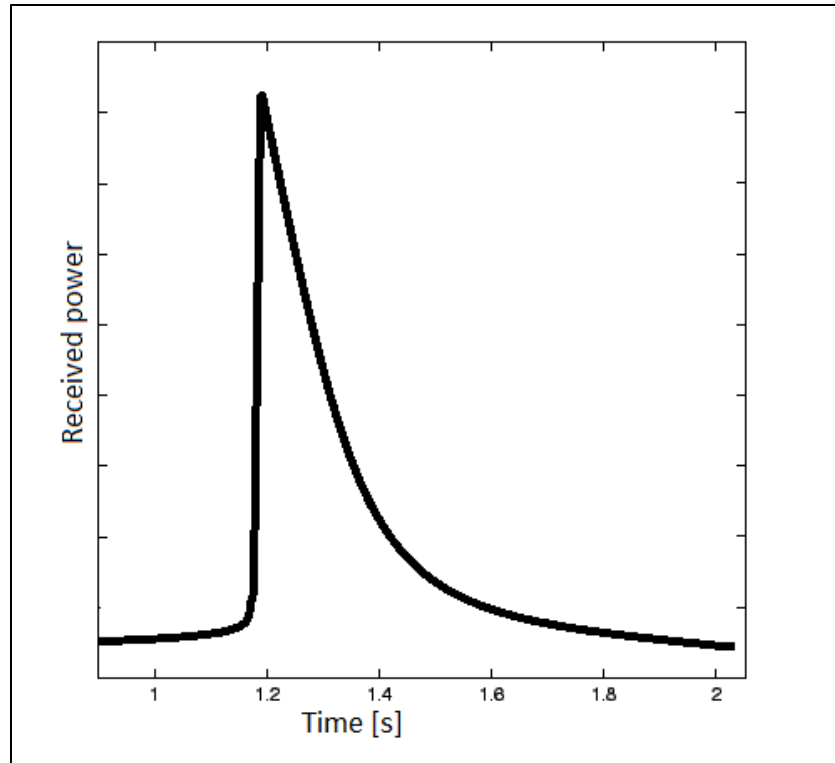
Figure 4: Sketch of the received power from an underdense meteor echo as a function of time. The signal is characterized by a step rise in the received power, followed by an exponential decay.

4.4 Frequency dependency

The frequency choice of the radar depends on two criteria. First of all, the frequency has to be high enough to penetrate the meteor trail, such that the signal is backscattered from the electrons inside trail. Higher frequency will therefore increase the amount of underdense echoes, but too high frequencies will result in lower backscattered power, shorter fading times of the echoes and lower the maximum observation height (Hall, et al., 2006). Lower backscattered power will reduce the amount of detected meteors and therefore aggravate the statistics. Also, if the frequency is too low, there is a risk of group retardation or complete reflection of the signal by the ambient ionosphere (Hall, et al., 2006). In addition, a lower frequency is more prone to refraction and thus increasing the uncertainty in the altitude.

4.5 Decay time and ambipolar diffusion coefficient

Now the decay time will be defined and a relationship between the decay time and the ambipolar diffusion coefficient will be established. If there were no diffusion and the meteor trail had no thickness, the backscattered power received by the radar would according to diffraction theory be (McKinley, 1961):

$$P_r = 2.5 \cdot 10^{-32} \cdot P_t \cdot G_t \cdot G_r \cdot q^2 \cdot \left(\frac{\lambda}{R_0}\right)^3 \cdot \frac{C^2 + S^2}{2}, \tag{3}$$

where P_r and P_t are the received and transmitted power, G_r and G_t are the transmitting and receiving gain of the antenna, q is the electron line density of the trail, λ is the wavelength of the radar, R_0 is the perpendicular distance to the trail and C and S are Fresnel integrals from diffraction theory. Further, it will be assumed that the radial density of electrons in the trail is Gaussian. Simulations done by Jones (1995) showed that the initial electron density of the trail is not Gaussian, but rather has a compact core surrounded by a less dense distribution of electrons. The same paper also showed that correcting for the distribution does not change the resulting expression of the decay time. Using the Gaussian distribution McKinley (1961) showed that the ratio of the received power at time t, P_R (t), over the ideal scattered power, P_R (0), from the case of no diffusion in Equation (4) is given by

$$\frac{P_R(t)}{P_R(0)} = \left(\frac{A}{A_0}\right)^2 = e^{-\left(\frac{8 \cdot \pi^2 \cdot r_0^2}{\lambda^2}\right)} \cdot e^{-\left(\frac{32 \cdot \pi^2 \cdot D_a \cdot t}{\lambda^2}\right)} ds \tag{4}$$

A is the amplitude of the signal, D_a is the ambipolar diffusion coefficient and r_0 is the initial radius. The first exponential in this expression describes the immediate attenuation due to the finite initial radius of the trail. The second exponential is time dependent and tells us how the power decays as a function of time. The decay time is usually defined as the time it takes for the power to fall by $1/e^2$ or amplitude to fall by 1/e. By solving for which t the exponential equals 1/e one gets an expression for the decay time τ:

$$\sqrt{e^{-(\frac{32 \cdot \pi^2 \cdot D_a \cdot t}{\lambda^2})}} = e^{-1}$$

$$\frac{16 \cdot \pi^2 \cdot D_a \cdot t}{\lambda^2} = 1$$

$$\tau = \frac{\lambda^2}{16 \cdot \pi^2 \cdot D_a} \tag{5}$$

An expression for the ambipolar diffusion coefficient is then easily obtained by rearranging the above equation.

$$D_a = \frac{\lambda^2}{16 \cdot \pi^2 \cdot \tau} \tag{6}$$

It should be noted that some authors use different definitions for the decay time. For example Hocking, Thayaparan, and Jones (1997) and Kumar (2007) define the decay time as the time it takes for the amplitude to fall to half of its original value.

The above analysis is valid only under the assumption that the expansion of the trail is governed by ambipolar diffusion alone. Unfortunately, there are several effects that are known to influence the dissipation of the meteor trails. Plasma simulations done by Dyrud, Oppenheim, and vom Endt (2001) showed that the density gradients at the edges of the meteor trails a few kilometres above 90 km, drive instabilities which create an anomalous diffusion that can affect the radar results. Below 90 km there is an increasing risk of underestimating the decay time as turbulence may contribute to the dissipation of the meteor trail (Hall, 2002). A recent study showed that the decay time for underdense meteor echoes can vary depending on the strength of the echo. Although having great influence both below and above 90 km, the effect is negligible at 90 km altitude. The study also found that the occurrence of noctilucent clouds increases the diffusion rate of the meteor trails at all altitudes (Singer, Latteck, Millan, Mitchell and Fielder, 2008). Along with the minimum of disturbing effects at 90 km, it is also the

altitude where most meteors are detected with the frequency of this radar. This makes 90 km

the ideal altitude for temperature measurements with the meteor radar.

Chapter 5: Method for statistical comparison of geophysical data

Later in the thesis the temperatures produced by the radar will be compared against the Aura MLS temperatures. A common way to determine the relationship between two measurements is to apply the least squares regression. A problem with this method is that it assumes that there is no uncertainty in one of the datasets. This chapter introduces a method for statistical comparison of geophysical data, which was developed by Hocking, Thayaparan and Franke (2001b). The main advantage of this technique is that it takes the uncertainties of both datasets into account.

With the standard least squares regression it would be typical to use the Aura temperatures as the independent variable with zero uncertainty. Such an assumption would lead to an overestimation of the uncertainty in the radar temperatures. The uncertainty of the Aura MLS temperatures is stated to be ± 3.5 K (Livesey, et al., 2007). The method Hocking et al. (2001b) developed was originally intended for comparing measurements of one geophysical parameter obtained by different instruments, but the technique can replace any standard linear regression analysis.

In the derivation of this technique, the datasets involved will be called X and Y. X is the measurements of a parameter V, and Y is measurements which are linearly related to the same parameter. In this case, the X could represent the Aura MLS measurements and Y could be the radar measurements. The mean of both sets is assumed to be zero. Although this rarely is the case, it can easily be achieved by removing the mean value from each dataset. The relationship between the two measurements can be written as

$$Y_i = X_i \cdot g_0 \qquad \text{i}=\{1, \text{N}\} \, , \tag{7}$$

where g_0 is the gain of Y relative to the parameter V and N is the number of measurements. In the following analysis there are two important assumptions. The first is that the measurement

errors are normally distributed with zero mean, and the second is that the errors are mutually independent.

The analysis starts by looking at the variances of the datasets. X is equal to V plus some normally distributed noise $X_i = V_i + \delta_{xi}$ and similarly $Y_i = V_i \cdot g_0 + \delta_{yi}$.

By squaring the datasets and taking the ensemble average one gets:

$$< X_i^2 >=< V_i^2 > +2 \cdot< \sigma_x V_i^2 > +\sigma_x^2 \tag{8}$$

σ_x and σ_y are the standard deviations of the errors. Because we have assumed zero mean quantities the above Equation becomes

$$< X_i^2 >=< V_i^2 > +\sigma_x^2 \tag{9}$$

And similarly for Y we get

$$< Y_i^2 >= g_0^2 < V_i^2 > +\sigma_y^2 \tag{10}$$

The same procedure for the crossed terms yields

$$< Y_i X_i > = g_0 < V_i^2 > +2 \cdot< \sigma_y \cdot V_i > +< \sigma_y \cdot \sigma_x >$$
$$= g_0 < V_i^2 > \tag{11}$$

The above Equation can be rearranged with respect to g_0 to give

$$g_0 = \frac{< X_i Y_i >}{< V_i^2 >} \tag{12}$$

At this point the standard least squares method would proceed by assuming that there is no uncertainty in the measurements of X. Although this is exactly the assumption that we aim to

avoid, it will give results that can be used in the further progress. From Equation (9) it can be seen that this assumption means that $<V_i^2>$ is equal to $<X_i^2>$. Replacing $<V_i^2>$ in the equation above gives an expression for the slope, which will be called g_x because of the assumptions of zero error in the X measurements.

$$g_x = \frac{<X_i Y_i>}{<X_i^2>} \tag{13}$$

Similarly by assuming zero error in the Y measurements we obtain

$$g_y = \frac{<Y_i^2>}{<X_i Y_i>} \tag{14}$$

Note that the latter is the inverted slope such that it fits the usual regression line Y = $g_y \cdot$ X +c. The slope g_x corresponds to regression of Y on X and g_y corresponds to regression of X on Y. None of these are the correct slope g_0. In fact g_x will always be equal to or less than the true slope, and g_y will always be equal to or larger than the true slope. The slope g_0 is therefore always somewhere between g_x and g_y depending on the assumed uncertainties. In the following analysis we will no longer assume zero errors in the measurements, but rather establish a relationship between the errors and the true slope. From rearranging Equation (13) with respect to the crossed terms one gets

$$<X_i Y_i> = g_x <X_i^2> \tag{15}$$

From Equation (9) we have that $<X_i^2>$ is equal to $<V_i^2> + \sigma_x^2$. Now, inserting this expression for $<V_i^2>$ into Equation (11) and equating with Equation (15) gives

$$g_0(<X_i^2> - \sigma_x^2) = g_x <X_i^2> \tag{16}$$

Again, the same approach is applied to the Y dataset

$$g_0\left(\frac{<Y_i^2> - \sigma_y^2}{g_0^2}\right) = g_x <X_i^2> \tag{17}$$

The $<V_i^2>$ is now eliminated from the equations. Also, $<X_i^2>$ and $<Y_i^2>$ can be estimated with their sample expectations

$$<X_i^2> = \frac{\Sigma_i X_i^2}{N} \tag{18}$$

$$<Y_i^2> = \frac{\Sigma_i Y_i^2}{N} \tag{19}$$

This means that there are two equations with three unknowns: g_0, σ_x and σ_y. This implies that knowledge about one of them will enable us to solve for the others. The last step is to solve Equations (16) and (17) with respect to g_0 and the standard deviations. This gives the final relationships which will be used to estimate the true slope and standard deviations:

$$\sigma_x = \sqrt{\frac{\Sigma_i X_i^2}{N}\left(1 - \frac{g_x}{g_0}\right)} \tag{20}$$

$$\sigma_y = \sqrt{\frac{\Sigma_i Y_i^2}{N}\left(1 - \frac{g_0}{g_y}\right)} \tag{21}$$

$$g_0 = g_y\left(1 - \sigma_y^2 \cdot \frac{N}{\Sigma_i Y_i^2}\right) \tag{22}$$

$$g_0 = \frac{g_x}{\left(1 - \sigma_x^2 \cdot \frac{N}{\Sigma_i X_i^2}\right)} \tag{23}$$

Chapter 6: Pressure based method

The aim here is to relate the ambipolar diffusion coefficient from Equation (6) to the neutral temperature, and to use this relation to estimate the temperature from the measured decay times. The radar temperatures are then compared to the Aura MLS temperatures, followed by a discussion on the errors involved with this method.

6.1 Derivation of the temperature

The relation between the ambipolar diffusion coefficient and the temperature can be established by first looking at the Einstein-Smoluchowski diffusion Equation. This Equation gives an expression for the diffusion coefficient D_i for an ion species in a neutral gas as

$$D_i = \frac{k_B \cdot T_i \cdot K}{e},$$
(24)

where k_B is Boltzmann's constant, T_i is the ion temperature and K is the zero field ion mobility factor of the ion. Mason and McDaniel (1989) showed that the ambipolar diffusion coefficient D_a in the case of a negligible magnetic field can be expressed as

$$D_a = D_i(1 + \frac{T_e}{T_i})$$
(25)

T_e is the electron temperature. After the ablation of the meteor the thermalization of both ions and electrons against the ambient atmosphere happens at the order of milliseconds (Bronshten, 1983). The two temperatures can therefore be assumed to be equal and the ambipolar diffusion coefficient becomes

$$D_a = 2 \cdot D_i$$
(26)

The only parameter left in order to solve for the temperature in the Einstein-Smoluchowski Equation is the zero field ion mobility factor K. It is defined as a proportionality factor of the drift velocity V_d of an ion in a gas when an electric field E is applied.

$$V_d = K \cdot E \tag{27}$$

Unfortunately, K varies a little with the temperature, but the change in K is less than 20% for a temperature change of 100 Kelvin (Ceplecha, et al., 1998). It is common to express the ion mobility as a function of the reduced ion mobility K_0 correcting to standard gas density n_0.

$$K = K_0 \cdot \frac{n_0}{n} \tag{28}$$

With the use of the ideal gas law the ion mobility can be written as

$$K = K_0 \cdot \frac{\dfrac{P_0}{k_b \cdot T_0}}{\dfrac{P}{k_b \cdot T}} = K_0 \cdot \frac{T \cdot P_0}{P \cdot T_0} = K_0 \cdot \frac{T}{P} \cdot \frac{1.013 \cdot 10^5}{273.16}, \tag{29}$$

where the standard temperature T_0 is 273 K and the standard pressure P_0 is 101.3 kPa. The reduced mobility for specific ions can be measured in a laboratory, and these measurements can be used to estimate the ion diffusion coefficient. Unfortunately, the exact content of the meteor trail is not known and K_0 will therefore depend on the ion composition one assumes for the meteor trail. As an example the reduced mobility factor for molecular nitrogen ions N_2^+ in neutral nitrogen gas is $1.9 \cdot 10^{-4} \, m^2 s^{-1} V^{-1}$ (Hocking et al., 1997). For metallic meteor ions the corresponding values lie between $2.4 \cdot 10^{-4} \, m^2 s^{-1} V^{-1}$ and $2.9 \cdot 10^{-4} \, m^2 s^{-1} V^{-1}$ according to Jones and Jones (1990).

By inserting the expression for the ion mobility from Equation (29) into Equation (24), we get

$$D_i = \frac{k_b \cdot T_i}{e} \cdot K_0 \cdot \frac{T}{P} \cdot \frac{1.013 \cdot 10^5}{273.16} . \tag{30}$$

The last steps are then to substituting D_i with D_a and to solve with respect to the temperature, which gives the final result:

$$T = \sqrt{\frac{D_a \cdot P}{K_0 \cdot 6.39 \cdot 10^{-2}}} \tag{31}$$

This equation shows that in addition to the reduced mobility factor and the measured ambipolar diffusion coefficient, the pressure is needed in order to solve for the temperature. Unfortunately, the pressure is generally not known and it will vary on both short and long time scales. Ideally the decay time and the pressure should be measured simultaneously. As pressure measurements in the mesopause are very rare and difficult, one normally has to rely on a model for the pressure values. This may introduce quite large errors depending on the quality of the pressure model, and it will not take day to day variations into account. The errors involved in this method will be discussed in more detail in Section 6.7.

6.2 Acquiring the pressure model

For the location of the radar, there are basically three different data sources available in order to obtain a pressure model. There are two global coverage models called COSPAR International Reference Atmosphere (CIRA) and the Mass-Spectrometer-Incoherent-Scatter (MSIS) model. These models can provide atmospheric temperature and mass densities from which the pressure can be estimated. The third option is a series of measurements done by Lübken and von Zahn (1991) and Lübken (1999). The CIRA model has been criticized for its lack of precision, especially at high latitudes. Due to this criticism and the old age, the CIRA model will not be considered here.

6.2.1 The Mass-Spectrometer-Incoherent-Scatter model

The Mass-Spectrometer-Incoherent-Scatter model describes the neutral temperatures and mass densities in the upper atmosphere. The MSIS model is based on data from various sources

including rockets, satellites and incoherent scatter radars. The model has the following output parameters: total mass density, neutral temperature, exospheric temperature and number densities of He, O, N_2, O_2, Ar and H. There are several versions of this model. The last one is named NRLMSIS-00, but in this paper the preceding model MSIS-E90 will be used because the accuracy is sufficient for making a raw temperature estimate. Also, the data from the MSIS-E90 model can easily be obtained online from *http://omniweb.gsfc.nasa.gov/vitmo/msis_vitmo.html*, whereas NRLMSIS-00 requires dedicated software.

6.2.2   Falling sphere measurements

In 1991, F.-J. Lübken and U. von Zahn published mass densities and temperatures measured at Andøya (69°N, 15.5°E), approximately 120 km from Tromsø. Measurements were done mainly with falling spheres and a sodium lidar. These measurements are monthly averages for all months except April, May and September. In 1999 Lübken published a new paper with a total of 89 falling sphere measurements done in period from late April to late September. The advantage of these measurements is that the measurements are done relatively close to the site of the radar, which might be more accurate than the globally fitted MSIS model.

6.2.3   Calculating the pressure models

The MSIS-E90 model and the falling sphere data give us the temperatures and the mass densities which will be used to calculate the pressure. In Figure 5 the monthly average values from the MSIS-E90 model are shown together with the two falling sphere campaigns from Andøya. The plots are expected to show a smooth annual variation as the data represents climatological values. It is therefore noteworthy that the mass densities from the two falling sphere campaigns seem to show a small inconsistency around April and October, where data from the two datasets meet. The Lübken and von Zahn measurements done in the winter months have less data and it is reasonable to assume that the newer falling sphere data for the summer period are of higher quality. It is emphasized that all the data presented in this thesis represent an altitude of 90 km.
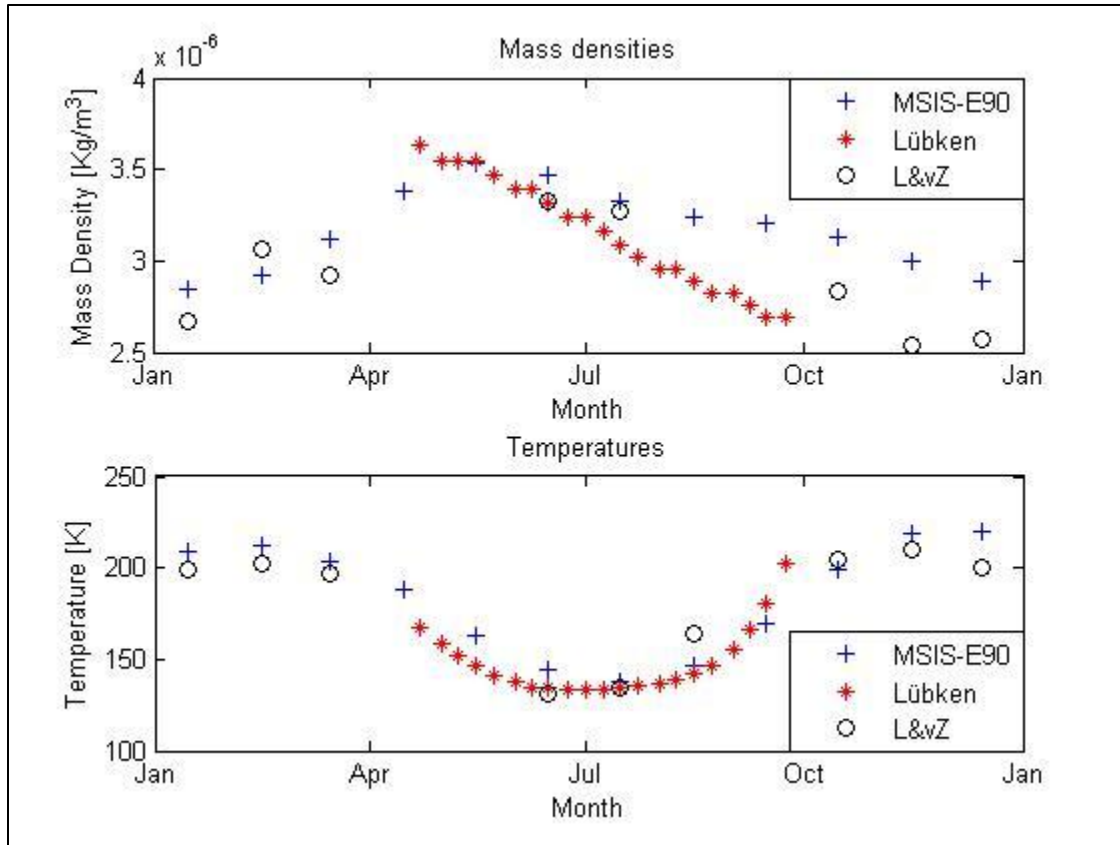
Figure 5: Mass densities and temperatures at 90 km. The MSIS-E90 model is indicated with blue plus signs. The corresponding values of the Lübken and von Zahn campaign is presented with black circles and the latest falling sphere measurements by Lübken are shown as red asterisks.

The pressure can then be estimated from the temperatures and the mass densities by assuming hydrostatic equilibrium and using the ideal gas law of the following form

$$P = \frac{\rho \cdot T \cdot k_B}{M},$$ (32)

where ρ is the mass density, T is the temperature, k_B is Boltzmann constant and M is the molecular mass. For simplicity, the molecular mass is assumed to be constant, made up of 20% oxygen and 80% Nitrogen. This might be an oversimplification, because the meteor region is very close to the homopause. The homopause is a transition region, which is normally situated between 80-90 km. Far beneath the homopause turbulence dominates over diffusion processes causing the atmosphere to be equally mixed. In the homopause on the other hand, diffusion

processes will become increasingly important, thus leading to variations from equal mixing of constituents of different molecular masses.

Another possible source of error is the use of average values of the mass density and the temperature in the ideal gas law. This is because the multiplication of the two average values not necessarily equals the average pressure. From the ideal gas law, the average pressure should be calculated with corresponding mass densities and temperature values as

$$\bar{P} = \frac{k_B}{N} \sum_{i=1}^{N} \frac{\rho_i \cdot T_i}{M_i} = \frac{k_b}{N} \left(\frac{\rho_1 \cdot T_1}{M_1} + \frac{\rho_2 \cdot T_2}{M_2} + \frac{\rho_3 \cdot T_3}{M_3} \cdots + \frac{\rho_N \cdot T_N}{M_N} \right) \tag{33}$$

Since only average values are available, the actual calculation becomes

$$\frac{\bar{\rho} \cdot \bar{T} \cdot k_B}{\bar{M}} = k_B \cdot \frac{\left(\left(\frac{\rho_1 + \rho_2 + \rho_3 + \cdots + \rho_N}{N} \right) \cdot \left(\frac{T_1 + T_2 + T_3 + \cdots + T_N}{N} \right) \right)}{\left(\frac{M_1 + M_2 + M_3 + \cdots + M_N}{N} \right)}$$

$$= \frac{k_B}{N} \cdot \frac{(\rho_1 + \rho_2 + \rho_3 + \cdots + \rho_N) \cdot (T_1 + T_2 + T_3 + \cdots + T_N)}{M_1 + M_2 + M_3 + \cdots + M_N} = \frac{k_B}{N} \cdot \tag{34}$$

$$\frac{(\rho_1 \cdot T_1 + \rho_1 \cdot T_2 + \cdots + \rho_1 \cdot T_N + \rho_2 \cdot T_1 + \rho_2 \cdot T_2 + \cdots + \cdots + \rho_N \cdot T_1 + \cdots + \rho_N \cdot T_N)}{M_1 + M_2 + M_3 + \cdots + M_N}$$

From the above expressions it can be seen that

$$\bar{P} = \frac{k_B}{N} \sum_{i=1}^{N} \frac{\rho_i \cdot T_i}{M_i} \neq \frac{\bar{\rho} \cdot \bar{T} \cdot k_B}{\bar{M}} \tag{35}$$

Unfortunately, the errors introduced by using the average values are difficult to estimate without access to the original measurements.

Figure 6 shows the pressure values estimated from Equation (33). The pressure calculated from the falling sphere measurements turns out to be lower than the MSIS pressure throughout most of the year. It also looks like the inconsistencies between the falling sphere datasets have passed on to the pressure estimates, causing some unexpected behaviour in the pressure in February and April.
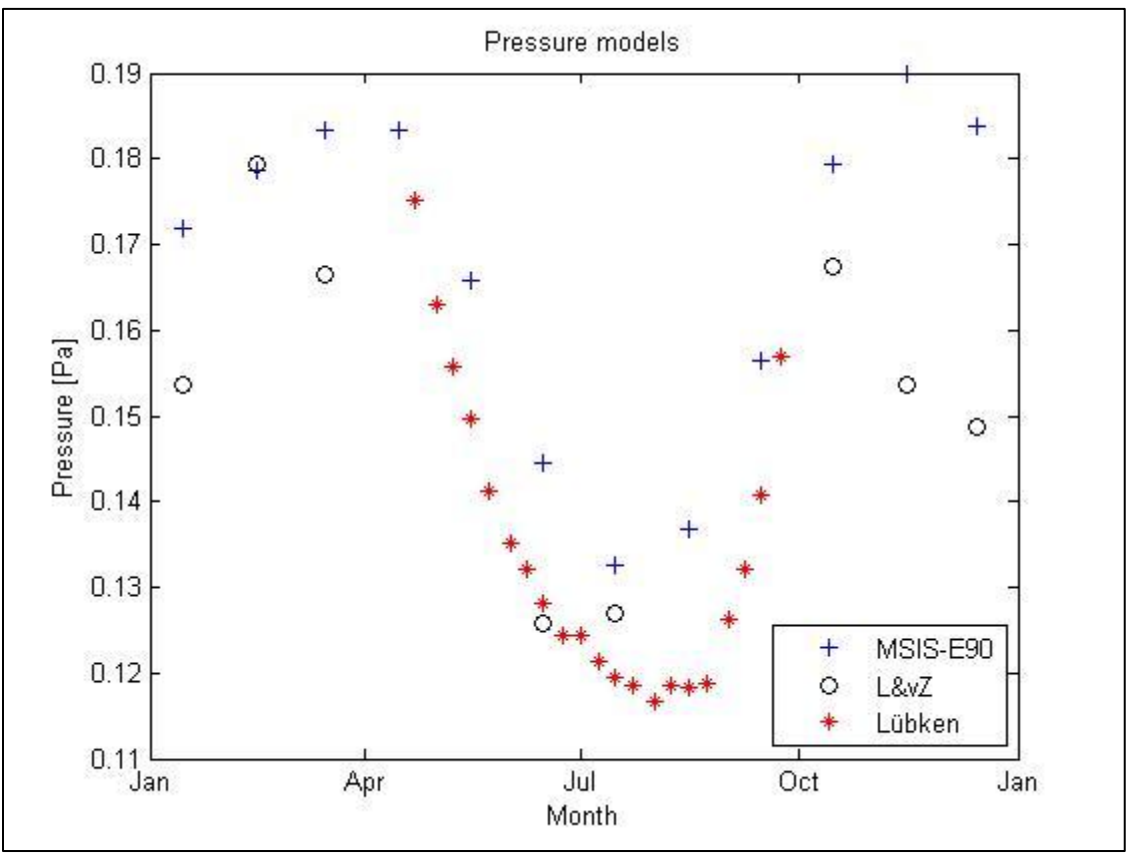

Figure 6: Pressure values estimated by Equation (32) using MSIS-E90 and falling sphere data.

The aim is to end produce daily average temperatures, the pressure is therefore needed for all days throughout the year. For the MSIS-E90 model this is straightforward, as the data can be downloaded as daily averages. The falling sphere measurements on the other hand, have to be interpolated to give daily values.

Before the pressure estimate from the falling sphere measurements are interpolated, some adjustments are needed in order to avoid that the inconsistencies between the datasets cause artefacts in the pressure. As previously stated, the older winter measurements are more likely to be of poorer quality. The winter measurements are therefore manually adjusted with the help of the MSIS-E90 curve to fit with the summer measurements. The result from the adaption is shown as a black line in Figure 7.
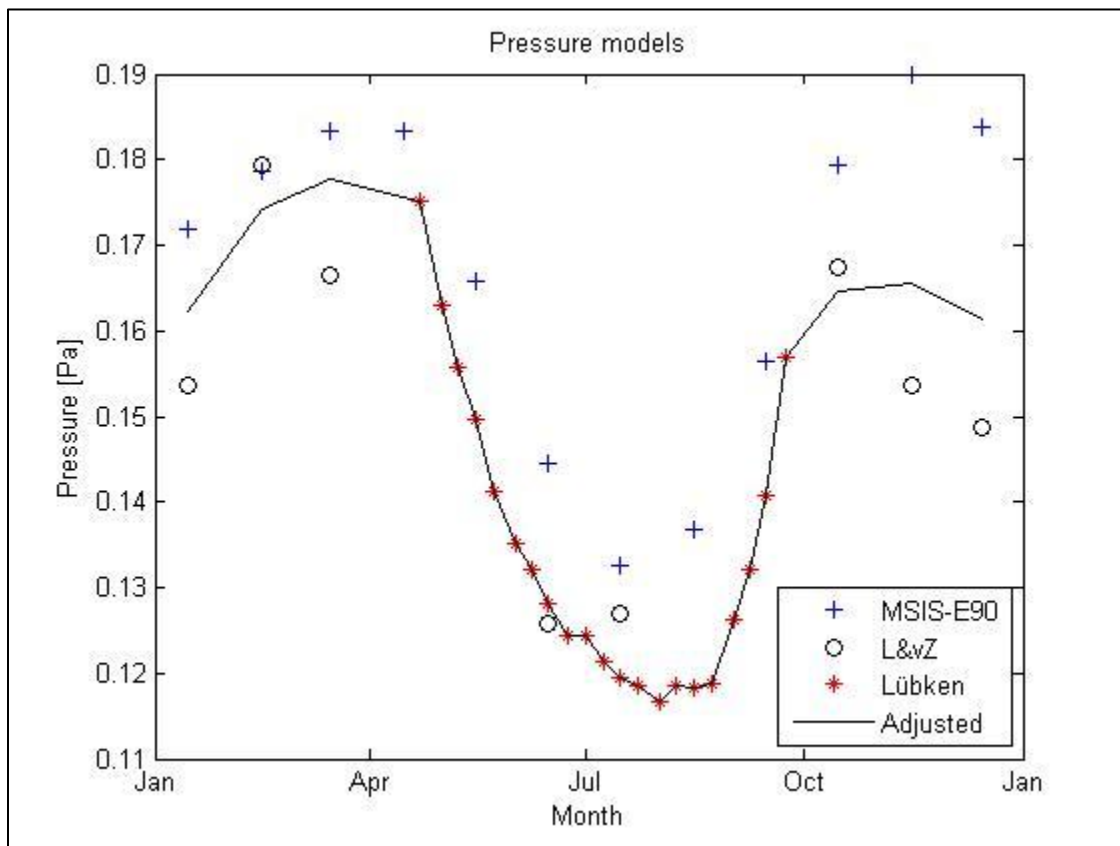

Figure 7: The black line shows how the falling sphere measurements are adjusted in to achieve a smooth annual pressure model.

In Figure 8 the daily pressure model obtained from MSIS-E90 data is shown as a blue line. The red line in the figure is the result of a cubic spline interpolation of the pressure estimated from the falling sphere data. A two way running average has been applied to both of the pressure

estimates to obtain smooth annual pressure models. From now on, the pressure models obtained by MSIS-E90 and falling sphere data are referred to as MSIS-pressure and FS-pressure respectively. It can be seen from Figure 8 that the FS-pressure is lower than the MSIS-pressure. It also looks like there is a phase shift between the two models.
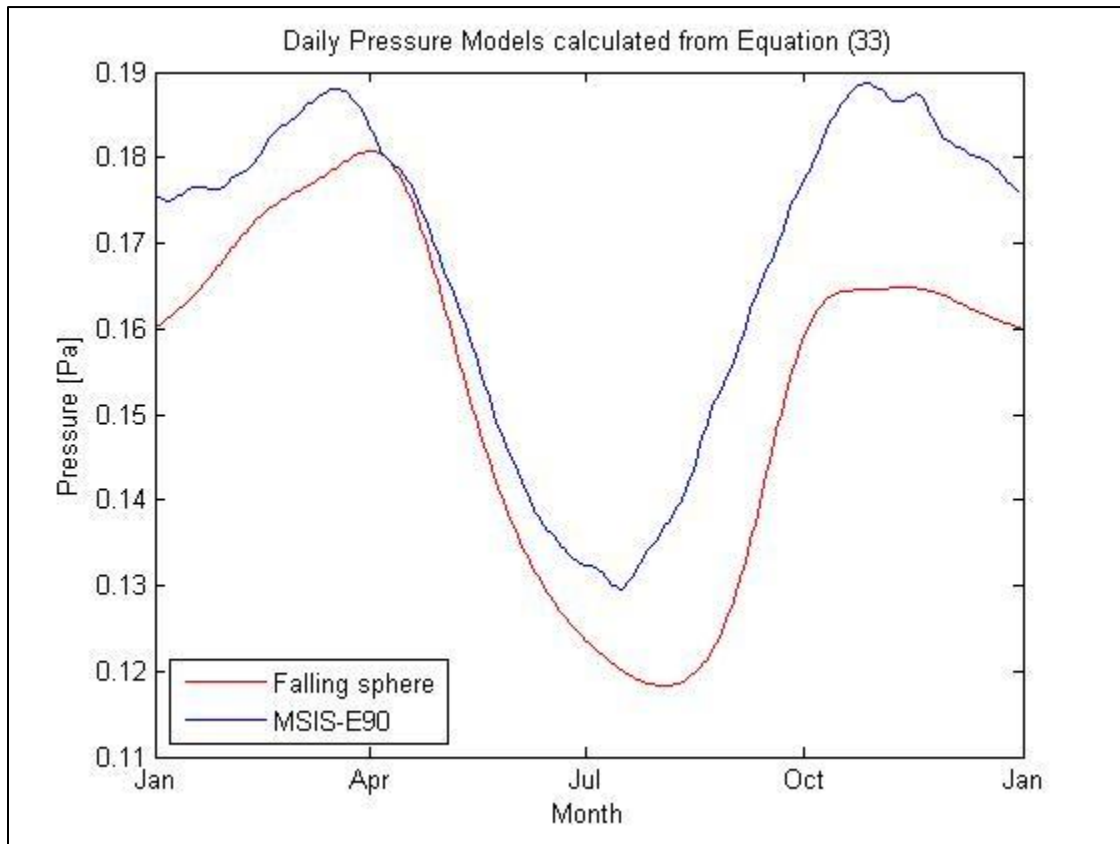

Figure 8: The pressure model obtained from falling sphere data is presented by a red line and the pressure model from the MSIS-E90 data is shown as a blue line. This difference in the two models is most noteworthy in October, November and December where the MSIS model is close to 15% higher.

6.3 The first temperature estimate

Daily average temperatures will be produced because of the large number of meteors throughout a whole day should ensure a good statistical basis. First, the dataset is checked for abnormalities. Days where the radar halted temporarily or days with unusually low meteor counts are removed. These tests have little influence on the dataset, because the radar has run almost continually since it started operating in November 2003.

To obtain temperatures representative of 90 km altitude all meteors between 89.5 and 90.5 km are selected. This introduces an error, unless the vertical temperature gradient is linear and the height distribution of meteors is equally distributed around 90 km. By using a one kilometre wide interval the number of meteors that can be used in the temperature estimate drops from the total of more than 12 000 to approximately 1000. A smaller interval would reduce this number further. Experiments with wider intervals were attempted without improving the temperature estimate, indicating that 1000 meteors are enough to produce reliable temperatures.

One of the main reasons for choosing the height of 90 km is that this is very close to the peak of the meteor height distribution, and the standard deviation from 90 km is relatively small. For a period of six years between 2004 and 2010 the mean peak height of the meteors in the interval was 90.004 km and the standard deviation was 0.011 km. For the whole dataset the largest deviation from the mean height was 0.081 km. Even for a very steep temperature gradient of 5 K/km, this would result in a temperature error of only 0.4 K. This error is therefore considered negligible at 90 km, but it will cause larger errors at heights above or below this height.

A value for the reduced ion mobility has to be specified before the temperatures can be calculated. The value used by different authors span from $1.9 \cdot 10^{-4}\ m^2 s^{-1} V^{-1}$ to $2.5 \cdot 10^{-4}\ m^2 s^{-1} V^{-1}$. The higher values correspond to metallic ions, while lower values corresponds non-metallic ions such as N_2^+. The lowest value was suggested by Chilson, Czechowsky, and Schmidt (1996), but it has received hard criticism afterwards (e.g. Cervera and Reid, 2000). Dyrland et al. (2010) used a value of $2 \cdot 10^{-4}\ m^2 s^{-1} V^{-1}$ while Hall et al. (2006) and Holdsworth et al. (2006) both used a value of $2.4 \cdot 10^{-4}\ m^2 s^{-1} V^{-1}$. Their argument for using this value was to be in accordance with Cervera and Reid (2000), but the value used in that paper was actually $2.5 \cdot 10^{-4}\ m^2 s^{-1} V^{-1}$. Other authors have also used this value, for example Hocking et al. (1997), Takahashi, Nakamura, Tsuda, Buriti and Gobbi (2002) and Kumar (2007). Because of this, the value of $2.5 \cdot 10^{-4}\ m^2 s^{-1} V^{-1}$ will be used when calculating the temperatures.

The next step is to convert the measured decay times into ambipolar diffusion coefficients with the use of Equation (6). Finally, the coefficients are inserted into Equation (31) together with the FS-pressure to produce the first temperature estimate shown in Figure 9.
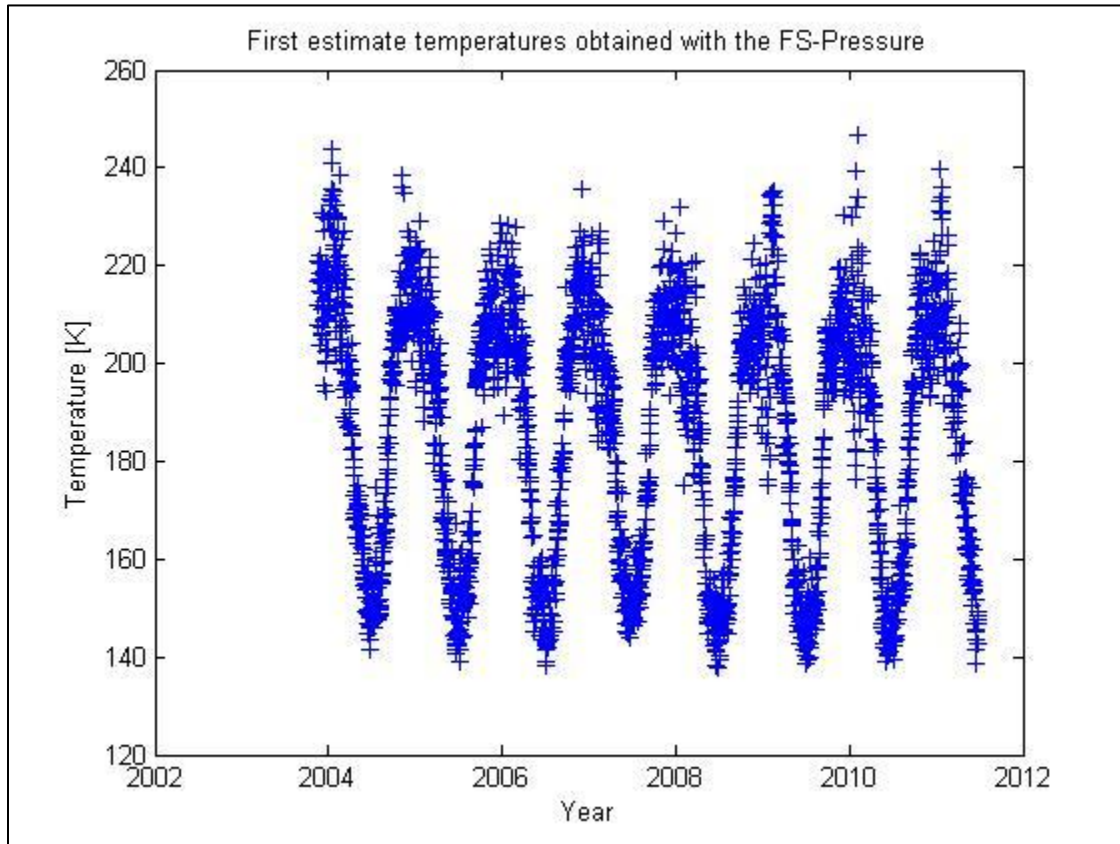

Figure 9: First estimate of meteor radar temperatures at 90 km using the FS-pressure model.

The same procedure is repeated with the MSIS-pressure model. These temperatures are shown in Figure 10, and seem to have quite similar values to the falling sphere version. In order to examine the differences closer, the two estimates are smoothed and plotted together in Figure 11. The red line is the FS-temperatures and the blue line is the MSIS-temperatures. The MSIS-temperatures are generally higher, but the difference is most noteworthy in the winter. This is expected since the deviations in the pressure models are greatest in the winter.
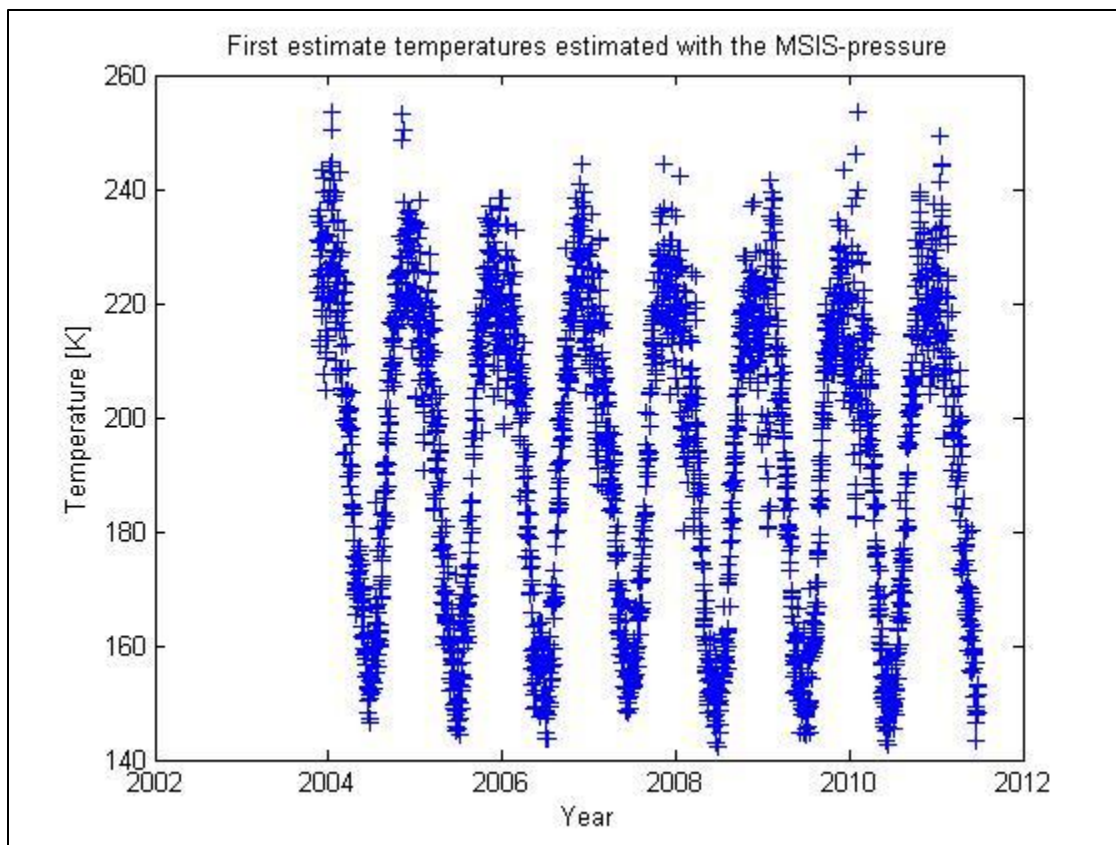
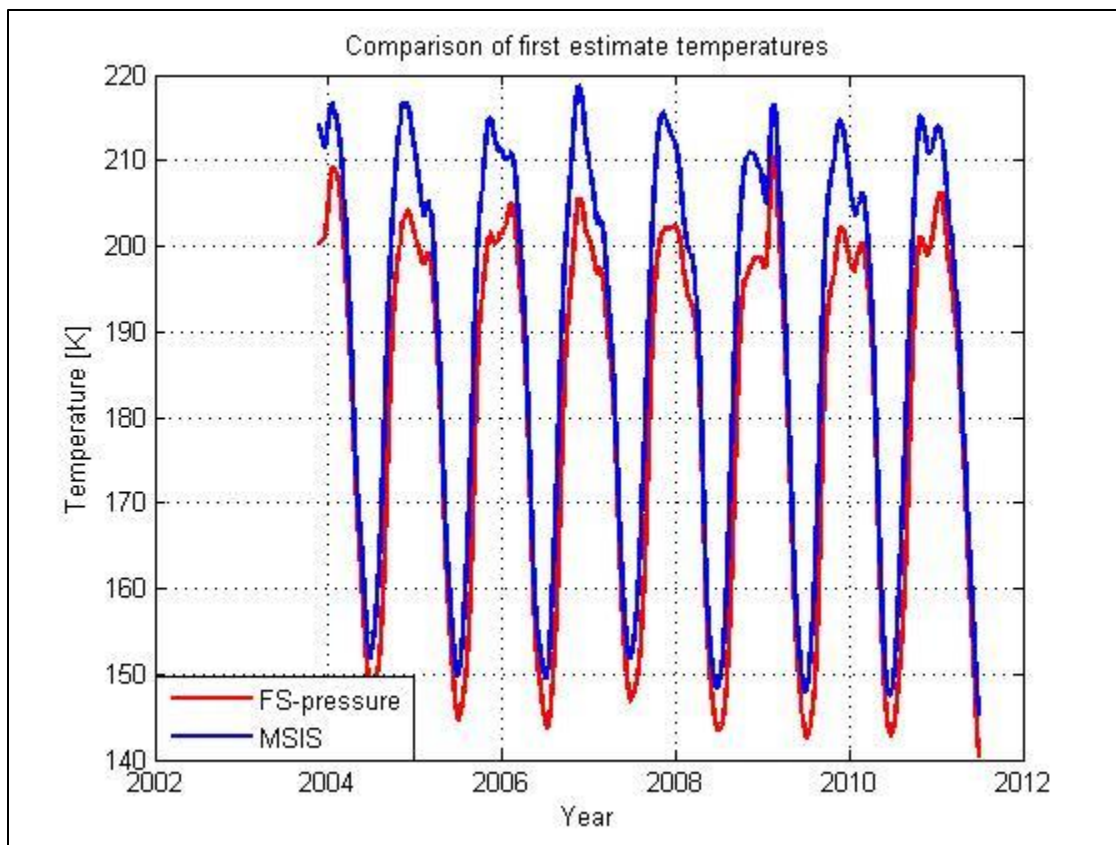Figure 10: First estimate of meteor radar temperatures using the MSIS-pressure model.

Figure 11: Comparison of smoothed temperatures produced with the use of the two pressure models. The FS-pressure model is used to produce the red temperatures and the MSIS-pressure is used to produce the blue temperatures.

Both temperature estimates display the expected annual variation with temperatures below 150 K in the summer and higher temperatures in the winter. Although the estimates look promising at first sight, a comparison against an independent instrument is needed in order to evaluate the temperatures and determine which estimate is better.

Thoroughly validated data from the Aura MLS instrument was kindly provided by Margit Dyrland at the University of Svalbard. At the location of the meteor radar the Aura satellite measures the temperature on two times during the day. The first period is around 2 AM and the other around 11 AM. Figure 12 shows in more detail the periods when the Aura temperatures were recorded in 2006.

Aura measurements within one day were then averaged, bearing in mind that these values may not represent daily averages. Selecting radar measurements done at the same time of the day as the Aura measurements greatly reduces the amount of meteors and had no noteworthy effect on the result. This might be an indication that the two measurement periods of the Aura satellite represents daily averages quite well. Daily averages of the radar temperatures will therefore be used when compared with Aura MLS.
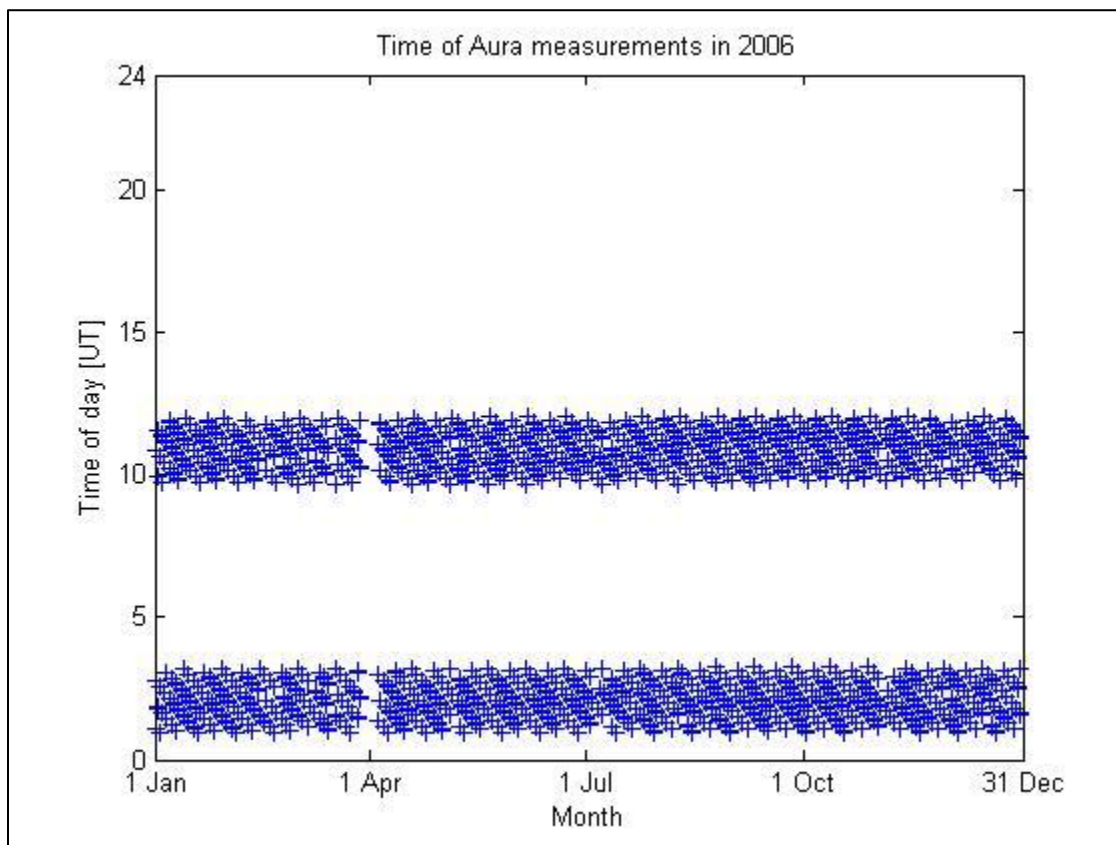

Figure 12: Time of acquisition of the Aura MLS temperatures above the location of the radar.

The Aura MLS measurements at 90 km altitude have an observed scatter of ± 3.5 K and an observed bias of -9 K (Livesey et al., 2007; French and Mulligan, 2010). Therefore 9 K is added to all temperatures in the Aura dataset.

In order to increase the number of available measurements from the Aura satellite, data from an area around the radar location had to be accepted. The maximum radial distance was set to

610 km, thus the distance between the centres of the two measurements can be quite large. The horizontal resolution of the Aura MLS instrument is 220 km, and the radar's field of view at 90 km altitude is 250 km. This means that some of the measurements will not overlap. In Table 2 some statistics on the spatial distribution of Aura's measurements are listed. The standard deviation in latitude from the radar location is 3°, which is equal to a distance of more than 300 km. The maximum deviation in latitude is 4.9° or 550 km.

Table 2: Statistics on the spatial distribution of the Aura temperature acquirements

	Latitude	Longitude
Location of the radar	69.58°	19.22°
Mean	69.86°	18.92°
Standard deviation	3°	8°
Max	74.3°	35.0°
Min	64.7°	3.0°

A comparison of the NTMR temperatures obtained with the MSIS-pressure and the temperatures from the Aura MLS instrument is shown in Figure 13. The temperatures show a similar annual variation, but the radar temperatures are higher at all times. In Figure 14 the same comparison is presented, only this time the FS-pressure is used to calculate the temperatures. The radar temperatures are considerably lower this time and therefore match better with the Aura MLS temperatures. It is reasonable to suspect that the poor match in the winter temperatures is caused by a lower data quality in the winter falling sphere measurements. As mentioned earlier, the FS-pressure model was estimated from measurements done at a site close to the radar, while the MSIS model is based on data from sites located mainly at low- to mid-latitude. Also, the MSIS-E90 model has been reported to conflict with several rocket studies in the mesopause region (Hedin, 1991). Due to this, and the better match against the Aura MLS instrument, the temperatures produced with the FS-pressure will be used in the forthcoming analysis.
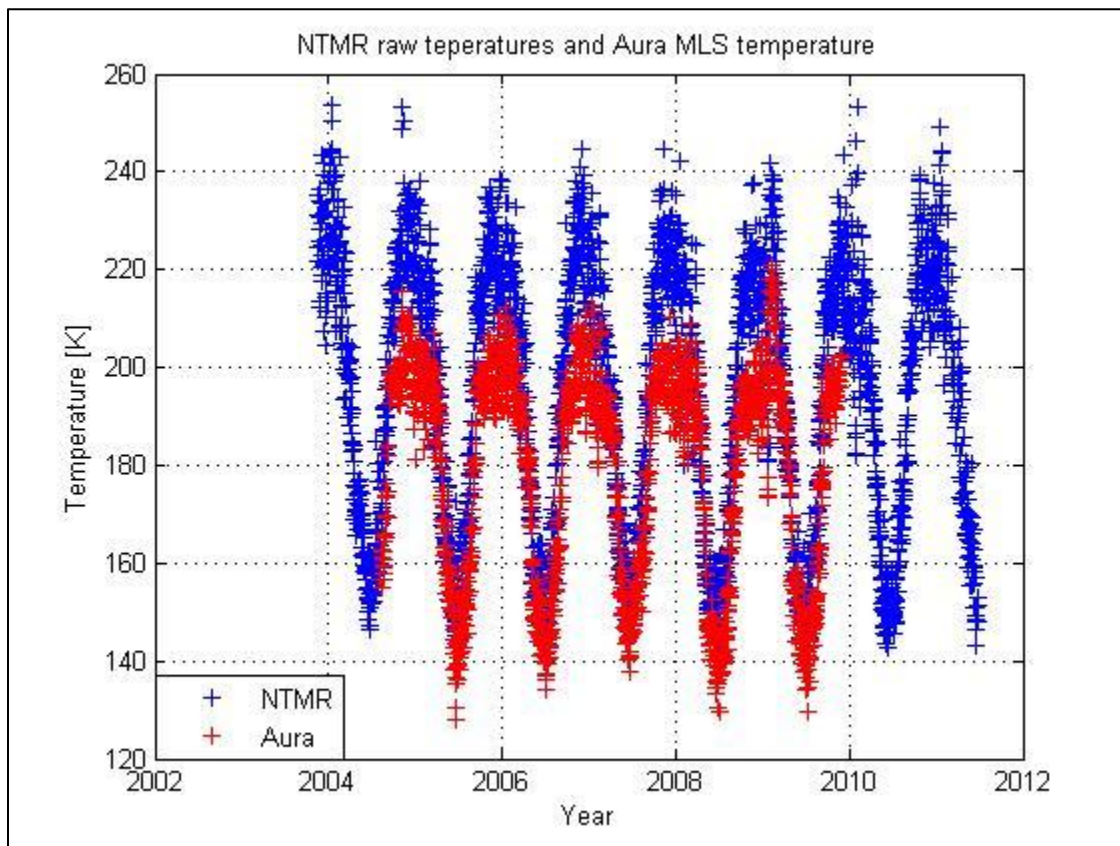
Figure 13: First estimate temperatures obtained with the MSIS-pressure and the Aura MLS temperatures. The radar temperatures seem to be overestimated at all times, especially during the winter.
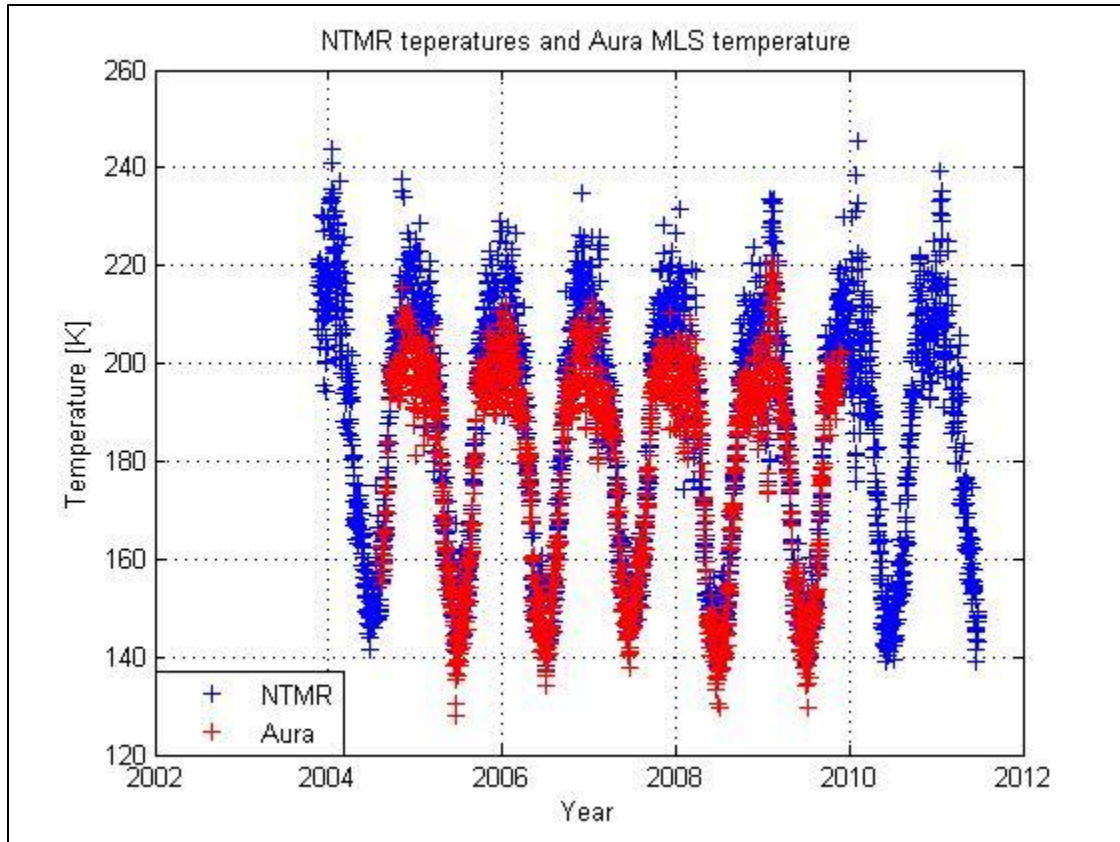
Figure 14: Radar temperatures obtained with the FS-pressure together with temperatures from the Aura satellite. The radar temperatures show a reasonably good match in the summer, but are overestimated in the winter

To get a better look at the small scale variations, a new plot is made with data from 2007 only. Also included in the plot is a linearly interpolated version of the falling sphere climatology. It is evident that the radar temperatures are far superior to the falling sphere temperatures in the summer. This is somewhat surprising since the falling sphere summer measurements were thought to be of higher quality than the winter measurements.
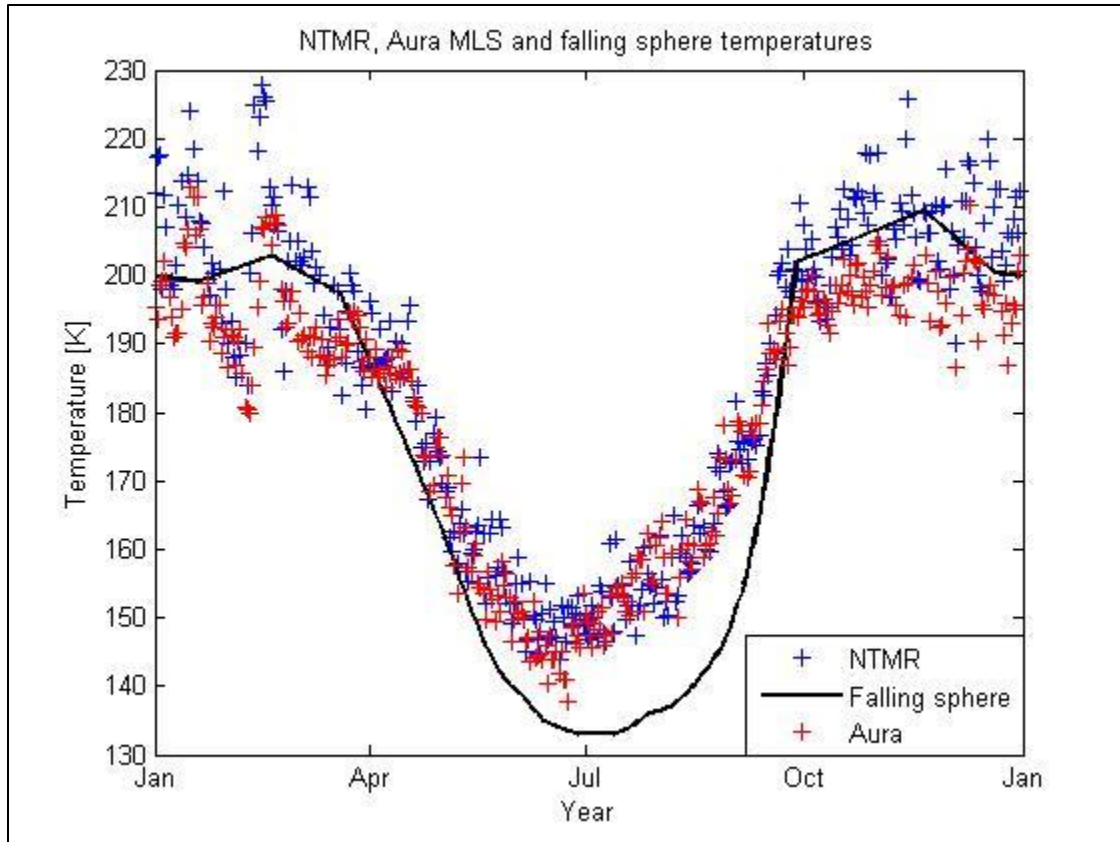
Figure 15: Comparison of the radar, Aura MLS and falling sphere temperatures. Most conspicuous is the deviations of the falling sphere temperatures in the summer, which are much lower that both the Aura MLS and the radar temperatures.

6.4 Calibration against Aura data

The goal here is to use regression techniques to quantify how well the radar temperatures match the Aura MLS temperatures and then calibrate the radar data.

The first step is to select coinciding measurements and make a scatterplot of the radar temperatures versus the Aura temperatures. To begin with, the uncertainty in the Aura MLS measurements is assumed to be zero. The standard least squares regression analysis resulted in the following relationship between the two temperatures.

$$T_{NTMR} = 1.12 \cdot T_{AURA} - 15 \tag{36}$$

The uncertainty in the slope is ± 0.01 and the uncertainty in the intercept is ± 1 K. The resulting scatterplot in Figure 16 also shows the results of the linear regression as a black line. The coefficient of determination R^2 is 0.92, meaning that the linear regression model explains 92% of the relation between the temperatures. The root mean square error is ± 7.2 K, which is very close to the uncertainty that Dyrland et al. (2010) obtained for the similar radar at Svalbard. Two significant figures will be kept in order to make comparisons of upcoming results easier. In this case, the estimator is unbiased and therefore the standard deviation will be identical to the root mean square error. The standard deviation explains how much the radar measurements deviate from the AURA measurements. 68.3 % of the radar measurements will have deviations less than one standard deviation if the data is normally distributed. Likewise, 95.5 % of the radar measurements will have deviations less than two standard deviations, which in this case is 14.4 K.

Eminent in the scatter plot is the slightly curved data. This suggests that the relationship between the measurements is not strictly linear. Dyrland et al. (2010) pointed out that there are two clusters of measurements, one of low summer temperatures and one of high winter temperatures. They also performed linear regression on both sets individually, showing that there are two different relationships for the summer and winter measurements. The reason for the difference is not clear, but it might be caused by errors in the pressure model. The fact that the winter measurements by Lübken and von Zahn (1991) are older, less numerous and obtained in an independent campaign points in that direction. Other possible causes could be violations of the ideal gas or constant molecular mass assumptions used to derive the pressure. The effects of fitting a non-linear curve to the scatter plot will be investigated in Chapter 6.5.
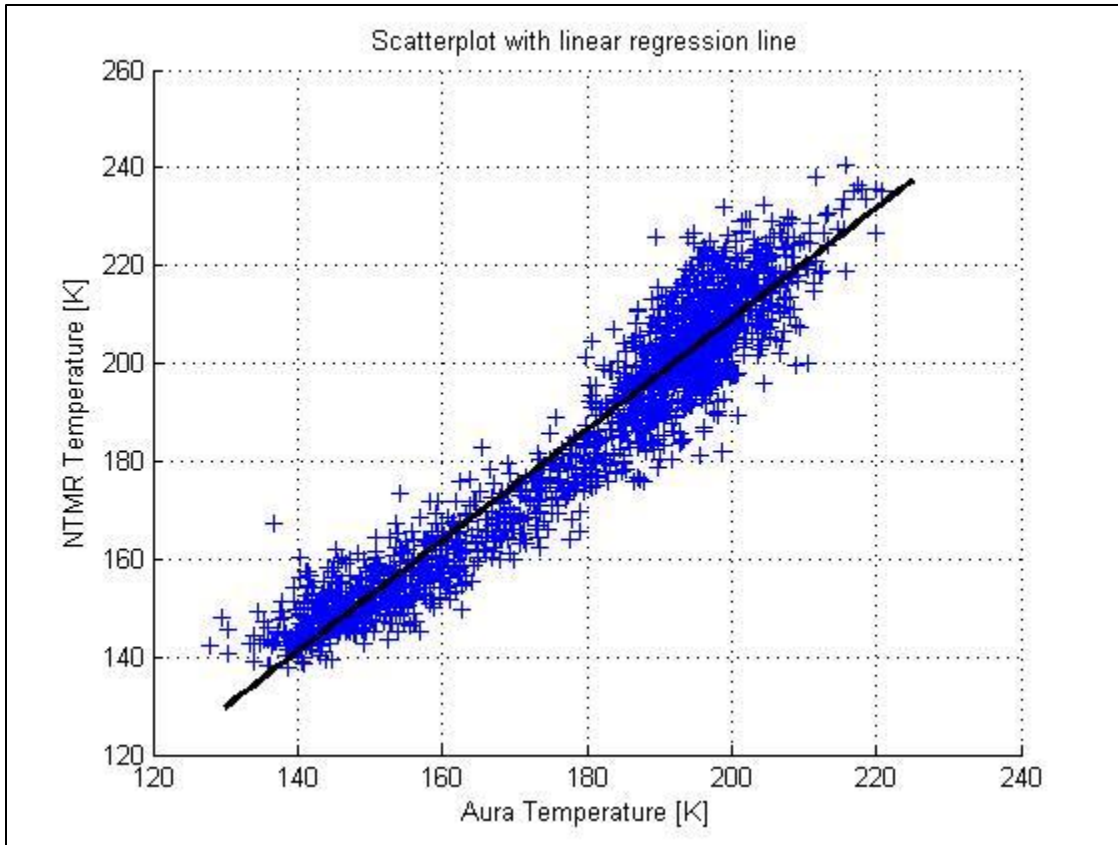
Figure 16: Scatterplot of the radar temperatures versus the Aura MLS temperatures. The black line in the plot is the least squares regression line.

By inverting the relationship in Equation (36) we obtain the following linear equation that is used to calibrate the radar temperatures.

$$T_{Calibrated} = 0.89 \cdot T_{Raw} + 14 \tag{37}$$

The result of the calibration is shown in Figure 17. The calibration has clearly made the winter temperatures match better with the Aura MLS temperatures. The highest radar temperatures are still slightly higher than the highest Aura temperatures.
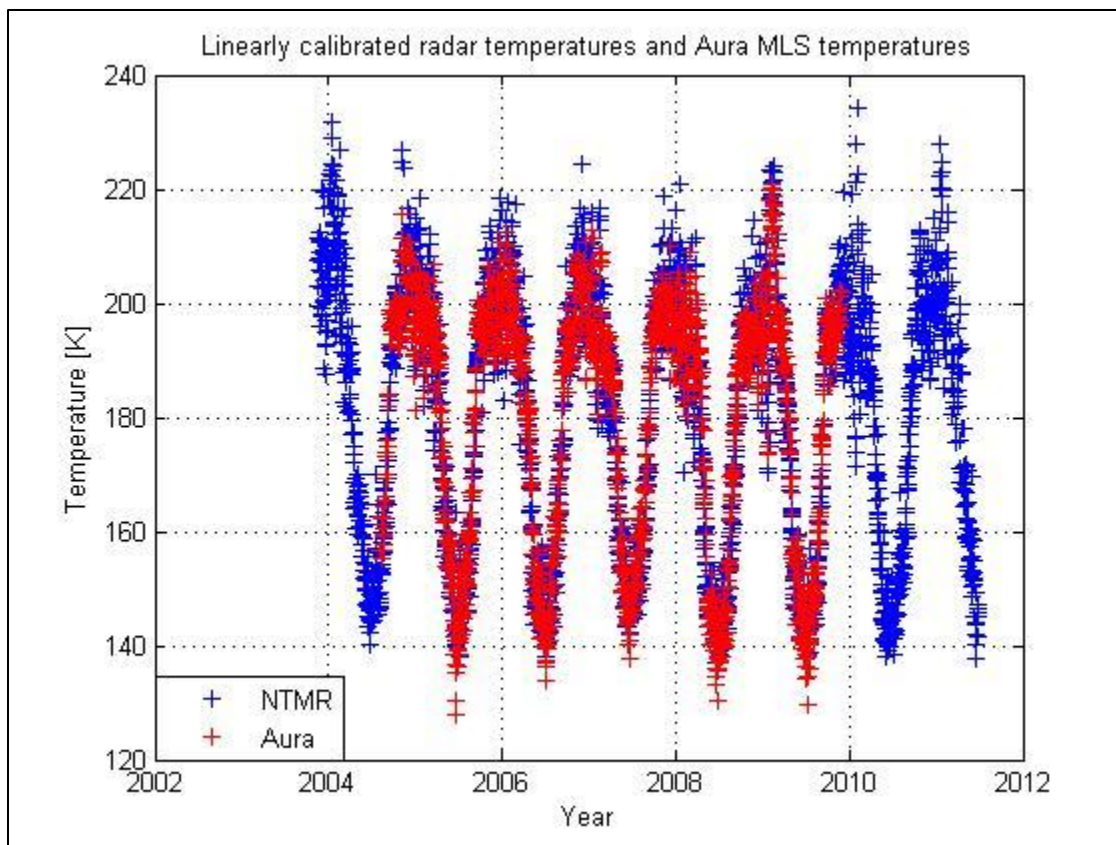
Figure 17: Comparison of the linearly calibrated radar temperatures and Aura MLS temperatures. The linear calibration lowers the temperatures to a level much closer to the Aura temperatures.

Now, performing the least squares regression on the linearly calibrated temperatures yields a standard deviation is ± 6.4 K. An important assumption in the least squares method is that the uncertainty is equal for all measurements. If this is a reasonable assumption the standard deviation can be used as an estimate of the uncertainty in the radar measurements, but it will only be correct if the Aura MLS temperatures are the true temperatures. Before the Aura MLS uncertainty is included in the analysis, two non-linear calibration techniques will be evaluated.

6.5 Nonlinear calibration

From the curved scatter plot in Figure 16 it was suggested that a non-linear regression could explain the relation between the two instruments better. In this chapter the regression will first be fitted to a second degree polynomial, and then an exponential curve.

The resulting second degree polynomial regression curve is shown in Figure 18 and has the following coefficients

$$T_{NTMR} = 0.0057 \cdot T_{AURA}{}^2 - 0.87 \cdot T_{AURA} + 154 \tag{38}$$

Solving this equation with respect to T_{AURA} yields the calibration Equation

$$T_{calibrated} = - \frac{0.87 - \sqrt{(4 * T_{NTMR} * 0.0057 - 4 * 0.0057 * 154 + 0.87^2)}}{2 * 0.0057} \tag{39}$$

A visual comparison of the linearly calibrated temperatures in Figure 17 and the polynomially calibrated temperatures in Figure 19 gives the impression that the polynomial calibration gives a better result.
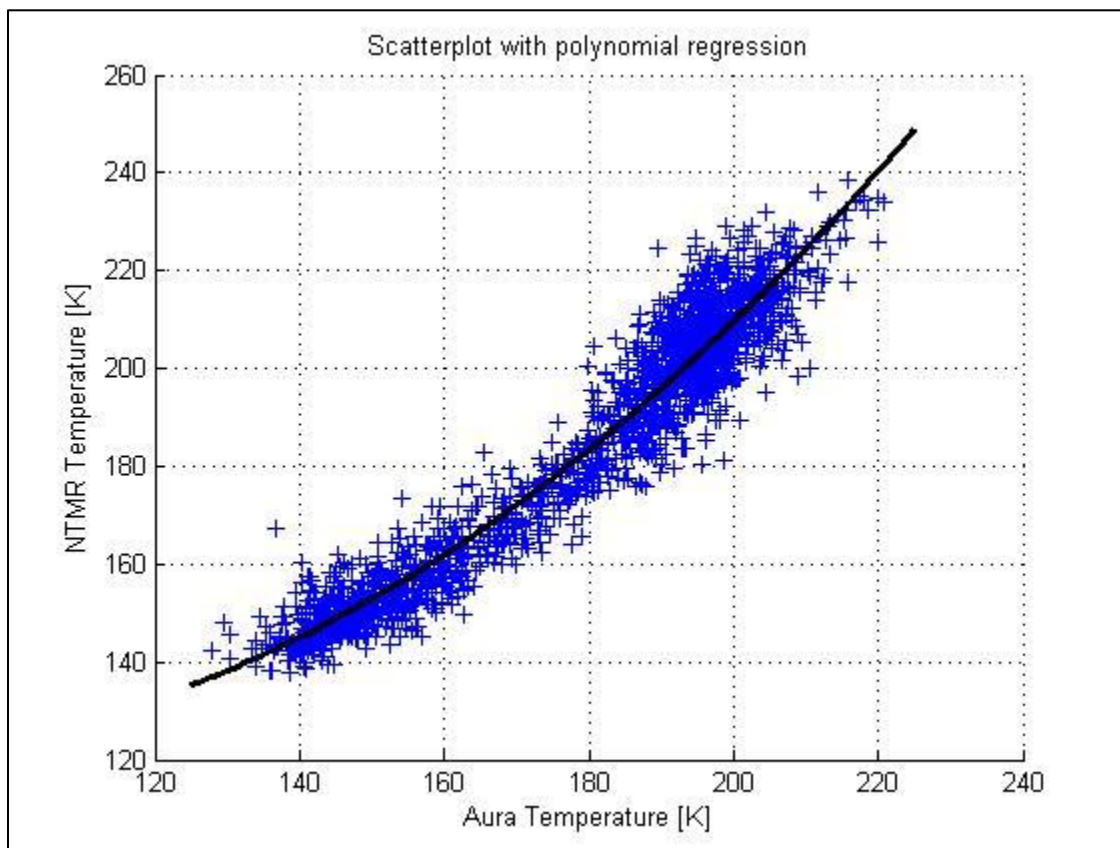

Figure 18: Scatterplot of the radar temperatures versus the Aura MLS temperatures. The black curve is the second degree polynomial regression curve.
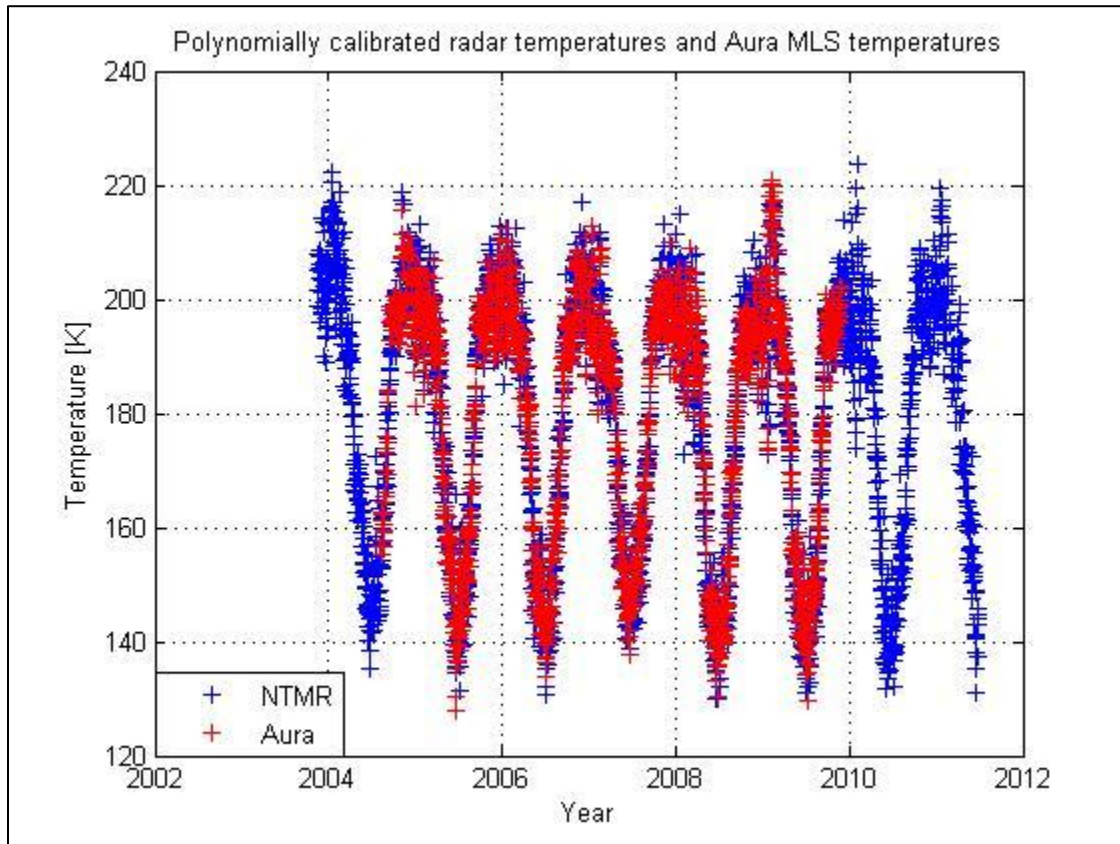
Figure 19: Comparison of the polynomially calibrated radar temperatures and the Aura MLS temperatures.

The coefficient of determination for the polynomially calibrated temperatures is 0.936 and the root mean square error is 5.7 K, which is 0.7 K lower than what was achieved with the linearly calibrated temperatures. The regression results confirm that the polynomial calibration gives a better result than the linear calibration.

Now, an exponential calibration will be examined. The exponential relation we seek is on the form $T_{NTMR} = A \cdot e^{B \cdot T_{Aura}}$, where A and B are the regression constants. The least squares method is very difficult to apply directly on this expression. Fortunately, the expression can be linearized by taking the natural logarithm of both sides. The standard least squares method can then be applied directly on the following expression $\log(T_{NTMR}) = \log(A) + B \cdot T_{Aura}$. One way to see the effect of such a calibration is to plot the logarithm of the radar temperatures

versus the Aura temperatures, as done in Figure 20. A visual inspection of the result shows that the relation between the temperatures is more linear in this case compared to the original scatterplot in Figure 16. It is therefore reasonable to expect an improvement relative to the linear calibration, but more details are needed in order to undergo a proper comparison.
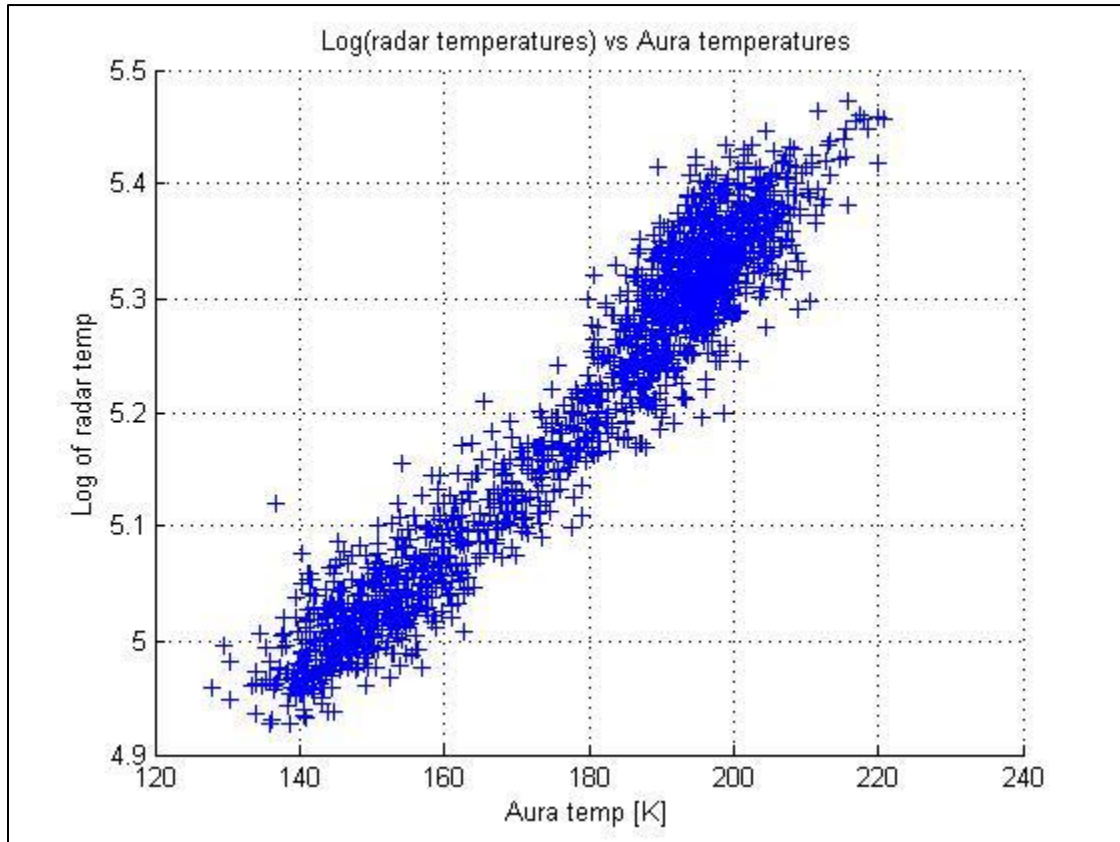

Figure 20: Scatterplot of the logarithm of the radar temperatures versus the Aura MLS temperatures

Applying the least squares method on the data in Figure 20 gives the following results:

$$\log(T_{NTMR}) = 4.1 + 0.0063 \cdot T_{AURA} \tag{40}$$

The exponential regression curve then becomes

$$T_{NTMR} = e^{4.1} \cdot e^{0.0063 \cdot T_{AURA}} \tag{41}$$

This regression curve is shown together with the scatter plot in Figure 21.
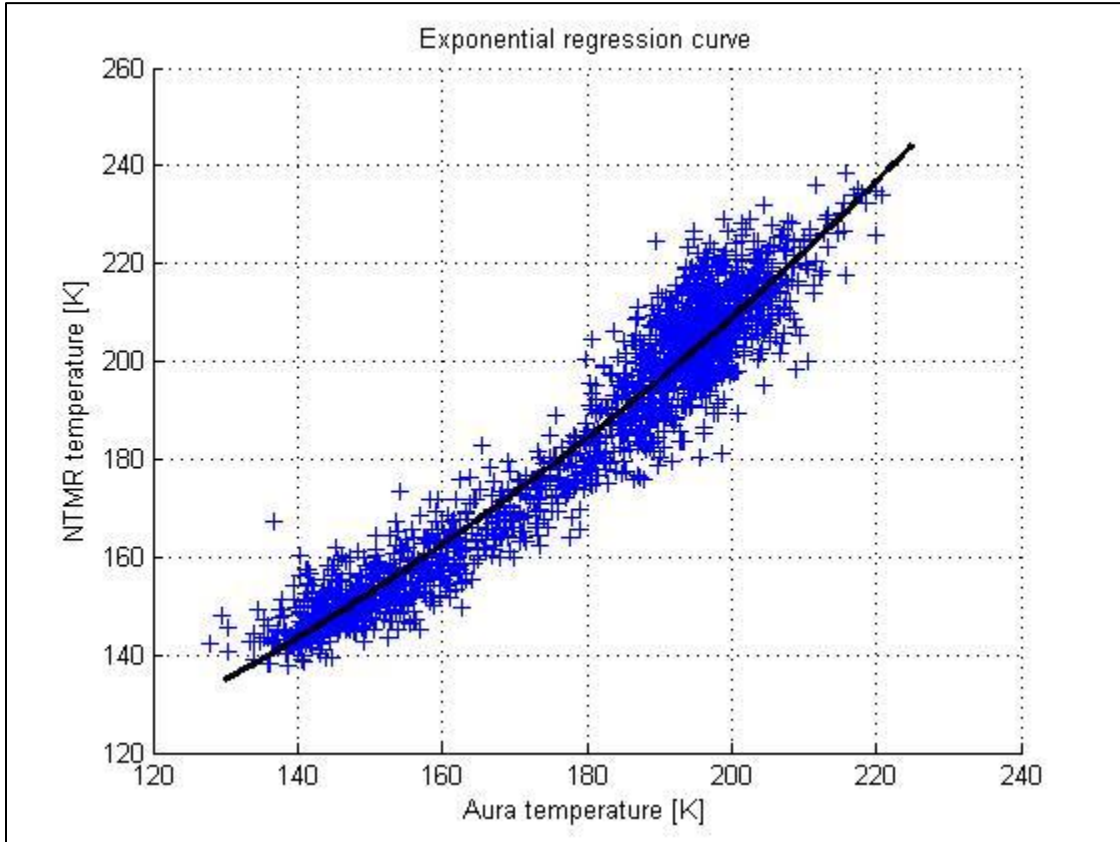

Figure 21: Scatter plot of NTMR temperatures and the Aura MLS temperatures with the corresponding exponential regression curve.

To obtain the calibration expression, Equation (41) is solved with respect to the Aura temperature to give

$$T_{Calibrated} = \frac{1}{0.0063} \cdot (\log(T_{Raw}) - 4.1) \tag{42}$$

The temperatures calibrated with this equation are plotted together with the Aura MLS temperatures in Figure 22. A regression analysis of the calibrated temperatures resulted in an

R^2 value of 0.932, which is slightly lower than the polynomially calibrated temperatures. The root mean square error from the Aura MLS Temperatures is ± 5.9 K
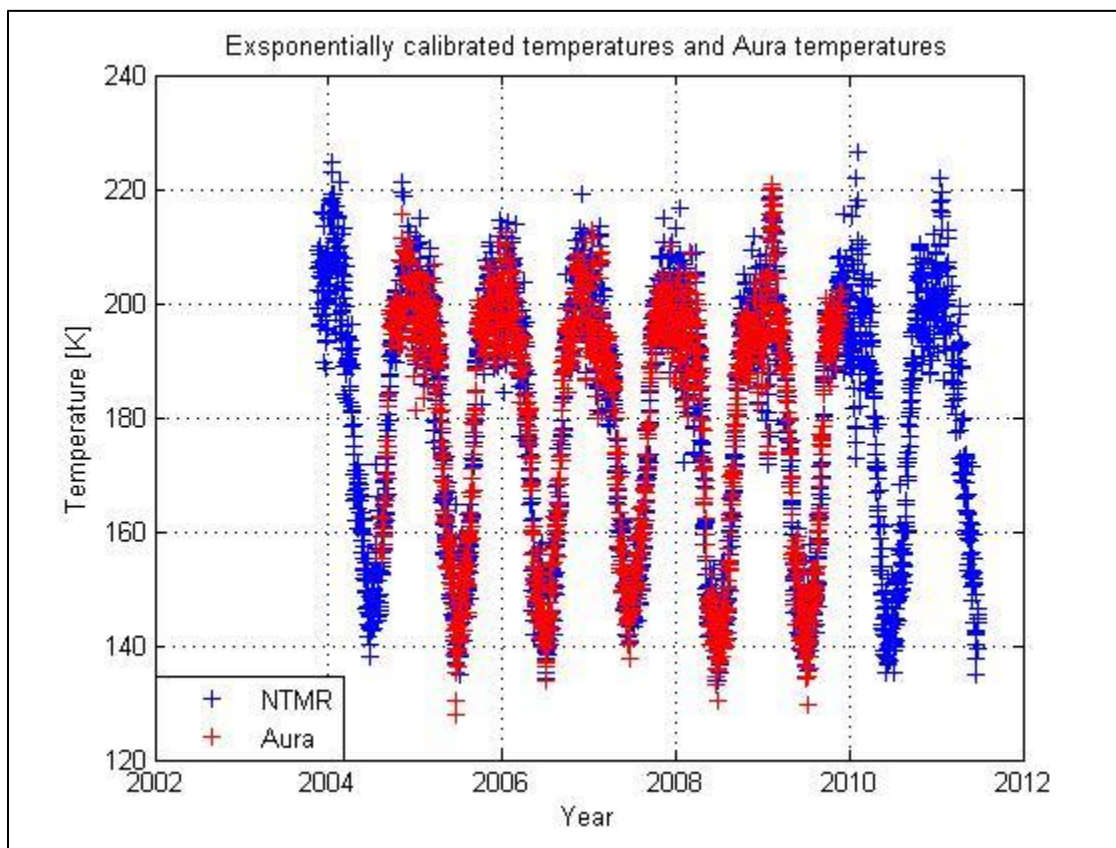

Figure 22: Exponentially calibrated temperatures compared to the Aura MLS temperatures.

An overview of the statistics for the different calibrations is presented in Table 3. Altogether, the polynomially calibrated temperatures gave the best result with the highest coefficient of determination and the smallest root mean squared error.

As mentioned earlier, the root mean squared error in Table 3 only represents the uncertainty of the radar measurements in the case where the Aura temperatures represent the true temperatures. By applying the statistical comparison technique from Chapter 5, a more correct value of the root mean squared error in the radar temperatures can be obtained. The root mean squared error of the polynomially calibrated temperatures is reduced to ± 4.5 K. The actual error will in fact be even lower because the deviations caused by the fact that the

instruments are not measuring the exact same area at the exact same period of time are still embedded in this value. It is very difficult to say how much this difference contributes to the total error, but the uncertainty estimate obtained with this method can be seen as an upper limit of the true intrinsic error of the radar.

Table 3: Summarization of regression results of raw and calibrated temperatures

Calibration method	R2	Root mean squared error [K]
None	0.920	7.2
Linear	0.920	6.4
Second degree	0.936	5.7
Exponential	0.932	5.9
Second degree with Aura error incorporated	0.936	4.5

6.6 Decay time limits

Hocking et al. (1997) and Holdsworth et al. (2006) applied several criteria to their data before the temperatures were calculated. Several of the criteria are similar to those used by the NTMR radar but a closer look at the raw data reveals that some of the measurements still have very unrealistic decay time values. Hocking (1997) excluded all measurements with decay times longer than 0.3 seconds or shorter than 0.025 seconds. The decay time definition used was half time amplitude decay, thus similar limits for the $\frac{1}{e}$ decay time would be a little longer. Holdsworth et al. (2006) on the other hand, used the values of 0.6 seconds and 0.02 seconds as the upper and lower decay time limits.

To investigate the effect of excluding very high or low values, a new temperature estimate is calculated with upper and lower limits on the decay time. The warmest temperatures reported by Aura MLS were around 220 K, and the coldest were about 130 K. To ensure that no realistic measurements are removed, only decay times resulting in temperatures higher than 300 K in the winter and lower than 50 K in the summer are rejected. The pressures in the winter and summer are approximately 0.18 and 0.12 Pa respectively. Inserting these temperatures and

pressure values into Equation (31) and (7) gives an upper decay time limit of 1.87 seconds and a lower limit of 0.078 seconds.

The raw temperatures produced with these criteria applied are shown in Figure 23. The result looks very promising, especially when looking at the highest temperatures. An R^2 value of 0.939 and a standard deviation of ± 5.8 K confirm that the temperatures produced with the decay time limits are considerably better than the ones produced without. When the statistical comparison method is used to incorporate the Aura MLS uncertainty, the estimate of the intrinsic error of the radar temperatures is reduced to ± 4.6 K

Again, the polynomial calibration is applied, and the resulting temperatures are presented in Figure 24. It is evident that there is less scatter in the temperatures this time. The red Aura MLS temperatures almost completely cover the blue radar temperatures. The root mean square error has decreased to ± 5.1 K. The coefficient of determination has also improved, now indicating that the linear regression explains 94.8 % of the relation between the polynomially calibrated Radar temperatures and the Aura MLS temperatures. By applying the statistical comparison technique on the calibrated temperatures, the standard deviation is estimated to ± 3.8 K. The intrinsic uncertainty of the radar measurements is therefore estimated to be less than 4 K. The regression results are summarized in Table 4, along with the results obtained without decay time limits for comparison. It should be noted that the uncertainty estimate of the radar temperatures is only valid if the uncertainty in the Aura MLS measurements is ± 3.5 K. For example, if the Aura MLS uncertainty is overestimated, then the radar uncertainty will be underestimated.

Experiments with other decay time limits found that the results were moderately sensitive to the value of the chosen limits. As stated earlier, Hocking et al. (1997) and Holdsworth et al. (2006) used two differet sets of limits for two different radars. This might be an indication that the decay time limits have to be specified for the particular radar systems, and may be viewed as a part of the calibration of the radar.
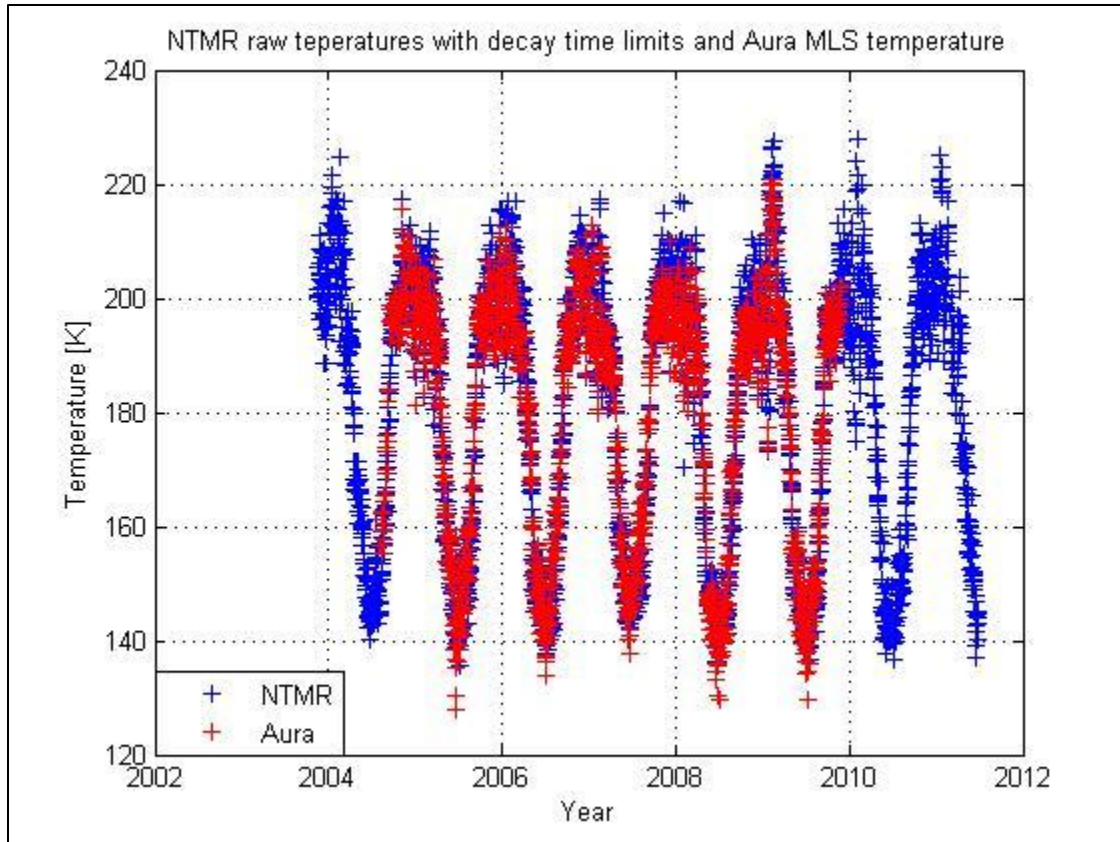
Figure 23: Comparison of radar versus Aura MLS temperatures. Uppper and lower decay time limits have been aplied to the radar data. There is less variation compared to the case without limits, especialy in the winter.
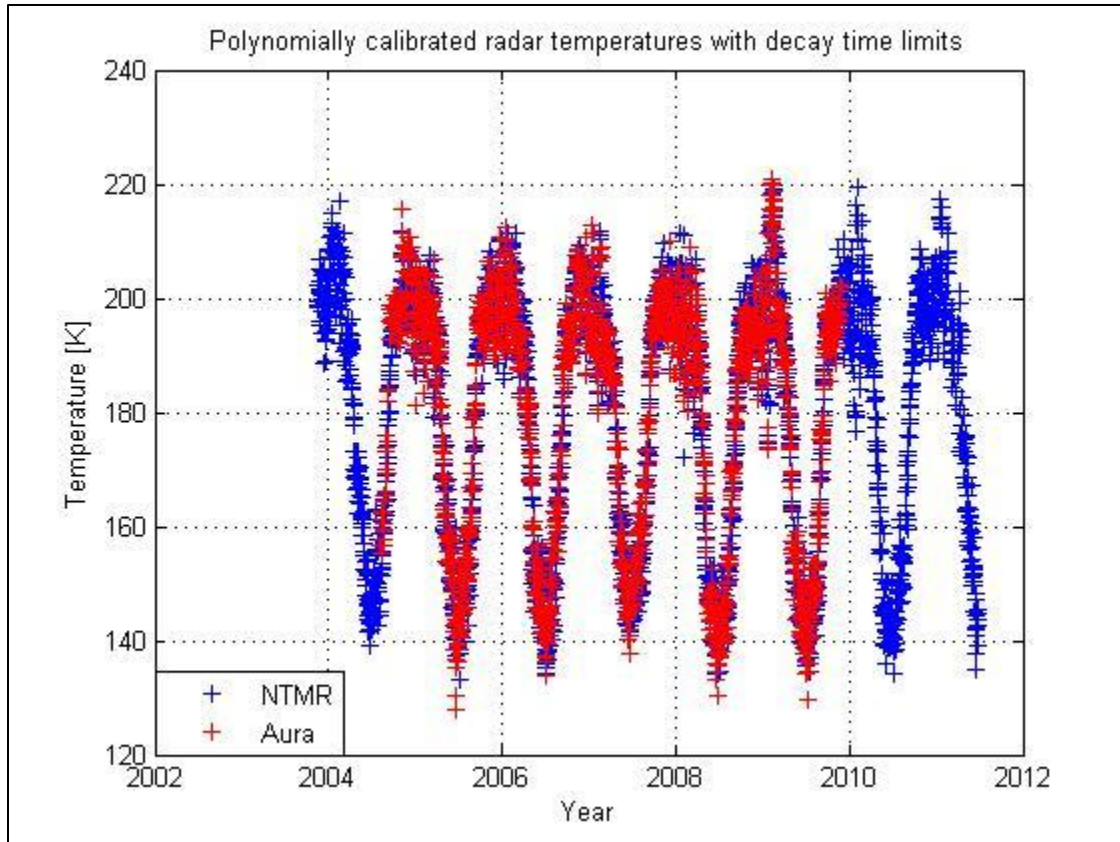
Figure 24: Polynomially calibrated radar temperatures produced with decay time limits plotted together with the Aura MLS temperatures for comparison.

Table 4: The coefficient of determination R^2 and root mean square error for the temperatures calculated with upper and lower decay time limits. In the bottom part the values obtaind withouts decay time limits are reprinted for comparison.

	Calibration method	R^2	Root mean square error [K]
With decay time limits	None	0.939	5.8
	None - With Aura error incorporated	0.939	4.6
	Second degree polynomial	0.948	5.1
	Second degree - with Aura error incorporated	0.948	3.8
Without decay time limits	None	0.920	7.2
	Second degree polynomial	0.936	5.7
	Second degree with Aura error incorporated	0.936	4.5

6.7 Pressure and ion mobility induced error

In this section the error introduced by the pressure model and the reduced ion mobility K_0 will be discussed. The error caused by the estimate of the decay time and thereby D_a is assumed to be zero.

The equation for the squared error in the temperature is

$$\delta T^2 = \left| \frac{d}{dP} T \right|^2 \cdot \delta P^2 + \left| \frac{d}{dK_0} T \right|^2 \cdot \delta K_0^2, \tag{43}$$

where the errors are assumed to be random. It is also very likely that both the pressure models and the reduced ion mobility have systematic error components. Now, with the use of Equation (31) the above expression becomes

$$\delta T^2 = \left| \frac{\partial}{\partial P} \sqrt{\frac{D_a \cdot P}{K_0 \cdot 6.39 \cdot 10^{-2}}} \right|^2 \cdot \delta P^2 + \left| \frac{\partial}{\partial K_0} \sqrt{\frac{D_a \cdot P}{K_0 \cdot 6.39 \cdot 10^{-2}}} \right|^2 \cdot \delta K_0^2 \tag{44}$$

The error in the temperature is then found by solving the partial differentials and taking the square root on both sides

$$\delta T = \left(\left| \frac{1}{2} \cdot \sqrt{\frac{D_a}{K_0 \cdot 6.39 \cdot 10^{-2} \cdot P}} \right|^2 \cdot \delta P^2 \right.$$

$$\left. + \left| \sqrt{\frac{D_a}{K_0^{\frac{3}{2}} \cdot 6.39 \cdot 10^{-2} \cdot P}} \cdot -\frac{1}{2} \right|^2 \cdot \delta K_0^2 \right)^{\frac{1}{2}} \tag{45}$$

With little knowledge about the standard deviation of either the pressure or the reduced ion mobility, the error introduced by a standard deviation of 5 % in both is calculated. With the use of Equation (45), this corresponds to a relative error of 3.5 % in the temperature. Since the

temperatures vary with the season, the magnitude of the error will also vary with the season. The size of the error is therefore calculated for both the winter and the summer conditions. The standard deviation in the temperatures is in this case ± 8 K in the winter, and ± 5 K in the summer.

The disadvantage of using a pressure model is that it cannot take short time scales variations into account. This will definitely introduce random errors in the pressure, even if the average values of the models are correct. There are very few measurements of the pressure at this altitude, especially of variations on short timescales. It is therefore very hard to say anything about what kind of spatial and temporal variations that could be expected. The pressure at ground level is not likely to change with more than 3 % within a day, and a similar variation in the meteor region would result in a temperature error of 1.5 % or a maximum of 3.3 K in winter. The systematic error in the pressure model is unfortunately even more difficult to estimate. In section 6.2.3 it was suggested that the pressure model most probably is more accurate in the summer, thus implying that the systematic error will vary with the season.

The value of the reduced ion mobility factor depends on the ion composition of the meteor trail. The content of the incoming meteors is likely to vary and therefore introduce random errors. Holdsworth et al. (2006) found that there was a bias in the temperatures during the Southern Delta Aquariids meteor shower. This bias might occur because the meteors in this shower have a different composition and therefore create trails with different ion mobilities.

As discussed in section 6.1, the reduced ion mobility values used by different authors spans from $1.9 \cdot 10^{-4} \, m^2 s^{-1} V^{-1}$ to $2.5 \cdot 10^{-4} \, m^2 s^{-1} V^{-1}$. The majority of the authors agree on the latter value, but in a worst case scenario where the true value is off by $0.6 \cdot 10^{-4}$, the systematic error in the temperature would be 14 % or about 30 K in the winter. The temperatures produced previously had uncertainties far less than this, making such a large offset highly unlikely. Even so, the reduced ion mobility might be the source of a systematic error.

Table 5: Numerically calculated temperature errors based on a 5 % error in both the pressure and the reduced ion mobility. The errors were calculated for the winter of 2006/2007 and the summer of 2007.

	June and July 2007	Dec 2006 and Jan 2007
Mean diffusion coefficient [m^2/s]	2.6	5.1
Mean temperature [K]	152	223
Mean pressure [Pa]	0.124	0.16
δT from 5 % error in both P and K_0	5 K	8 K
Relative error	3.5 %	3.5 %

Chapter 7: Temperature gradient based method

The second method for obtaining neutral temperatures with the meteor radar is called the temperature gradient method. The advantage of this technique is that it does not depend on knowledge of the pressure. However, as the name implies, it does require the mean vertical temperature gradient. The resulting temperature, called TG-temperature from now on, is a weighted average over the height distribution of meteors. This is commonly accepted to represent the height of maximum meteor occurrences (e.g. Hocking, 1999; Holdsworth, et al., 2006; Kumar, 2007). The altitude of the temperatures produced by this method will therefore vary with the peak of the meteor height distribution, but the temperatures may be adjusted to 90 km altitude if the deviations are small. The mean peak height in the period from 2004 to 2010 was 90.3 km, and the standard deviation was 0.8 km. The peak height is therefore very close to 90 km for the frequency of this radar, and should therefore be ideal to produce temperatures at 90 km altitude.

7.1 Derivation of the temperature

The derivation of this technique was first done by Hocking (1999), and it begins with the result of the pressure based method, namely Equation (31):

$$T = \sqrt{\frac{D_a \cdot P}{K_0 \cdot 6.39 \cdot 10^{-2}}} \qquad (46)$$

The technique is based upon expressing the temperature as a function of height with the use of the vertical temperature gradient and the temperature at the peak height (T_0).

$$T(z') = T_0 \left(1 + \frac{1}{T_0} \frac{dT}{dz'} z' \right) \qquad (47)$$

Here the vertical coordinate z' is introduced, which is the height defined to be zero at the meteor peak height. The pressure can then be expressed by the hypsometric equation as

$$P(z') = P_0 \cdot e^{-\int_0^{z'} \frac{mg}{kT(z'')} dz''} \tag{48}$$

This equation assumes that both the temperature and gravity are constant. While this is a good approximation for the gravity, it is clear that the temperature will vary. Hocking (1999) justified the use of this assumption by arguing that the pressure changes much faster with height than the temperature. Now, substituting the expression for the temperature into the hypsometric equation gives

$$P(z') = P_0 \cdot e^{-\int_0^{z'} \frac{mg}{kT_0\left(1+\frac{1}{T_0}\frac{dT}{dz'}z'\right)} dz''} \tag{49}$$

The next steps are to square Equation (46) to avoid the square root and to insert the expressions for the pressure and temperature. Then, taking the natural logarithm of both sides gives

$$2 \cdot \log\left(T_0\left(1 + \frac{1}{T_0}\frac{dT}{dz'}z'\right)\right) = \log(D_a) + \log(e) \cdot \frac{mg}{k} \int_0^{z'} \frac{1}{T_0\left(1 + \frac{1}{T_0}\frac{dT}{dz''}z''\right)} dz'' + C, \tag{50}$$

where C is the constant $\log(K_0 \cdot 6.39 \cdot 10^{-2}) + \log(P_0)$. The next move is to rearrange the equation such that D_a is left on the side.

$$\log(D_a) = 2 \cdot \log\left(T_0\left(1 + \frac{1}{T_0}\frac{dT}{dz'}z'\right)\right) + \log(e) \cdot \frac{mg}{k} \int_0^{z'} \frac{1}{T_0\left(1 + \frac{1}{T_0}\frac{dT}{dz''}z''\right)} dz'' + C \tag{51}$$

The final steps are to differentiate this Equation with respect to z' and then evaluate it at the peak height z'=0.

$$\frac{d\log(D_a)}{dz'} = \frac{2}{\left(T_0\left(1+\frac{1}{T_0}\frac{dT}{dz'}z'\right)\right)} \cdot \log(e) \cdot \frac{dT}{dz'}$$

$$+ \log(e) \cdot \frac{mg}{k} \int_0^{z'} \frac{\frac{dT}{dz''}}{\left(T_0\left(1+\frac{1}{T_0}\frac{dT}{dz''}z''\right)\right)^2} dz''$$

(52)

Evaluating at z'=0 gives

$$\frac{d\log(D_a)}{dz'} = \frac{2}{T_0} \cdot \log(e) \cdot \frac{dT}{dz'} + \log(e) \cdot \frac{mg}{k} \int_0^{z'} \frac{\left(\frac{dT}{dz''}\right)_0}{{T_0}^2} dz''$$

$$= \frac{2}{T_0} \cdot \log(e) \cdot \frac{dT}{dz'} + \log(e) \cdot \frac{mg}{k} \cdot \frac{1}{{T_0}^2} \int_0^{z'} \left(\frac{dT}{dz''}\right)_0 dz''$$

(53)

$$= \frac{2}{T_0} \cdot \log(e) \cdot \frac{dT}{dz'} + \log(e) \cdot \frac{mg}{k} \cdot \frac{1}{T_0}$$

The value of the expression on the left side can be estimated from the slope of the scatterplot of log (D_a) versus z'. This value is commonly called $\frac{1}{S_m}$, where the subscripted m stands for mean. Finally, the temperature can be found by rearranging Equation (53) with respect to the temperature

$$T_0 = S_m\left(2\cdot\frac{dT}{dz'} + \frac{mg}{k}\right) \cdot \log(e)$$

(54)

7.2 Calculating S_m

Since $\frac{1}{\tau}$ is proportional to D_a, the gradient S_m can be found by calculating the best fit line from a scatterplot of height versus log (D_a) or $\log\left(\frac{1}{\tau}\right)$. In Figure 25 the latter is used to produce an example of such a scatterplot with data from the entire period the radar has been operating. A large portion of the scatter stems from natural seasonal variation, but even without the seasonal variations there are substantial amounts of scatter in the data. Therefore, several thousands of meteors are needed in order to get a reliable estimate of S_m (Singer, et al., 2004b). As previously mentioned, the NTMR radar has since its inception detected on average more than 12,000 usable meteors per day, and should therefore be capable of producing good temperature estimates with the temperature gradient technique.
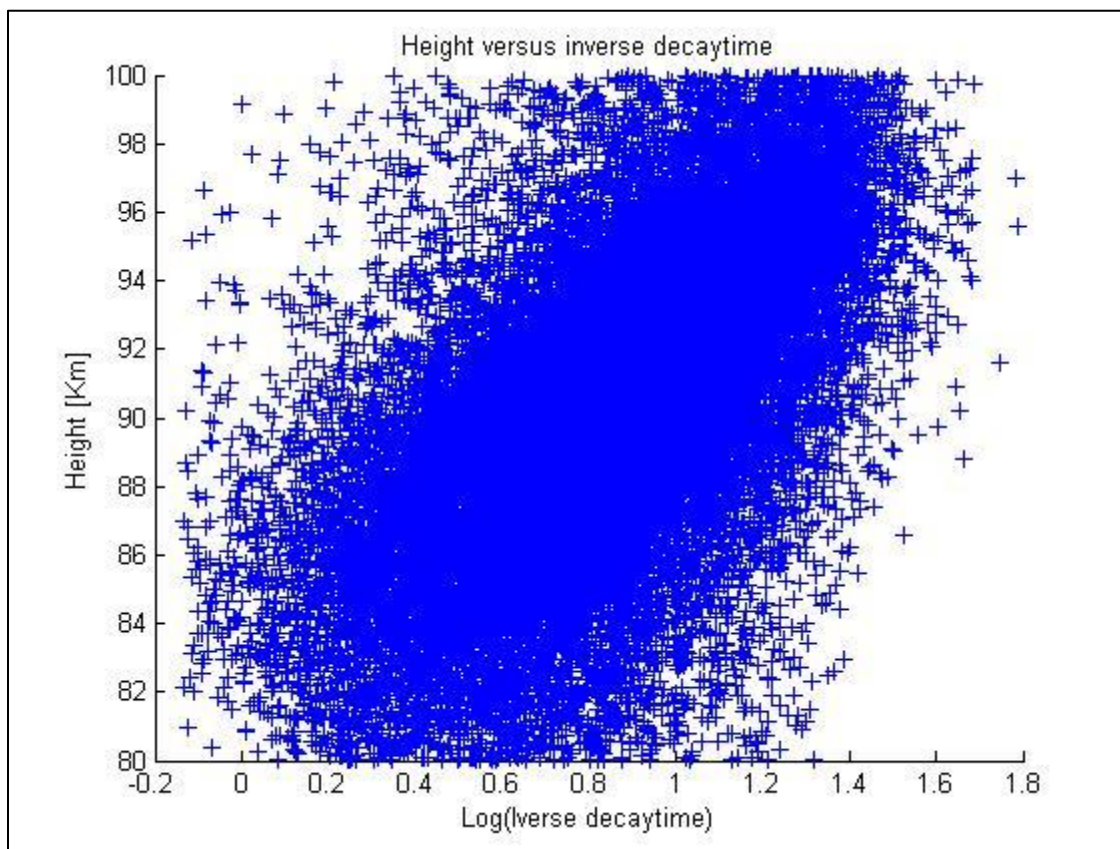

Figure 25: Example of a scatterplot of height versus log $\left(\frac{1}{\tau}\right)$. The data in the plot span the period from September 2003 to June 2011. A large portion of the scatter stems from natural seasonal variation.

Hocking et al. (1997) pointed out that various instrumental errors will lead to errors to the measured heights. In order to compensate for these errors a method for bias adjustment was introduced. Holdsworth et al. (2006) used the statistical comparison technique from Chapter 5 instead of the bias adjustment, arguing that the method takes the height measurement error directly into account when making the fit. This approach is adopted here, since the statistical comparison technique is easy to apply and works as both bias adjustment and regression analysis in one. A disadvantage with both methods is that the value of the slope S_m depends on the assumed errors in the height and the decay time measurements. Greater uncertainty in log $\left(\frac{1}{\tau}\right)$ increases the value of S_m which results in higher temperatures.

Daily average temperatures will be produced in order to easily compare the result with the temperatures produced with the pressure method. In addition to the data criteria used in the pressure based method, all meteors above 100 km are discarded because the magnetic field is likely to affect the trail diffusion at these heights (Dyrud et al., 2001). The daily average correlation coefficient of height versus log $\left(\frac{1}{\tau}\right)$ for the NTMR radar was 0.71, which is very similar to results reported by Hocking (2004) and others.

7.3 Gradient model

All that remains in order to calculate the temperatures with Equation (54) is the vertical temperature gradient. As with the pressure, the knowledge about the temperature gradient is very limited. Again, a model has to be used in the lack of better options. The falling sphere measurements that were used to obtain the pressure model can also be used to derive a gradient model. Unfortunately, some of the temperature profiles in Lübken and von Zahn (1991) stop at 90 km, thus impeding the calculation of gradients at 90 km. Since there were fewer measurements in the winter to begin with, one would expect poor accuracy in the winter season with this model.

In the search for an alternative gradient model, Doctor Werner Singer at the Leibniz-Institute of Atmospheric Physics was contacted. He has applied the temperature gradient technique to data

from a meteor radar at Andøya, the same location as the falling sphere measurements. Doctor Singer supplied the gradient model used in the Singer et al. (2004b) paper, which will be called the Singer model hereafter. This model is an adjusted version of a gradient model for mid-latitudes that has been cross-checked with the falling sphere climatology (W. Singer, personal communication, July 8, 2011). For comparison, the gradients are also obtained from the MSIS-E90 model. All three models are shown in Figure 26. The Singer gradients are generally of lower value than both the MSIS-gradients and the FS-gradients, especially in the summer. This is somewhat surprising since the Singer model has been cross-checked against the falling sphere climatology. Both the MSIS-gradients and the Singer gradients display a smooth seasonal variation, but the FS-gradients clearly suffer from an insufficient number of measurements. Also, the FS-gradient model has some inconsistencies in April and October, where the measurements from two campaigns are joined.
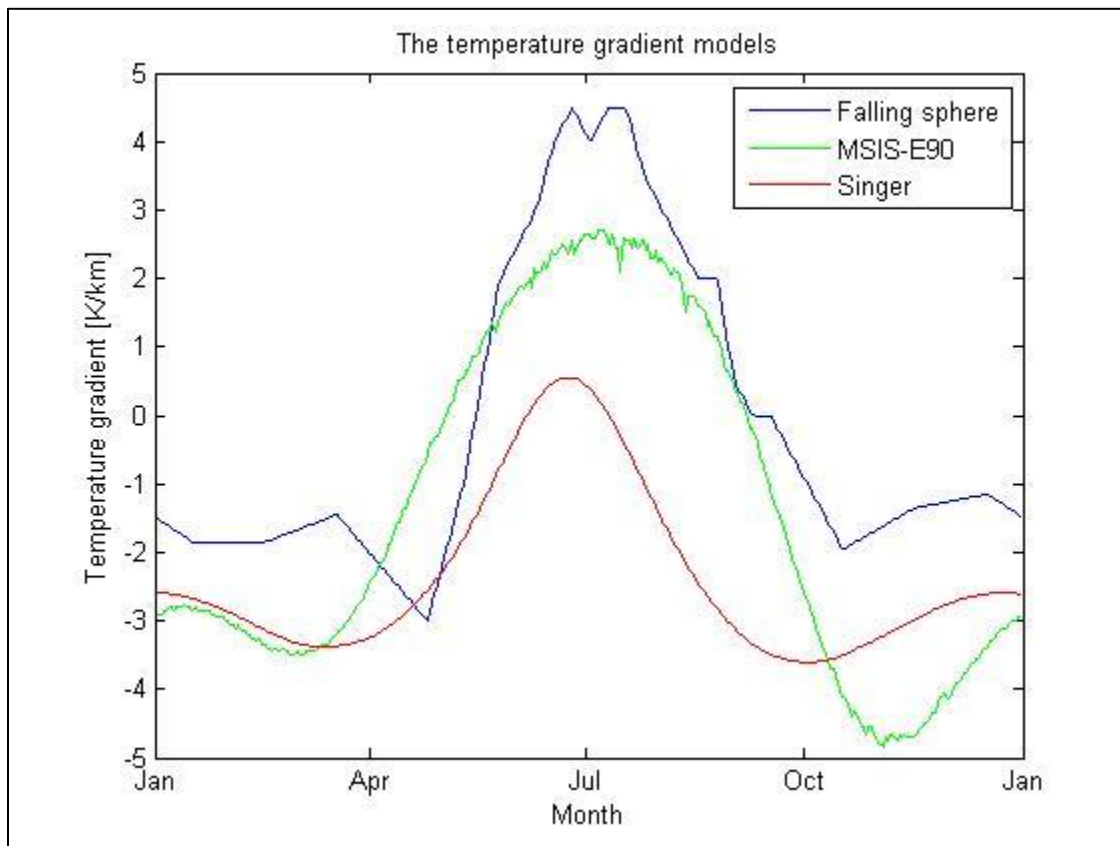

Figure 26: The three gradient models for 90 km altitude above the radar.

7.4 Calculating the temperatures

Before the temperatures are calculated one issue with the method has to be addressed. As previously mentioned, the value of the slope S_m will depend on the assumed uncertainty in the height and decay time measurements. Since the gradient models have large deviations, there will not be one set of uncertainties suiting all the models. A good estimate of the uncertainties should therefore make it possible to determine which gradient model is better. With the use of the statistical comparison technique from Chapter 5 an estimate of one of the uncertainties will allow for the determination of the other uncertainty and the bias adjusted slope.

Because little information on the uncertainty of the decay time measurements is available, an attempt to estimate the uncertainty in the height measurements will be conducted. The uncertainty in height will depend on the pulse length and the angular resolution of the radar. Unfortunately, the uncertainty caused by the pulse length of the radar is not straightforward, because the radar beam consists of two 4-bit coded pulses. Holdsworth and Reid (2002) stated that the transmited pulse length is between 100 to 4000 meters long. With little detailed information on the uncertainties of either the pulse length or the angular resolution, the values of 2 km and 1.5° respectively will be assumed in order to proceed. With the help of Figure 27 the height uncertainty caused by the pulse length can be found as $2\ km \cdot cos(\theta)$, where θ is the angle between zenith and the meteor. The height H of a measurement can be calculated as $R \cdot \cos(\theta)$, where R is the range given by $H/cos(\theta)$. The height difference caused by a change in angle of δθ is then

$$\delta H_\theta = R \cdot \cos(\theta) - R \cdot \cos(\theta + \delta\theta) = \frac{H}{\cos(\theta)}(\cos(\theta) - \cos(\theta + \delta\theta)) \qquad (55)$$

The mean height is 90 km and the mean zenith angle observed at all heights is very close to 50°. The height uncertainty caused by the pulse length at this average angle is ± 1.3 km and the uncertainty caused by an angular error of 1.5° is 2.8 km. Adding these two uncertainties gives

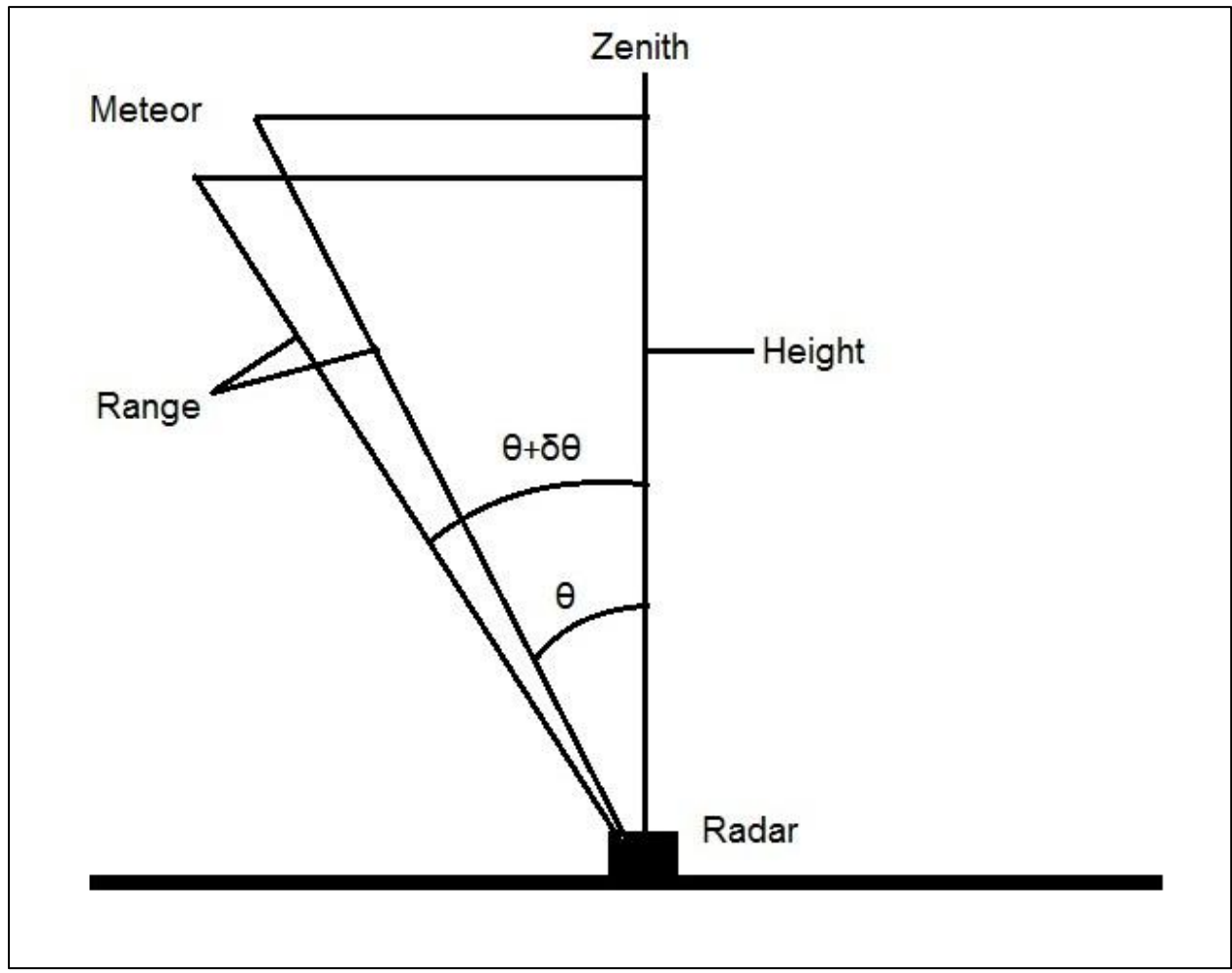$$\delta H = \sqrt{1.3^2 + 2.8^2} = 3.1 \; km \tag{56}$$

Figure 27: Sketch of parameters used to estimate the height uncertainty of the radar.

In Figure 28 the temperatures calculated with the height uncertainty of 3.1 km and the FS-gradient model are presented. The temperatures are extremely high. In fact, the errors are so large that they cannot be caused by an improper gradient model alone. It can only be assumed that the attempt to estimate the height uncertainty failed.

The uncertainty of ± 3.1 km in height corresponded to an uncertainty of ± 0.23 in $\log\left(\frac{1}{\tau}\right)$.
Holdsworth et al. (2006) used an error of ± 0.14 for the measurement of $\log(D_a)$, where D_a has the units of m^2/s. Adopting this lower value should result in considerably lower temperatures since a lower uncertainty will decrease the values of S_m. First the temperatures are produced with this uncertainty and the FS-gradient model, and then the temperatures are the adjusted to 90 km height. Figure 29 shows that the temperatures are much lower this time. In Figure 30 the temperatures calculated with the same uncertainty and the Singer gradient model are plotted. Neither of the gradient models gives very good results, but the adopted measurement uncertainty greatly improves the temperature estimates. The temperatures acquired with the MSIS-gradients were far inferior and are therefore omitted in the text.

The uncertainty of ± 0.14 in $\log\left(\frac{1}{\tau}\right)$ corresponds to an uncertainty of ± 4.5 km in height. This means that a difference in height uncertainty of 1.4 km results in two tremendously different temperature estimates. The method is therefore very sensitive to the assumed uncertainties of the instrument.
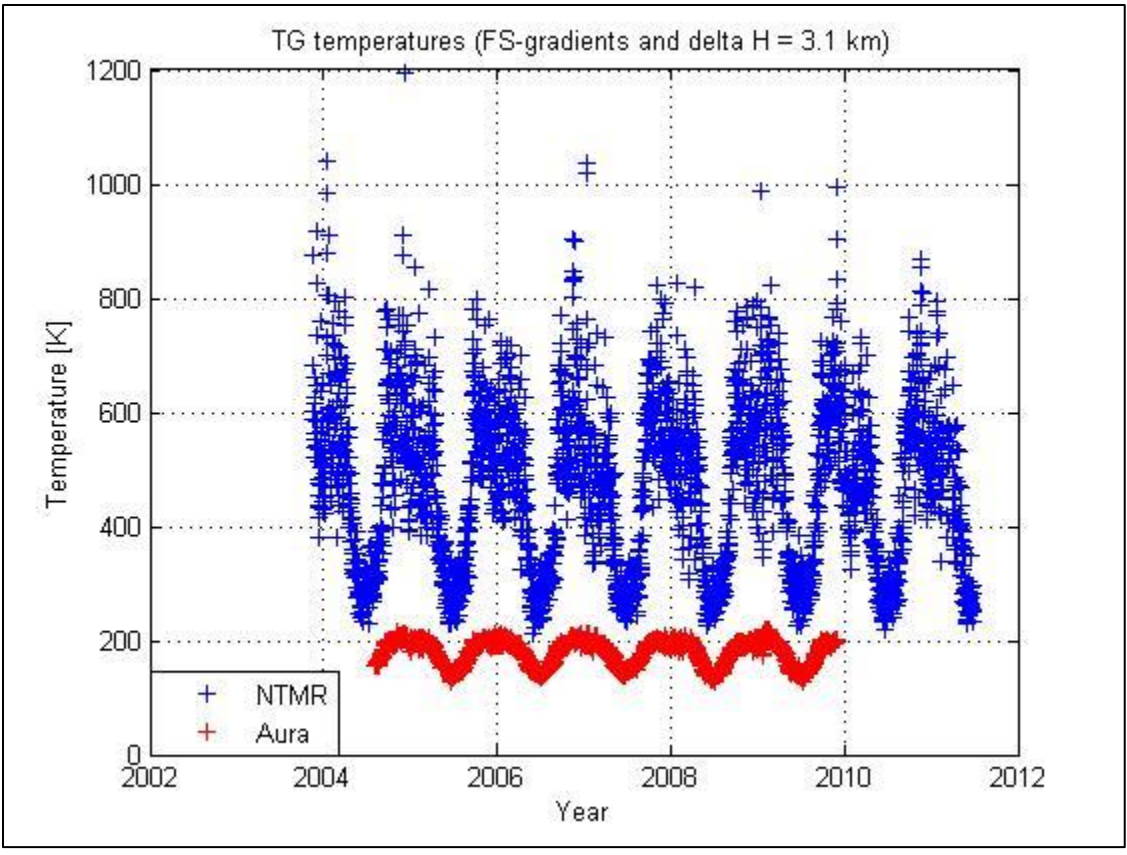
Figure 28: TG temperatures produced with the FS-gradients and an uncertainty in the height measurements of ±3.1 km. The radar temperatures are overestimated by several hundred Kelvin.
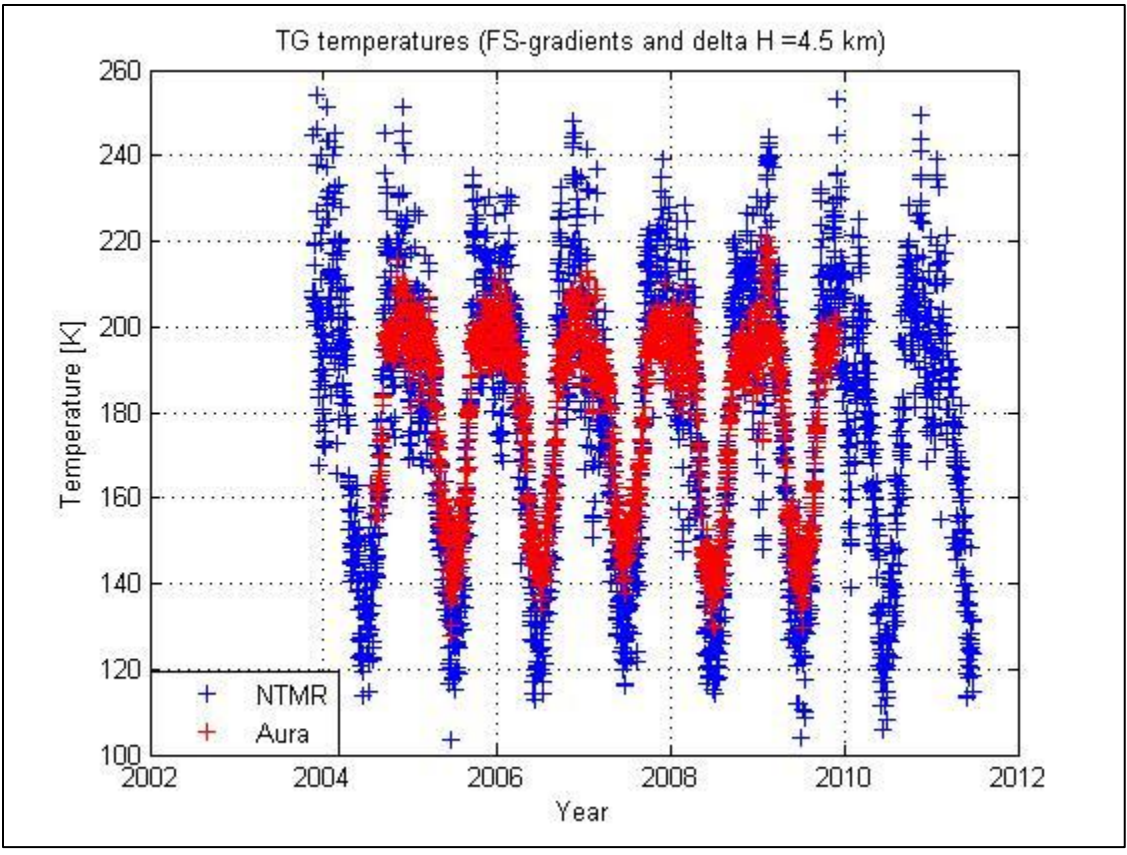
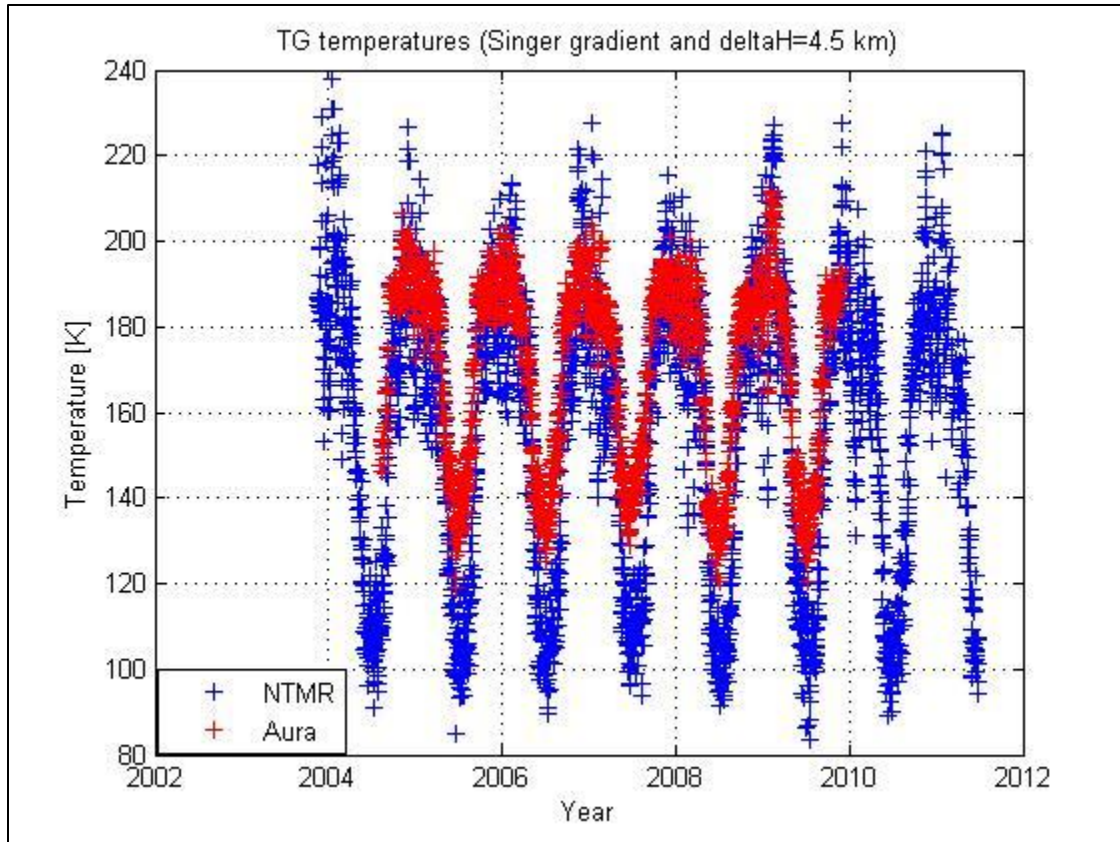Figure 29: TG temperatures produced with the FS-gradients and an uncertainty in the height measurements of ±4.5 km.

Figure 30: TG temperatures produced with the Singer gradient model and a height uncertainty of ± 4.5 km.

Both gradient models give initial temperatures which are underestimated in the summer and overestimated in the winter, but the coefficient of determination is relatively good in both cases. The highest value of 0.89 was obtained with the Singer model, while the FS-gradient model gave a value of 0.86. The Singer model temperatures gave the best result after calibration. The calibrated temperatures, shown in Figure 31, have a standard deviation of 7.4 K and a coefficient of determination of 0.90. The details of the comparison of the TG temperatures against the Aura temperatures are listed in Table 6.

Table 6: Statistical comparison of TG temperatures against the Aura MLS temperatures

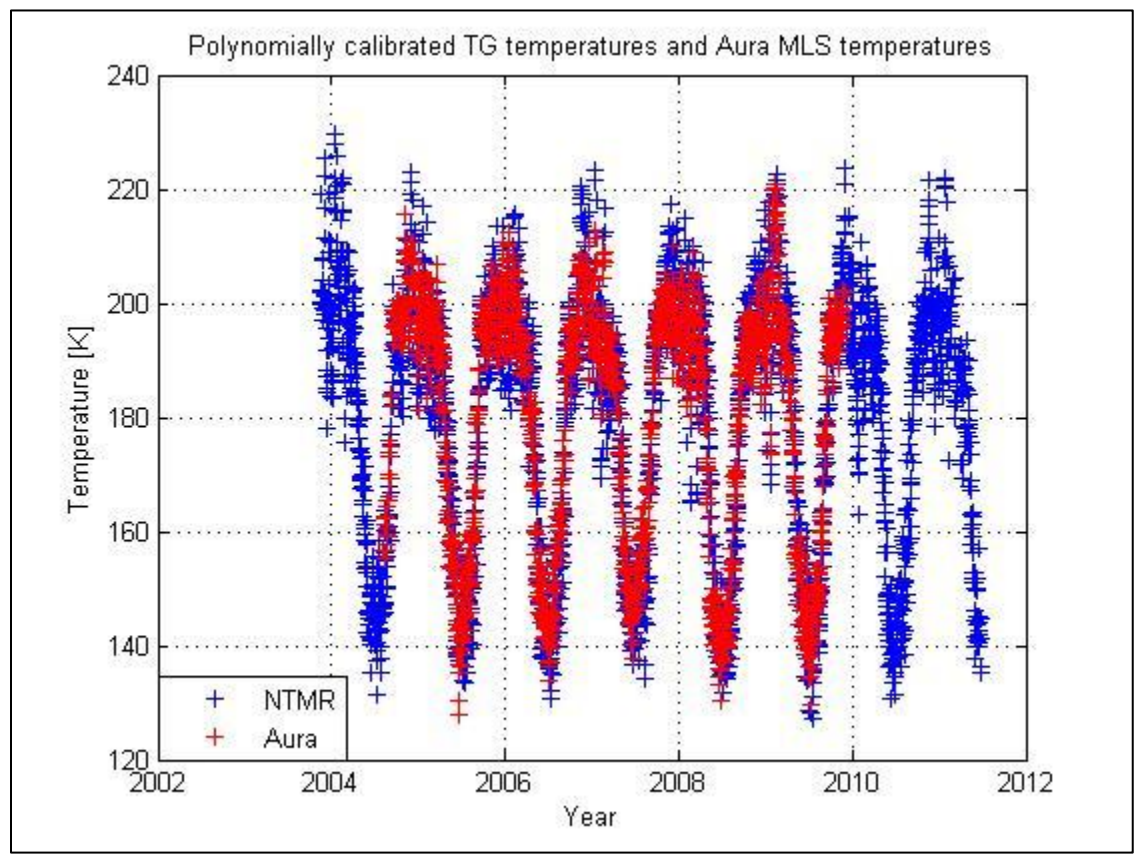| Gradient Model	Calibration	R^2	RMSE [K]
Falling spheres	None	0.86	12.7
Falling spheres	Polynomial	0.86	8.6
Singer	None	0.89	11.7
Singer	Polynomial	0.90	7.4

Figure 31: Polynomially calibrated TG temperatures produced with the Singer gradient model compared to the Aura MLS temperatures.

Chapter 8: Combining the methods

In the two previous chapters the temperature at 90 km has been calculated by two independent methods. A disadvantage to the methods is that they depend on input data from other instruments or models. The pressure method for example, needed a pressure model in order to work. Such a model will not be able to take into account any variations from the mean, such as day to day variations or long term changes like climate change. In this chapter, the possibility of combining the gradient method and the pressure method into one self-sustained method will be outlined.

One possible approach is to start by creating height dependent temperatures with the pressure method, and then use these temperatures to estimate the vertical temperature gradients needed by the gradient method. Even though a pressure model would be used initially, the resulting temperature gradients would incorporate both short and long changes inherited from the measured decay times. Thereafter, the temperatures are calculated with the gradient method. The pressure could then be estimated by inserting these temperatures and the measured ambipolar diffusion coefficients into Equation (31). One could also picture an iterative process wherein the estimated pressure is used to adjust the pressure model used initially. Unfortunately, my attempts to create height dependent temperatures with the pressure method failed. Both the MSIS-pressure and the FS-pressure gave temperature gradients which were strongly negative at all heights, which clearly is wrong since temperatures increase with increasing height above the mesopause.

Another way to combine the methods is to first calculate the temperatures with the gradient method and then use the ideal gas law to estimate the pressure at 90 km. A model of the particle number density is needed in order to calculate the pressure with the ideal gas law. This pressure estimate can then be used to calculate the temperatures with the pressure method. The advantage of these methods is that they obtain both the pressure and the temperature at the same time.

First, the TG temperatures and the falling sphere mass densities are used to estimate the
pressure shown in Figure 32. A lot of the variability stems from the uncertainty in the
temperature measurements. The TG-pressure is compared to the FS-pressure model estimated
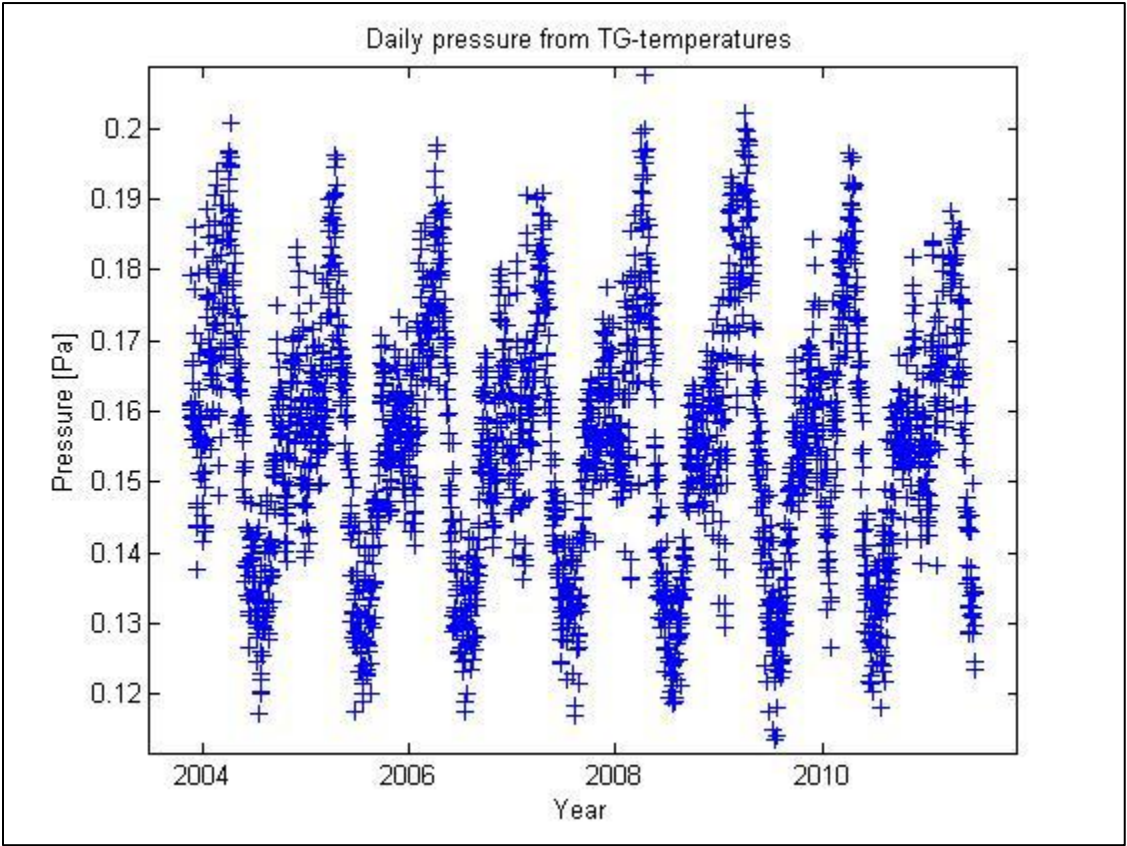in Chapter 6.

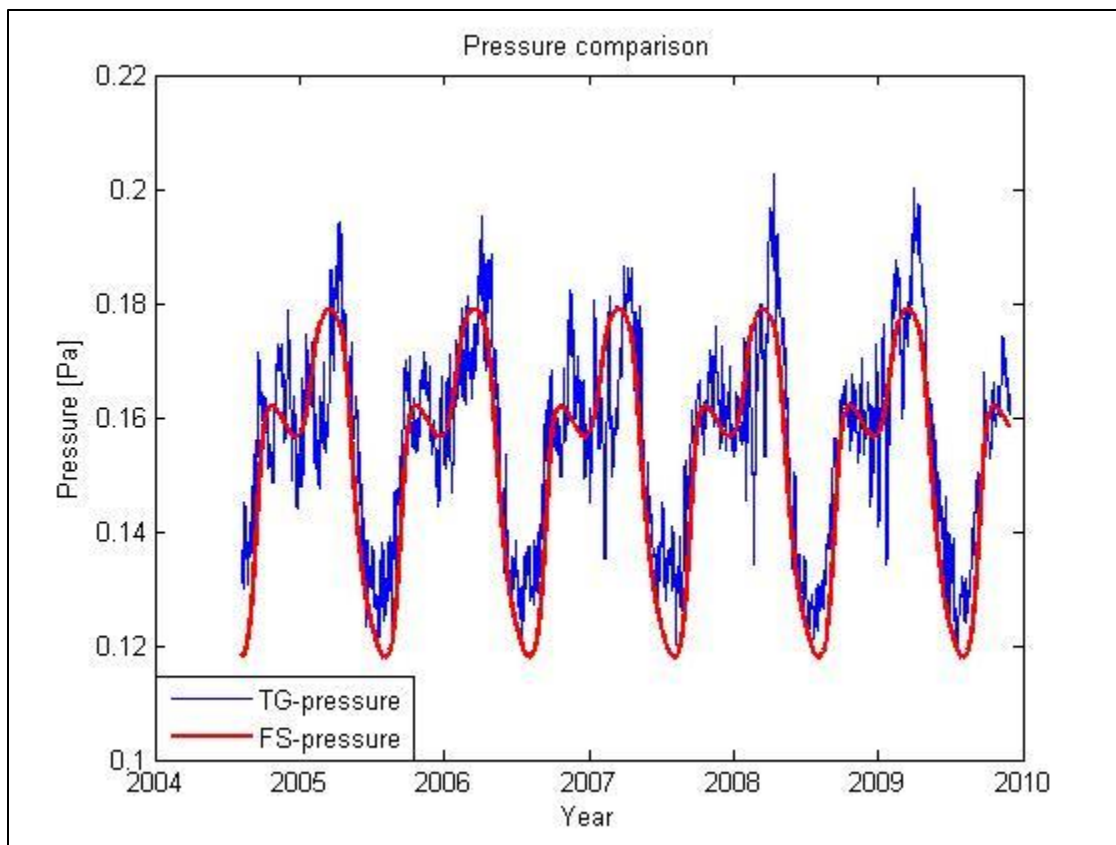Figure 32: The pressure estimated from the TG temperatures

Figure 33: Comparison of the TG-pressure and the FS-pressure.

The pressure estimates match very well, but there are some notable differences in the summer. The good match must partially be attributed to the fact that the falling sphere mass density measurements were used to produce the pressure. It is therefore curious that the largest deviations occurred in the summer where the falling sphere measurements are thought to be best. The temperatures calculated with this pressure are shown in Figure 34 together with the Aura MLS temperatures. A least squares regression analysis on these data gives a coefficient of determination of 0.922 and a standard deviation of ± 5.9 K. This result is close to the uncalibrated PB-temperatures. The R^2 value is a little bit smaller, but at the same time the standard deviation is slightly lower. By taking the Aura MLS uncertainty into account, the estimate of the intrinsic standard deviation of the temperatures produced with this method becomes ± 4.9 K.
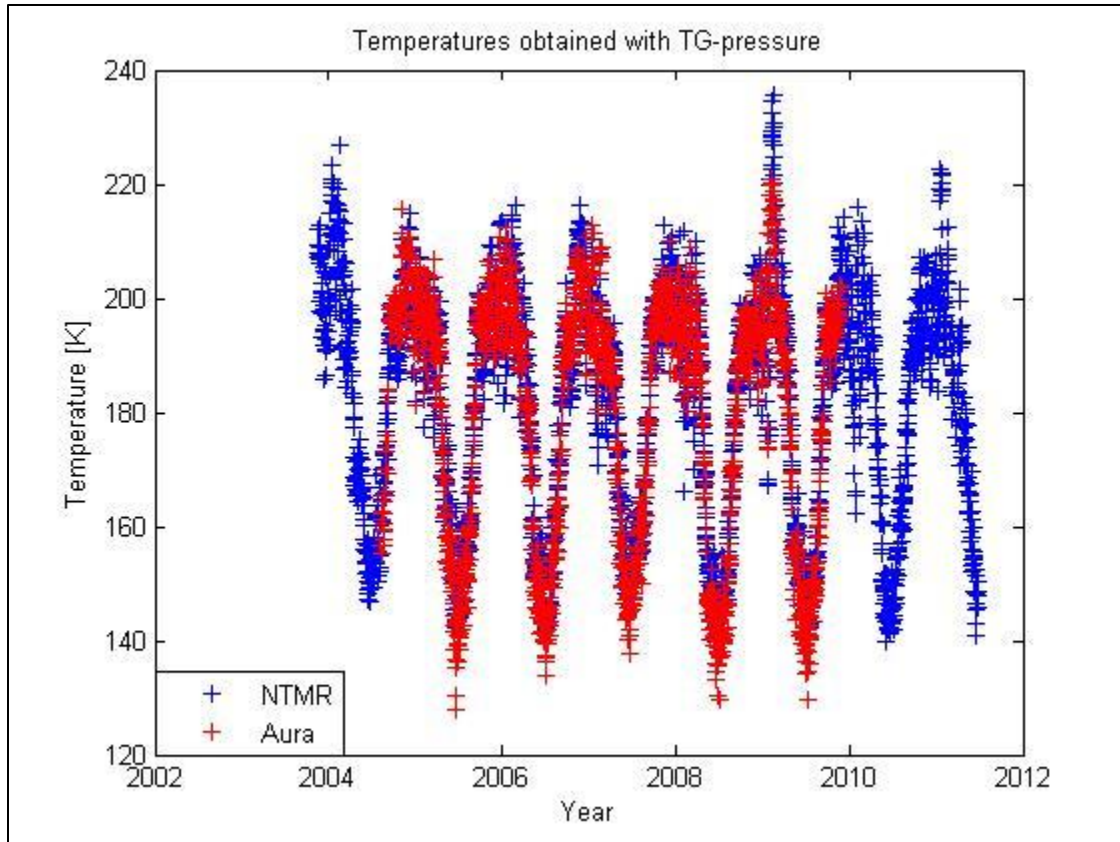
Figure 34: Temperatures obtained with the pressure estimated from the temperature gradient method.

It is also recognized that the close match against The Aura MLS measurements partially stems from the fact that the TG temperatures have been calibrated against the Aura MLS temperatures. At the same time, it should be noted that authors like Hocking et al. (2004) and Singer et al. (2004b) were able to obtain TG temperatures with similar accuracies without calibration. This suggests that this method has the potential of producing both pressure and temperature estimates with high accuracy even without calibration.

Chapter 9: Lidar comparison

Collocated with the meteor radar at Ramfjordmoen is a sodium lidar operated by Professor Satonori Nozawa at the Nagoya University in Japan (Tsuda, et al., 2010). A comparison between the lidar and the radar was proposed, although there is not a large amount of data to compare yet. This is mainly because the lidar is a fairly new installation that started doing measurements in October 2010 and temperature measurements have not been the main focus so far. Also, the lidar is not able to operate under daylight or cloudy conditions, which greatly restricts the runtime. As a consequence of this, the temperature measurements of the lidar have not yet been thoroughly validated, at least not compared to the Aura measurements.

Nozawa were able to obtain lidar temperatures from six periods where the lidar had run continuously for several hours. Unfortunately, the radar operated only during five of the six periods, leaving only five periods of measurements available for comparison. The lidar measurements are 30 minute average values. This should suit the radar well as 30 minutes are commonly regarded as the shortest time scale at which the radar can produce reliable temperatures. The Aura temperatures should have been included in the comparison, but the data at hand does not cover the period of time after the initialization of the lidar.

The radar automatically produces estimates of the ambipolar diffusion coefficients. These estimates are 30 minute averages. These coefficients are used to calculate the temperatures, and then the second degree polynomial calibration from Chapter 6 is applied. The period with the best match had a correlation coefficient of 0.65 and is presented in Figure 35. The period with the lowest correlation of 0.38 is plotted in Figure 36. The plots show that there can be rather large discrepancies between the two measurements but they also show similarities in the tides. In Figure 37, a scatterplot of all the coinciding data is presented. It is fair to say that the scatterplot displays a lot more scatter than what was hoped for. A least square analysis results in a correlation coefficient of 0.44 and a root mean squared error of 12.6 K.
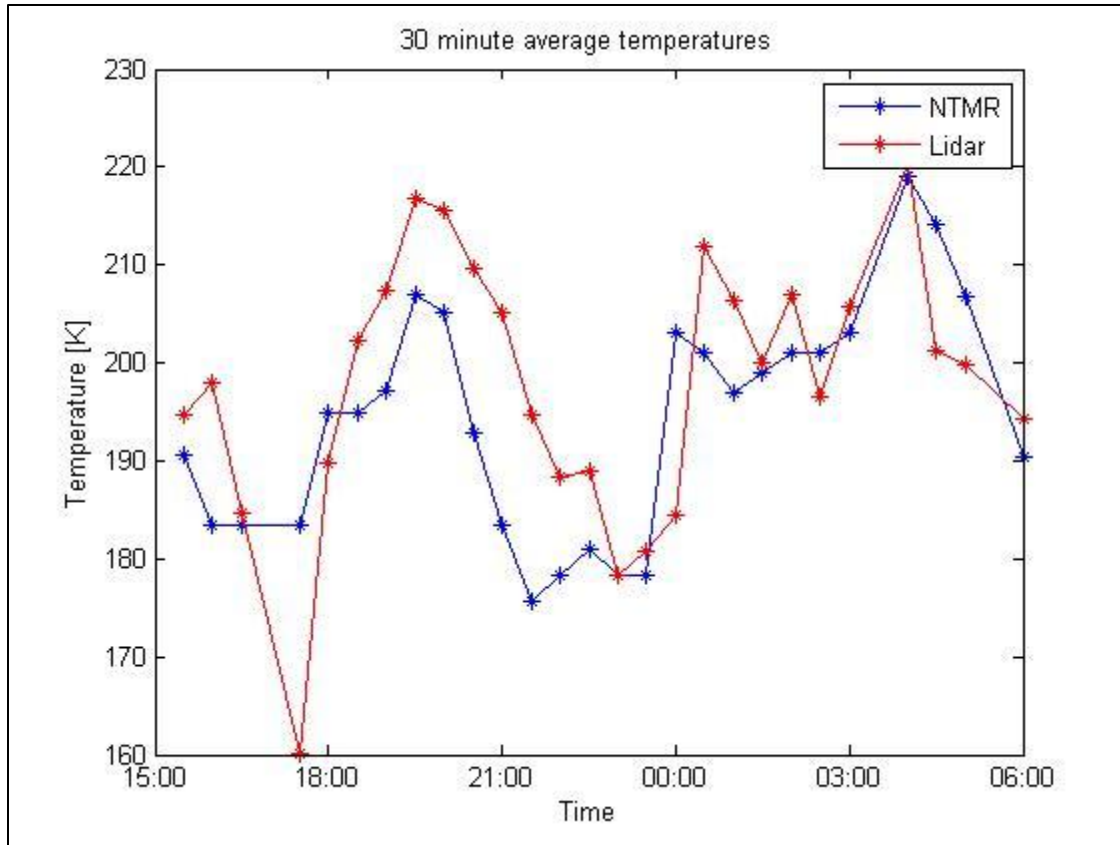
Figure 35: Comparison of lidar and radar temperatures for the period between 19.11.10 15:30 and 20.11.10 06:00. The Radar temperatures are shown in blue and the lidar temperatures in red. A line has been drawn between each measurement to emphasize the tides.
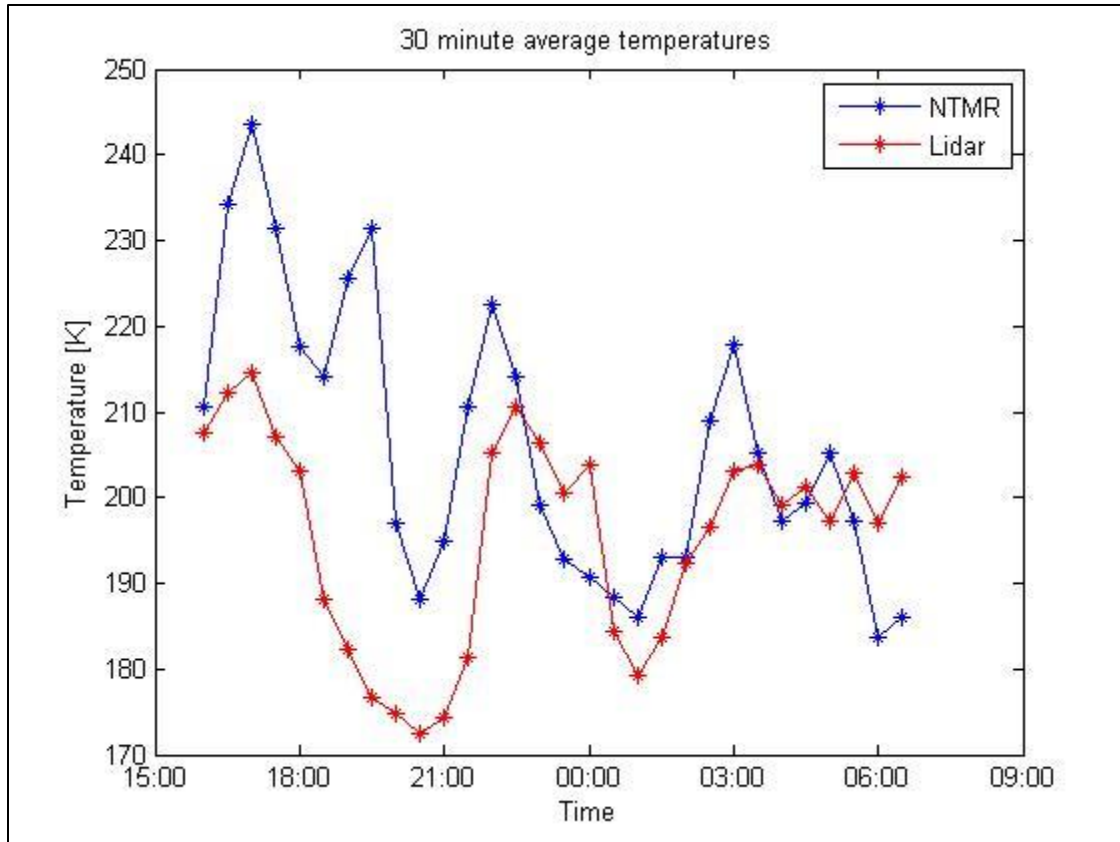
Figure 36: Comparison of lidar and radar temperatures for the period between 08.01.11 16:00 and 09.01.11 06:30. These temperatures had a correlation coefficient of 0.36, the lowest of the five comparisons.
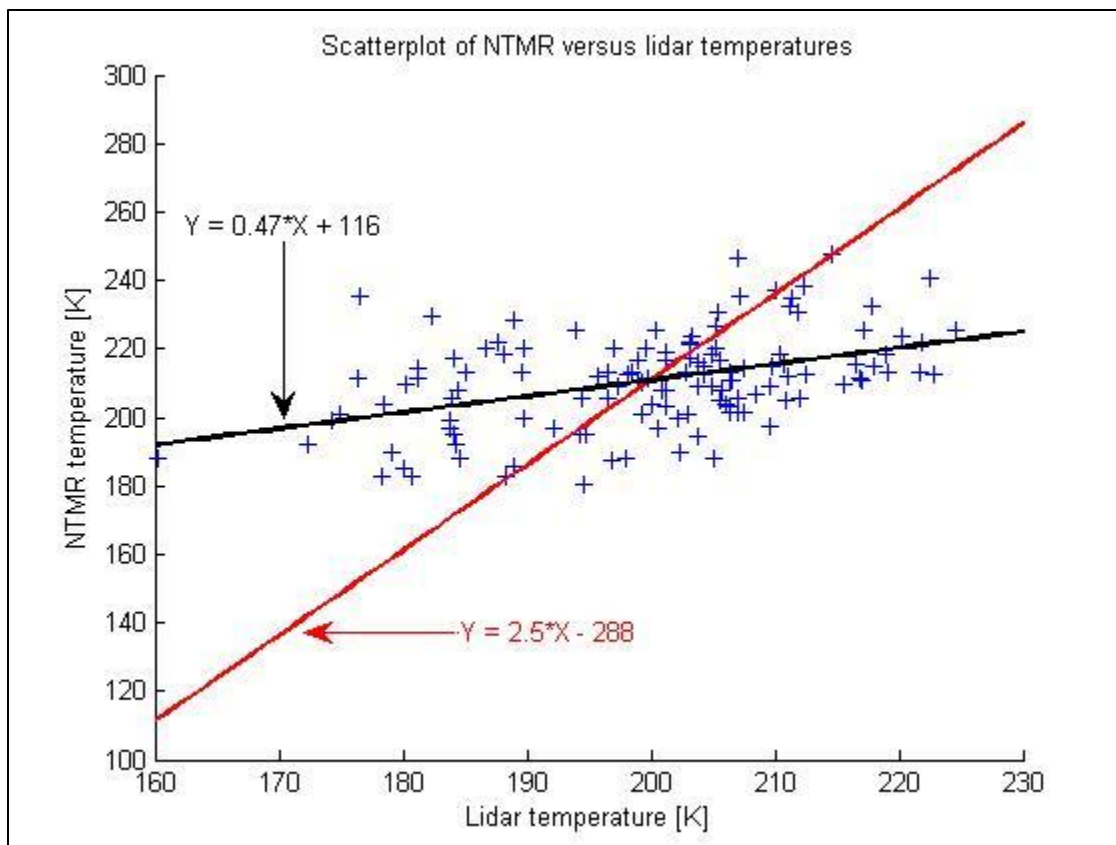
Figure 37: Scatterplot of radar versus lidar temperatures. The red line is the best fit line with zero uncertainty assumed in the radar measurements, and the black line is with zero uncertainty assumed in the lidar measurements.

The poor result from the lidar comparison raises doubts on the radar's ability to produce 30 minute average temperatures. It was found that the radar detected on average 16 meteors every 30 minutes in the height interval between 89.5 and 90.5 km. The lowest count was only four meteors and it is possible that this is too few to obtain a reliable temperature estimate. However, experiments with increased height interval to increase the number of meteors did not improve the results. Also, the radar temperatures are produced with the daily mean pressure values only. This may introduce relatively large errors, depending on the size of the intraday pressure variations.

In Figure 38 the mean temperatures for the five periods are presented. Although, there are too few data to perform any accurate analyses on these data, one may note that the deviations are almost 16 K for the three last periods.
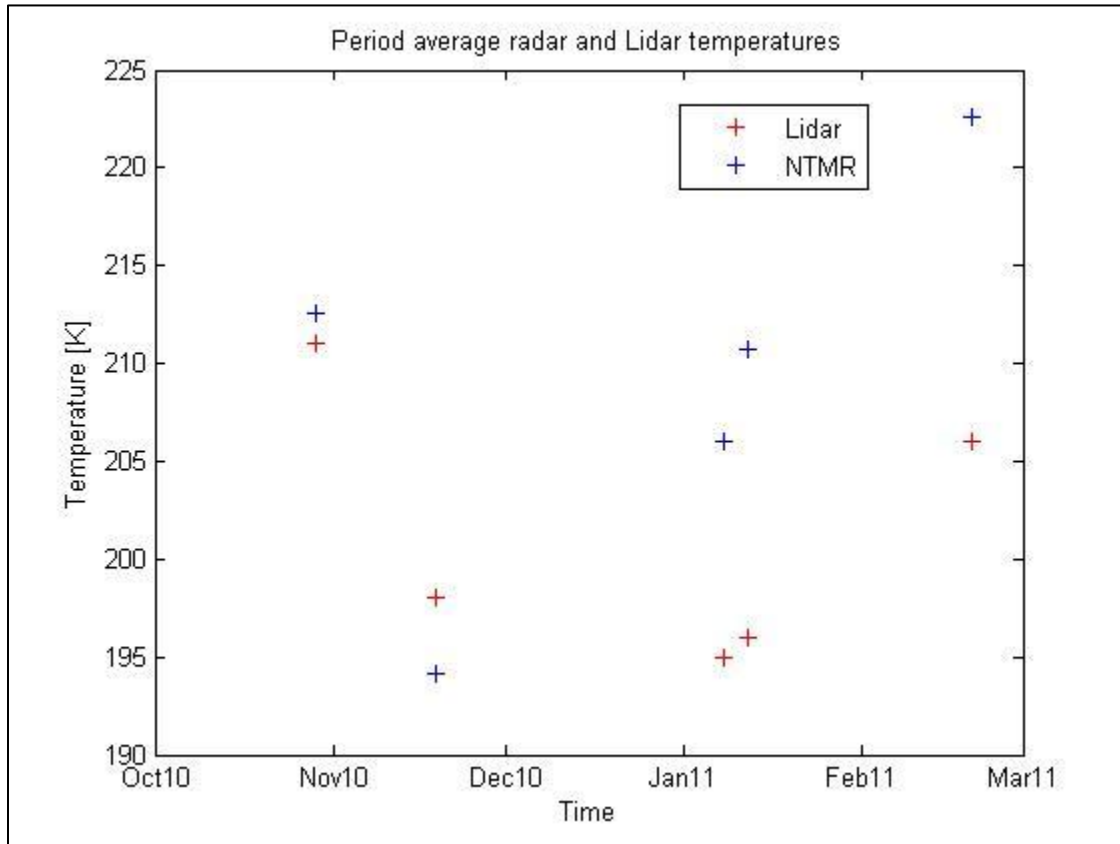

Figure 38: Period average lidar and radar temperatures.

In addition to the static pressure and the relatively low meteor count, the difference in measurement areas of the two instruments might contribute a lot to the discrepancies. At 90 km height, the radar measures over an area of 192,000 km^2, while the beam width of the lidar can be considered a point measurement. Both the lidar and the radar measurements show that the temperature can change with as much as 30° C within an hour. A large portion of the deviations between the instruments could be attributed to the differences in the measuring area if there are similar spatial variations in the temperatures.

With more data available in the future, it might be concluded that the radar is best suited to do measurements on longer time scales and the lidar is better for short time scale measurements. There is no doubt that the lidar measurements at the time of writing are too few to undergo a proper comparison. Regardless, we recognise that the collocation of these instruments can be of great benefit in the future. They have the potential of compensating for each other's weaknesses, and together they can form a valuable platform for observing the mesopause region.

Chapter 11: Application to climate studies

In this chapter the utility value of the meteor radar temperatures is discussed. A method for investigating the possibility of a long term trend is presented and the length of the time series needed to determine the trend with a 95 % confidence level is estimated.

A group of researchers observing PMSEs with the collocated European Incoherent Scatter radar are interested in the possibility of predicting temperatures in the mesopause region. The reason is that PMSEs occur at temperatures below 140 K when turbulent structures and sufficient ionisation are present. Therefore, a forecast could help the researchers to optimize the radar-time at their disposal. The ability of producing uninterrupted near real time temperature measurements could make the meteor radar a valuable instrument in the process of estimating future temperatures.

As mentioned earlier, the availability of data from the mesopause is very poor, thus new data is very likely to contribute to the basic knowledge of the region. As seen in the comparison against the lidar, the radar may not be the best choice for measurements on small spatial scales or short time scales. Its advantage is rather the capability of producing long continuous time series with little supervision and low cost. The need for long term measurements is most evident in climate change studies, where many years of measurements are needed to extract small trends from inherently noisy datasets. Now, it will be outline a procedure to detect long term change, and an estimate of the time needed to determine the trend with a confidence level of 95 % is calculated.

It is common to work with monthly average values when examining long term change. Therefore, monthly averages are calculated of the polynomially calibrated temperatures from section 6.5. Then, all measurements in the dataset belonging to January, February, March and so on are averaged. The latter will be called climatological monthly averages to avoid confusion. By subtracting the climatological values from the monthly values one gets a measurement of how much each month deviates from the overall mean, as well as an effective way to remove

the strong seasonal variation in the temperatures. In Figure 39 the monthly excursions from the climatological means are presented along with the best fit line obtained with the least squares method. The best fit line has a slope of − 5 K per decade, with an uncertainty of ± 1.5 K per decade. It is common to use the following expression to decide if a trend is determined at a 95 % confidence level (Tiao, et al., 1990)

$$\frac{|\omega|}{\sigma_\omega} > 2 \tag{57}$$

ω is the estimated trend and σ_ω is the standard deviation of the trend. In this case, the trend is large enough to be significant non-zero.
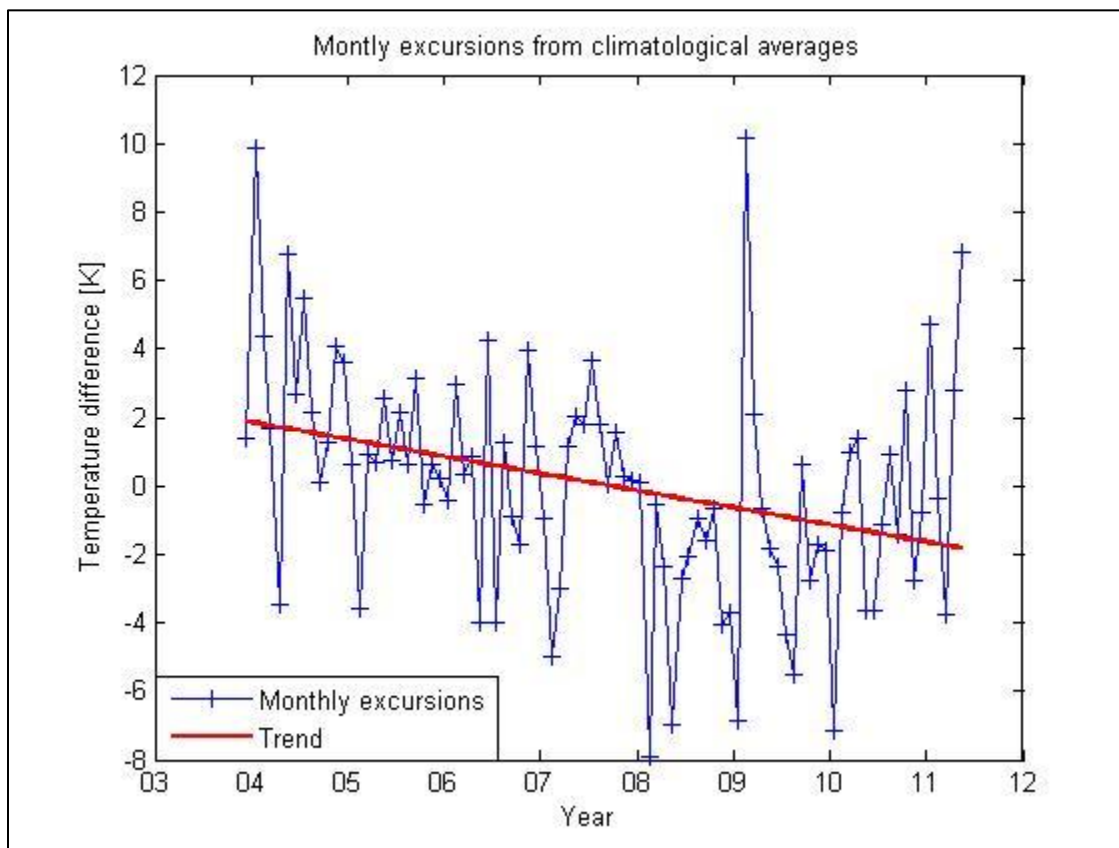

Figure 39: Monthly deviations from the overall mean. The red line is the best fit trend with a slope of − 5 K per decade.

Even if the trend line turned out to be significantly non-zero, one could not interpret it as proof of climate change. The trend is an estimate of the average change per month only for the period for which we have data. Short scale variations as daily and seasonal variations have been taken into account, but any variations with timescales longer than the length of the dataset are not. One well-known process which greatly affects the temperatures is the solar cycle. The solar cycle is a periodic variation in the suns magnetic activity, irradiation, number of sunspots and other properties that have a period of about 11 years (Rishbeth and Clilverd, 1999).

A change in the irradiance from the sun will affect the temperatures on earth, especially in the upper atmosphere. In order to examine the effect of the solar cycle, a smoothed version of the monthly excursions is plotted in the upper panel of Figure 40 and the international sunspot number is plotted in the bottom panel. In this way the link between the temperature and the solar cycle becomes clear.
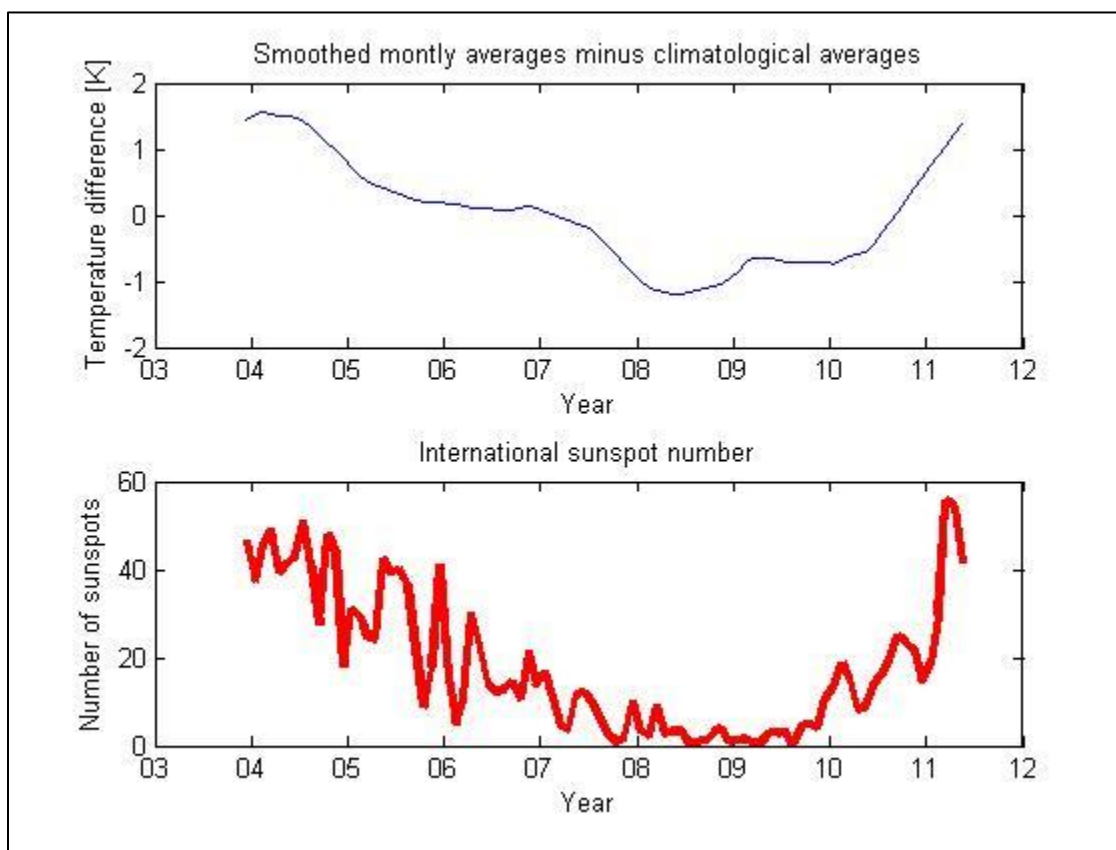

Figure 40: Comparison of monthly temperature excursions and sunspot numbers.

The ideal way to remove this variation is to average over several solar cycles. This is one of the reasons why detecting climate change requires long time series. The radar has at the time of writing collected less than eight years of data, thus such an averaging is not possible. Another way to handle the solar cycle is to use the sunspot number. First, a linear regression is performed on the monthly excursions versus the sunspot number. The regression coefficients are then used to create a new time series, which is subtracted from the monthly excursions.

The solar cycle adjusted monthly excursions are presented in in Figure 41 along with the trend line. The new trend line has a slope of – 2.2 K per decade, with a standard deviation of ± 1.5 K per decade. It is noteworthy that this result is less than half of the trend before the solar cycle was removed, thus emphasizing the importance of taking the solar cycle into consideration.
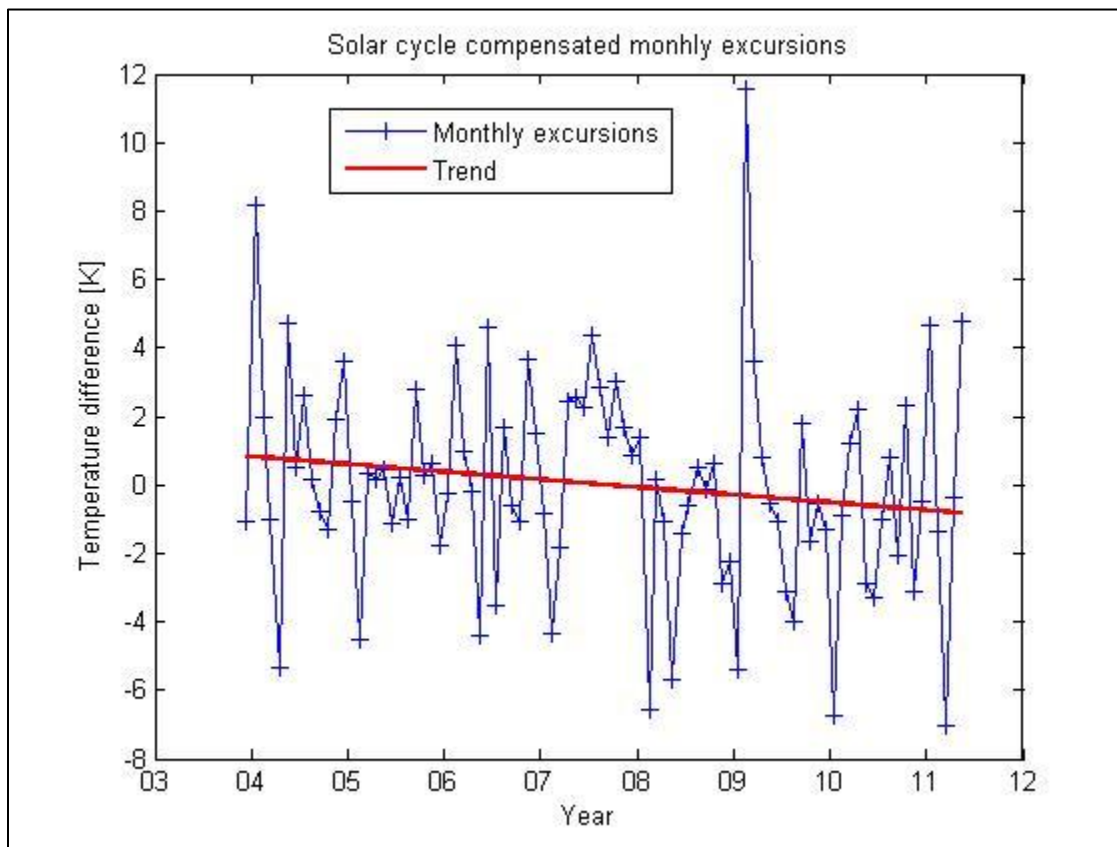

Figure 41: Solar cycle adjusted monthly excursions and best fit trend line with a slope of -2.2 K per decade.

From the decision rule in Equation (57) it can be seen that the solar cycle adjusted trend is far from significantly non-zero. The negative trend is however in in accordance with models predicting lower temperatures in the upper atmosphere as the carbon dioxide level rise (Roble and Dickinson, 1989). It is obvious that more data is needed in order to increase the certainty of the estimated trend. Weatherhead, Stevermer and Schwartz (2002) used the following approximate expression for the number of years n needed to determine a trend at the 95 % confidence level with a probability of 90 % as

$$n \approx \left(\frac{3.3\sigma_n}{|\omega|} \cdot \sqrt{\frac{1+\varphi}{1-\varphi}} \right)^{\frac{2}{3}}, \tag{58}$$

where σ_n is the standard deviation of the noise, and φ is the autocorrelation at lag one. Before calculating the standard deviation of the noise, any trend in the monthly excursions is removed, so that only the noise part remains. From the formula we see that n increases with the noise and autocorrelation, and that larger trends are easier to detect than smaller trends. For this dataset, the standard deviation of the noise is ± 3 K and the autocorrelation at lag one is 0.006. Inserting these values into Equation (58) yields n = 13 years, for the trend of - 2.2 K per decade.

The main reason for the need of such a long time series is that the trend we seek to determine is very small compared to the noise in the dataset. So far, only the average trend has been considered, but it is not necessarily such that the trend is equal for all months of the year. In Figure 42 the trend for each individual month is presented. The trend seems to vary throughout the year. In fact the resulting trends in April and October are strongly positive and the trends in January, June and November are strongly negative.
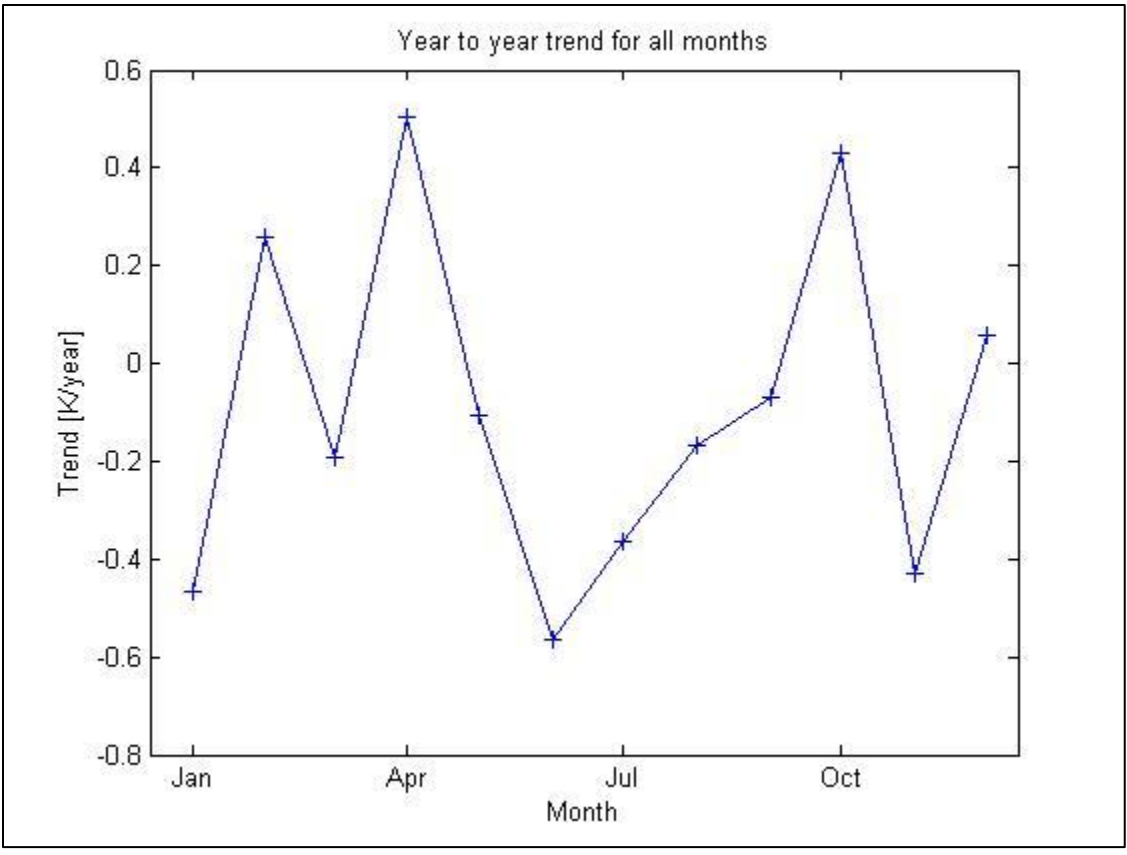
Figure 42: The trend per year for all months.

In the above analysis the process has been assumed to be autoregressive and the probability distributions have been assumed to be Gaussian. This may not be the case and a more thorough analysis of the noise would enable us to take the true probability distribution into account as done in Hall, Rypdal and Rypdal (2011).

Chapter 10: Conclusion

Daily temperatures at 90 km have been obtained with the Nippon/Norwegian meteor radar using two different methods. The pressure method gave the best result with a standard deviation of ± 5.8 K from the Aura MLS temperatures. By calibrating the temperatures with a second degree polynomial, the standard deviation was lowered to ± 5.1 K. These results are among the best results that have been achieved with meteor radars. However, it is likely that a better pressure model would improve the results even further. Compared with previous work, there have been made mainly three important improvements. The first was the use of a more suitable reduced ion mobility constant. The second was the replacement of the linear calibration used previously with a polynomial calibration. The last major improvement was the introduction of upper and lower decay time limits.

A relatively new statistical comparison technique was employed to estimate the intrinsic uncertainty of the radar measurements. For the uncalibrated temperatures the intrinsic error was estimated to ± 4.6 K and the calibrated temperatures gave a standard deviation of ± 3.8 K. The other temperature acquisition technique, the temperature gradient method, gave a very poor temperature estimate with standard deviation of ± 11.7 K from the Aura MLS temperatures. Despite the low accuracy of the raw temperatures, the standard deviation ended up at an acceptable uncertainty of ± 7.4 K after calibration. It is recognized that other authors have produced more precise measurements with this method, and more work should allow for accurate temperature measurements with this method without calibration. For instance, it is possible that the use of the bias correction from Hocking et al. (1997) over the statistical comparison method would improve the results. Also, this method will most certainly gain from an improved vertical temperature gradient model. The accuracy of both techniques are therefore expected to improve with increaced knowledge of the mesopause region.

In addition to the ability of creating very accurate temperatures both with and without calibration, the pressure method is far simpler to implement. The pressure method is therefore recommended, subject to an appropriate pressure model.

The gradient method should however not be rejected as there are situations where the method will be beneficial. This was shown in Chapter 8 when the two methods were combined into one method capable of estimating both temperatures and pressure at 90 km altitude. The latter is a rather unique capability. However, this approach was still dependent on external data, namely the atmospheric number density. A more ideal way to combine the methods into one method virtually independent of external data is also suggested. The approach relies on the ability of the pressure method to create height dependent temperatures. Unfortunately, attempts at this failed for hitherto unknown reasons. Solving this problem may enable a combination of the two existing methods into one method capable of measuring both temperatures and pressure without the need for input data.

Throughout the thesis, the Aura MLS instrument has been used for validation of the radar temperatures. A new and exciting comparison alternative was introduced in the relatively new and collocated sodium lidar. The two instruments had a low average correlation coefficient of 0.44, but there was not enough data available to perform any proper analyses. The radar measures over a much larger spatial scale than the lidar and this is probably one of the main reasons for the low correlation. Although the difference in the measured areas may prevent direct comparison of the temperatures, it may very well become an advantage as the two instruments can fulfil each other's weaknesses.

Finally, some possible utilisations of the radar temperatures are discussed. A method for investigation of climate change is outlined. The data collected so far gave a trend of - 2.2 K per decade with an uncertainty of ± 1.5 K per decade. The large uncertainty of the trend means that more data is required in order to determine a non-zero trend at the 95 % confidence level. The length of the time series needed to obtain the trend with a probability of 90 % was estimated to 13 years. It is interesting to note that the negative sign of the preliminary trend is consistent with the expected decrease in temperatures with increased amounts of carbon dioxide in the upper atmosphere.

Chapter 12: Bibliography

Beig, G., Keckhut, P., Lowe, R. P., Roble, R. G., Mlynczak, M. G., Scheer, J., Fomichev, V. I., Offerman, D., French, W. J., Shepherd, M. G., Semenov, A. I., Remsberg, E. E., She, C. Y., Lübken, F.-J., Bremer, J., Clemesha, B. R., Stegman, J., Sigernes, F. and Fadnavis, S. (2003). Review of mesospheric temperature trends. *Rev. Geophys., 41*. doi:doi:10.1029/2002RG000121

Bronshten, V. A. (1983). *The Physics of Meteoric Phenomen.* Norwell: D. Reidel Pub Co.

Ceplecha, Z., Borovicka, J., Elford, W. G., Revelle, D. O., Hawkes, R. L., Porubcan, V. and Simek, M. (1998). Scattering of radio wave from meteor trails, Meteor phenomena and bodies. *Space Sci. Rev., 8J*, 327-471.

Cervera, M. A. and Reid, I. M. (2000). Comparison of atmospheric parameters derived from meteor observations with CIRA. *Radio Sci., 35*(3), 833-843.

Chilson, P. B., Czechowsky, P. and Schmidt, G. (1996). A comparison of ambipolar diffusion coefficients in meteor trains using VHF radar and. *Geophys. Res. Lett., 23*, 2745–2748.

Cosby, P. C. and Slanger, T. G. (2007). OH spectroscopy and chemistry investigated with astronomical sky spectra. *Can. J. Phys, 85*, 77–99. doi:10.1139/P06-088.

Dyrland, M. E., Hall, C. M., Mulligan, F. J., Tsutsumi, M. and Sigernes, F. (2010). Improved estimates for neutral air temperatures at 90 km and 78°N using satellite and meteor radar data. *Radio Sci., 45, RS4006*. doi:10.1029/2009RS004344.

Dyrud, L. P., Oppenheim, M. M. and vom Endt, A. F. (2001). The anomalous diffusion of meteor trails. *Geophys. Res. Lett., 28*, 2775– 2778.

French, W. R. and Mulligan, F. J. (2010). Stability of temperatures from TIMED/SABER v1.07 (2002–2009) and Aura/MLS v2.2 (2004–2009) compared with OH(6-2) temperatures

observed at Davis Station, Antarctica. *Atmos. Chem. Phys. Discuss., 10*, 21547-21565. doi:10.5194/acpd-10-21547-2010

Garcia, R. R. and Solomon, S. (1985). The effect of breaking gravity waves on the dynamics and chemical composition of the mesosphere and lower thermosphere. *J. Geophys. Res., 90*, 3850–3868.

Hall, C. M. (2002). On the influence of neutral turbulence ambipolar diffusivities deduced from meteor trail expansion. *Annal. Geophys., 20*, 1857–1862.

Hall, C. M., Aso, T., Tsutsumi, M., Höffner, J., Sigernes, F. and Holdsworth, D. A. (2006). Neutral air temperatures at 90 km and 70N and 78N. *J. Geophys. Res., 111, D14105*. doi:10.1029/2005JD006794.

Hall, C. M., Rypdal, K. and Rypdal, M. (2011). The E region at 69°N, 19°E: Trends, significances, and detectability. *J. Geophys. Res., 116, A05309*. doi:10.1029/2011JA016431

Havnes, O. and Sigernes, F. (2005). On the influence of background dust on radar scattering from meteor trails. *J. Atmos. Sol.-Terr. Phys., 67*(6), 659–664. doi:10.1016/j.jastp.2004.12.009

Hedin, A. E. (1991). Extension of the MSIS thermosphere model into the middle and lower atmosphere. *J. Geophys. Res., 96, NO, A2*, 1159 – 1172. doi:10.1029/90JA02125

Hocking, W. K. (1999). Temperatures using radar-meteor decay times. *Geophys. Res. Lett., 26*, 3297–3300.

Hocking, W. K. (2004). Radar meteor decay rate variability and atmospheric consequences. *Ann. Geophys., 22*(11), 3805-3814. doi:10.5194/angeo-22-3805-2004

Hocking, W. K., Singer, W., Bremer, J., Mitchel, N. J., Batista, P., Clemesha, B. and Donner, M. (2004). Meteor radar temperatures at multiple sites derived with SKiYMET radars and compared to OH, rocket and lidar measurements. *J. Atmos. Sol. Terr. Phys., 66*(6-9), 585-593. ISSN 1364-6826. doi:10.1016/j.jastp.2004.01.011

Hocking, W. K., Thayaparan, T. and Franke, S. (2001b). Method for statistical comparison of geophysical data by multiple instruments which have differing accuracies. *Adv. Space Res., 27*(6–7), 1089–1098.

Hocking, W. K., Thayaparan, T. and Jones, J. (1997). Meteor decay times and their use in determining a diagnostic mesospheric temperature pressure parameter: Methodology and one year of data. *Geophys. Res. Lett., 24*, 2977– 2980.

Höffner, J. and Lübken, F. J. (2007). Potassium lidar temperatures and densities in the mesopause region at Spitsbergen (78N). *J. Geophys. Res., 112, D20114*. doi:10.1029/2007JD008612.

Holdsworth, D. A. and Reid, I. M. (2002). The Buckland Park meteor radar - description and initial results. *Workshop on the Applications of Radio Science (WARS02) (2002 : Leura, NSW). 095804760x.* Physics Publications.

Holdsworth, D. A., Morris, R. J., Murphy, D. J., Reid, I. M., Burns, G. B. and French, W. J. (2006). Antarctic mesospheric temperature estimation using the Davis mesosphere-stratosphere-troposphere radar. *J. Geophys. Res., 111, D05108*. doi:10.1029/2005JD006589

Jones, W. (1995). Theory of the initial radius of meteor trains. *Mon. Not. R. Astron. Soc., 275*, 812–818.

Jones, W. and Jones, J. (1990). Ionic diffusion in meteor trains. *J. Atmos. Terr. Phys., 52*(3), 185-191. doi:10.1016/0021-9169(90)90122-4

Kumar, K. K. (2007). Temperature profiles in the MLT region using radar-meteor trail decay times: Comparison with TIMED/SABER observations. *Geophys. Res. Lett., 34, L16811*. doi:10.1029/2007GL030704

Laštovička, J., Akmaev, R. A., Beig, G., Bremer, J., Emmert, J. T., Jacobi, C., Jarvis, M. J., Nedoluha, G., Portnyagin, Y. I. and Ulich, T. (2008). Emerging pattern of global change in

the upper atmosphere and ionosphere. *Ann. Geophys., 26*, 1255 - 1268. doi:10.5194/angeo-26-1255-2008

Livesey, N. J., Read, W. G., Lambert, A., Cofield, R. E., Cuddy, D. T., Froidvaux, L., Fuller, R. A., Jarnot, R. F., Jiang, J. H., Jiang, Y. B., Knosp, B. W., Kovalenko, L. J., Pickett, H. M., Pumphrey, H. C., Santee, M. L., Schwartz, M. J., Stek, P. C., Wagner, P. A., Waters, J. W. and Dong, L. W. (2007). Version 2.2 Level 2 data quality and description document. *Tech. rep., JPL, California Institute of Technology. http://mls.jpl.nasa.gov/data/v2-2_data_quality_document.pdf*.

Lübken, F. -J. (1999). Thermal structure of the Arctic summer mesosphere. *J. Geophys. Res., 104*, 9135– 9149.

Lübken, F. -J. and von Zahn, U. (1991). Thermal structure of the mesopause region at polar latitudes. *J. Geophys. Res., 96*, 20,841– 20,857.

Lübken, F. -J., Hillert, W., Lehmacher, G., von Zahn, U., Bittner, M., Offerman, D., Schmidlin, F. J., Hauchecorne, A., Mourier, M. and Czechowsky, P. (1994). Intercomparison of density and temperature profiles obtained by lidar, ionization gauges, falling spheres, datasondes and radiosondes during the DYANA campaign. *J. Atmos. Solar-Terr. Physics, 56*(13-14), 1969-1984. doi:10.1016/0021-9169(94)90023-X.

Mason, E. A. and McDaniel, E. W. (1988). *Transport Properties of Ions in Gases.* New York: John Wiley.

McKinley, D. W. (1961). *Meteor Science and Engineering.* New York: McGraw-Hill.

Rishbeth, H. and Clilverd, M. (1999). Long-term change in the upper atmosphere. *Astronomy & Geophysics, 40*, 3.26 - 3.28.

Roble, R. G. and Dickinson, R. E. (1989). How will changes in carbon dioxide and methane modify the mean structure of the mesosphere and thermosphere? *Geophys. Res. Lett., 16*(12), 1441-1444.

Sigernes, F., Shumilov, N., Deehr, C. S., Nielsen, K. P., Svenøe, T. and Havnes, O. (2003). Hydroxyl rotational temperature record from the auroral station in Adventdalen, Svalbard. *J. Geophys. Res., 108*(A9), 1342. doi:10.1029/2001JA009023

Singer, W., Bremer, J., Weib, J., Hocking, W. K., Hoffner, J., Donner, M. and Espy, P. (2004b). Meteor radar observations at middle and Arctic latitudes. Part 1: mean temperatures. *J. Atmos. Sol.-Terr. Phys., 66*(6-9), 607–616.

Singer, W., Latteck, R., Millan, L. F., Mitchell, N. J. and Fielder, J. (2008). Radar backscatter from underdense meteors and diffusion rates. *Earth Moon and Planets, 102*(14), 403 - 409.

Takahashi, H., Nakamura, T., Tsuda, T., Buriti, R. A. and Gobbi, D. (2002). First measurement of atmospheric density and pressure by meteor diffusion coefficient and airglow OH temperature in the mesopause region. *Geophys. Res. Lett., 29*(8), 1165. doi:10.1029/2001GL014101

Tiao, G. C., Reinsel, G. C., D. Xu, D., Pedrick, J. H., Zhu, X., Miller, A. J., DeLuisi, J. J., Mateer, C. L. and Wuebbles, D. J. (1990). Effects of autocorrelation and temporal sampling schemes on estimates of trend and spatial correlation. *J. Geophys. Res., 95, D12*, 20,507 – 20,517. doi:10.1029/JD095iD12p20507

Tsuda, T. T., Nozawa, S., Kawahara, T., Kawabata, T., Oyama, S., Fujii, R., Ogawa, Y., Saito, N., Wada, S., Brekke, A. and Hall, C. M. (2010). A sodium lidar project at Tromsø, Norway: First report on test observations at Wako, Japan and current status. *Proceeding of the CAWSES-II Kick-Off Symposium.* Kyoto University: American Geophysical Union.

Weatherhead, E. C., Stevermer, A. J. and Schwartz, E. B. (2002). Detecting environmental changes and trends. *Physics and Chemistry of the Earth, 27*, 399-403.

Winick, J. R., Wintersteiner, P. P., Picard, R. H., Esplin, D., Mlynczak, M. G., Russel III, J. M. and Gordley, L. L. (2009). OH layer characteristics during unusual boreal winters of 2004 and 2006. *J. Geophys. Res., 114, A02303*. doi:10.1029/2008JA013688.